

May 2012

Automation of the Registration of Range Plant Images Using Geomagic Studio

Quazi M. Akter

The University of Western Ontario

Supervisor

Dr. John L. Barron

The University of Western Ontario

Graduate Program in Computer Science

A thesis submitted in partial fulfillment of the requirements for the degree in Master of Science

© Quazi M. Akter 2012

Follow this and additional works at: <https://ir.lib.uwo.ca/etd>



Part of the [Other Computer Sciences Commons](#)

Recommended Citation

Akter, Quazi M., "Automation of the Registration of Range Plant Images Using Geomagic Studio" (2012). *Electronic Thesis and Dissertation Repository*. 513.

<https://ir.lib.uwo.ca/etd/513>

Automation of the Registration of Range Plant Images Using Geomagic Studio

(Thesis format: Monograph)

by

Quazi Mah-Zereen Akter

Graduate Program in Computer Science

Submitted in partial fulfillment
of the requirements for the degree of
Master of Science

School of Graduate and Postdoctoral Studies
The University of Western Ontario
London, Ontario
April, 2012

© Quazi Mah-Zereen Akter 2012

THE UNIVERSITY OF WESTERN ONTARIO
SCHOOL OF GRADUATE AND POSTDOCTORAL STUDIES

CERTIFICATE OF EXAMINATION

Supervisor

Dr. John L. Barron

Examiners

Dr. Mahmoud R. El-Sakka

Dr. Robert Webber

Dr. Lindi M. Wahl

The thesis by
Quazi Mah-Zereen Akter

entitled

AUTOMATION OF THE REGISTRATION OF RANGE PLANT IMAGES USING
GEOMAGIC STUDIO

is accepted in partial fulfillment of the
requirements for the degree of
Master of Science

Date

Dr. Marc Moreno Maza
Chair of Examining Board

Abstract

As plant science advances, the quantitative measurement of 3D plant growth has become an essential tool to evaluate the growth performance of genetically modified seeds or plants. In the past, “wet volumes” had been used to quantitatively measure plant growth which result in the destruction of the plants. Other traditional methods like interferometry methods or mechanical methods are also inefficient because they are either invasive or unable to provide sufficient growth information. On the other hand, computer vision methods, especially optical and range flow techniques, are non-contact, more accurate, and relatively less expensive. But they require a fixed light source for the experimental environment and also, higher acquisition rate for the data.

In this thesis, we generate a number of 3D range scans of the *Arabidopsis thaliana* plant from different viewpoints. We use ShapeGrabber laser scanner to acquire the scanned data and Geomagic Studio 12 CAD software to register these scans to produce 3D polygonal meshes. Then, the canopy surface area and 3D stem volume of the plant are computed from these meshes to determine its growth over a time cycle. To perform registration in Geomagic, 6 ping pong balls are used as reference spheres. However, because the laser scanner can only see the 3D environment that is visible from its line-of-sight, the balls are imaged as semi-spheres in the original range images. But, Geomagic is unable to register multiple images with incomplete semi-sphere data and requires full spheres as target objects. Zhao (MSc UWO 2010) and Yang (MSc UWO 2009) manually replaced these semi-spheres with artificially generated spheres using Geomagic which is both tedious and error prone. Moreover, they manually rotated the images to find out the pair of spheres that matches in adjacent range scans and aligned them manually before performing the registration. Because of the manual nature of this processing, full or semi automation of the registration process is very desirable. Among the major contributions of this research are not only to automatically generate synthetic sphere data but also detect and localize the semi-spheres in the original range images using parameter estimation techniques and parametric equation of spheres. Additionally, we reconstruct the original range images by replacing the incomplete semi-sphere data with “perfect” full sphere data to aid Geomagic during the automatic detection of target objects. After this pre-processing, the modified images are automatically registered using Geomagic macros so that the

3D polygonal meshes found from the registration process can be used to measure plant growth quantitatively. We believe that the automation of the registration process is a good first step towards a fully automated system of 3D plant growth measurement.

Acknowledgments

Acknowledgments

First of all, I thank Allah the most beneficent and merciful as He allowed me to finish my thesis successfully.

I would like to express special gratitude to my supervisor, Prof. John L. Barron, for his constant support, patient guidance, insightful suggestion and sincere encouragement as these were essential to the completion of my Masters degree.

I also thank Prof. Mahmoud El-Sakka– I learned a lot from his course on advanced image compression techniques. My sincere gratitudes also go to Prof. Robert Mercer for allowing me to get engaged with a different genre of research and for his moral support during my Masters degree.

My gratitude also goes to Geomagic Technical Support team, especially Richard Sandham, for their constant help. Without their technical support and expert opinions, I would have been lost at some points.

Also, I extend thanks to the Department of Computer Science administrative staff for their assistance in the course of my study at Western.

I am grateful to my parents, specially my mother who is my inspiration at all times– I came this long and will continue my journey for them. I would also like to thank my sister and brother for their love and support.

I thank my loving husband Rushdi Shams for reminding me how to smile even in the darkest hours of life and I show my gratitude to my friends who were so considerate when I shared my joy as well as frustrations with them.

I wish to dedicate my thesis to my wonderful “curious George” nephew Aayan.

Table of Contents

Certificate of Examination	ii
Abstract	iv
Acknowledgment	iv
Acknowledgments	iv
List of Tables	vii
List of Figures	x
1 Introduction	1
1.1 Problem Statement	2
1.2 Motivation	4
1.3 Thesis Contributions	5
1.3.1 Generating Full Sphere from Semi-sphere Data	5
1.3.2 Automating the Registration Process using Geomagic Macros	5
1.3.3 Improving Speed and Accuracy	6
1.4 Thesis Outline	6
2 Literature Review	8
2.1 A General Overview of Parameter Estimation Techniques	8
2.2 Basic Categories of Parameter Estimation	9
2.2.1 Least-Squares Fitting	10
2.2.1.1 LS Fitting Based on Algebraic Techniques	10

2.2.1.2	The Insufficiency of Algebraic Techniques	11
2.2.1.3	LS Fitting Based on Euclidean Norm	11
2.2.2	Robust Estimation	14
2.2.2.1	M-estimators	14
2.2.2.2	Bounded-Influence Estimators and MM-estimators	16
2.2.2.3	L_1 Regression	17
2.2.2.4	Regression Diagnostics	17
2.2.2.5	Least Median of Squares (LMedS) Estimators	17
2.3	Recent Plant Growth Measurement Techniques using Computer Vision	18
2.4	Conclusion	21
3	Experimental Methodology	22
3.1	Implementation of Automatic Registration Process	27
3.1.1	The Process of Segmentation and Estimation	30
3.1.1.1	Segmentation of Semi-Spheres	30
3.1.1.2	Estimation of Parameters (Center Coordinates and Radius of Semi-Spheres)	31
3.1.1.3	Segmentation of Plant Data	33
3.1.2	Replacement of Semi-sphere with Full Sphere Data	33
3.1.3	Reconstruction of Views	35
3.1.4	Process of Registration	35
3.1.5	Measuring the Growth Cycle of <i>Arabidopsis thaliana</i> Plants	39
3.1.5.1	Manual Editing (Pre-processing)	39
3.1.5.2	Measuring Plant Growth using the 3D Triangular Meshes	40
3.2	Conclusions	47
4	Results and Discussion	64
4.1	Problems with the <i>Arabidopsis thaliana</i> Datasets	64
4.1.1	Missing Datasets	64
4.1.2	Validating the Experimental Outcomes	64
4.1.3	Problems with Manual Processing	66
4.2	Methods of Validation	67

4.2.1	Validation of Sphere Fitting Algorithms	67
4.2.2	Validation of the Registration Process	68
4.2.3	Validation of Plants Areas and Volumes	69
4.3	Experimental Results and Discussion	69
4.3.1	Performance Analysis of the Parameter Estimation Techniques	69
4.3.2	Performance Analysis of the Registration Process	72
4.3.3	Performance Analysis of the Plant Growth Measurement . . .	74
4.3.3.1	Changes in Plant Canopy Area	74
4.3.3.2	Changes in 3D Stem Volume	77
4.4	Conclusion	80
5	Conclusion and Future Work	85
5.1	Summary	85
5.2	Future Work	87
A	Average and Standard Deviation of Average Radius (Datasets: 30-40)	90
B	Average and Standard Deviation of Average Residual (Datasets: 30-40)	96
C	Average and Standard Deviation of Average Radius (Datasets: 60-70)	102
D	Average and Standard Deviation of Average Average Residual (Datasets: 60-70)	108
E	Whole Plants Surface Area Measurement From Yang and Our Experiment	114
F	3D Stem Volume Measurement From Yang Our Experiment	117
G	Macros used to Automate Various Geomagic's Tools	119
	Bibliography	125
	Vita	131

List of Tables

2.1	Objective function and weight functions of the LS, Huber and Bisquare estimators	15
2.2	Advantages and disadvantages of three approaches to measure quantitative plant growth	19
3.1	3PI file format	24
3.2	STL file format	25
3.3	List of the ranges indicating up to which datasets the position of the reference spheres was unchanged. Note that datasets 52 and 53 and parts of dataset 51 are missing.	27
3.4	List of the Geomagic's macros and their equivalent VBScript code used to automate the registration process	39
4.1	Estimated average radius and standard deviation values of the reference spheres for dataset 30-40	72
4.2	Estimated average radius and standard deviation values of the reference spheres for datasets 60-70	73
4.3	Estimated average residual and standard deviation values of the reference spheres in datasets 30-40	74
4.4	Estimated average residual and standard deviation values of the reference spheres in datasets 60-70	75
4.5	Performance Analysis of the overall registration (datasets 30-40) . . .	76
4.6	Performance Analysis of the overall registration process (datasets 60-70)	77
A.1	Average and standard deviation of average radius (mm) for dataset 30	90
A.2	Average and standard deviation of average radius (mm) for dataset 31	91
A.3	Average and standard deviation of average radius for dataset 32 . . .	91

A.4	Average and standard deviation of average radius (mm) for dataset 33	92
A.5	Average and standard deviation of average radius (mm) for dataset 34	92
A.6	Average and standard deviation of average radius (mm) for dataset 35	93
A.7	Average and standard deviation of average radius (mm) for dataset 36	93
A.8	Average and standard deviation of average radius (mm) for dataset 37	94
A.9	Average and standard deviation of average radius (mm) for dataset 38	94
A.10	Average and standard deviation of average radius (mm) for dataset 39	95
A.11	Average and standard deviation of average radius (mm) for dataset 40	95
B.1	Average and standard deviation of average residual (mm) for dataset 30	96
B.2	Average and standard deviation of average residual (mm) for dataset 31	97
B.3	Average and standard deviation of average residual (mm) for dataset 32	97
B.4	Average and standard deviation of average residual (mm) for dataset 33	98
B.5	Average and standard deviation of average residual (mm) for dataset 34	98
B.6	Average and standard deviation of average residual (mm) for dataset 35	99
B.7	Average and standard deviation of average residual (mm) for dataset 36	99
B.8	Average and standard deviation of average residual (mm) for dataset 37	100
B.9	Average and standard deviation of average residual (mm) for dataset 38	100
B.10	Average and standard deviation of average residual (mm) for dataset 39	101
B.11	Average and standard deviation of average residual (mm) for dataset 40	101
C.1	Average and standard deviation of average radius (mm) for dataset 60	102
C.2	Average and standard deviation of average radius (mm) for dataset 61	103
C.3	Average and standard deviation of average radius (mm) for dataset 62	103
C.4	Average and standard deviation of average radius (mm) for dataset 63	104
C.5	Average and standard deviation of average radius (mm) for dataset 64	104
C.6	Average and standard deviation of average radius (mm) for dataset 65	105
C.7	Average and standard deviation of average radius (mm) for dataset 66	105
C.8	Average and standard deviation of average radius (mm) for dataset 67	106
C.9	Average and standard deviation of average radius (mm) for dataset 68	106
C.10	Average and standard deviation of average radius (mm) for dataset 69	107

C.11	Average and standard deviation of average radius (mm) for dataset 70	107
D.1	Average and standard deviation of average residual for dataset 60	108
D.2	Average and standard deviation of average residual for dataset 61	109
D.3	Average and standard deviation of average residual for dataset 62	109
D.4	Average and standard deviation of average residual for dataset 63	110
D.5	Average and standard deviation of average residual for dataset 64	110
D.6	Average and standard deviation of average residual for dataset 65	111
D.7	Average and standard deviation of average residual for dataset 66	111
D.8	Average and standard deviation of average residual for dataset 67	112
D.9	Average and standard deviation of average residual for dataset 68	112
D.10	Average and standard deviation of average residual for dataset 69	113
D.11	Average and standard deviation of average residual for dataset 70	113
E.1	Canopy area measurement (mm^2) from Yang's experiment (Datasets 30-40)	114
E.2	Canopy area measurement (mm^2) from Yang's experiment (Datasets 60-70)	115
E.3	Canopy area measurement (mm^2) from our experiment (Datasets 30-40)	115
E.4	Canopy area measurement (mm^2) from our experiment (Datasets 60-70)	116
F.1	3D stem volume measurement (mm^3) from Yang's experiment (Datasets 60-70)	117
F.2	Canopy area measurement (mm^3) from our experiment (Datasets 60-70)	118

List of Figures

3.1	The experimental setup used by Yang in the Transgenic lab no. 3 at the Biotron Experimental Climate Change Research Center, the University of Western Ontario	23
3.2	Steps related to the proposed methodology	28
3.3	Stages related to the automation of the registration process	29
3.4	Segmentation of plant data	33
3.5	Replacement of the semi-spheres with the full sphere data	35
3.6	Reconstruction of views	36
3.7	Steps related to the overall registration process	42
3.8	3D polygon mesh generated from the registration phase	43
3.9	Pictorial illustration of problems with the manual editing before measuring plant growth	43
3.10	Illustration of the volume measurement processing using 65 th dataset	44
3.11	The first 6 original range images of the 30 th dataset showing the <i>Arabidopsis thaliana</i> plants at different views	48
3.12	The rest of the 6 original range images of the 30 th dataset showing the <i>Arabidopsis thaliana</i> plants at different views	49
3.13	Demonstration of the semi-sphere and plant data segmentation phase and the replacement of semi-spheres with full sphere data phase using the 1 st view of the 30 th dataset	50
3.14	The reconstructed views of the first 6 range images of the 30 th dataset	51
3.15	The reconstructed views of the rest of the 6 range images of the 30 th dataset	52
3.16	The first 6 reconstructed views of the 30 th dataset after performing the <i>Convert to Points</i> , <i>Sample</i> , and <i>Detect Sphere Targets</i> operations in Geomagic	53

3.17	The second 6 reconstructed views of the 30 th dataset after performing the <i>Convert to Points, Sample, and Detect Sphere Targets</i> operations in Geomagic	54
3.18	Illustration of the registration phase using all the 12 views of the 30 th dataset	55
3.19	The first 6 original range images of the 60 th dataset showing the <i>Arabidopsis thaliana</i> plants at different views	56
3.20	The rest of the 6 original range images of the 60 th dataset showing the <i>Arabidopsis thaliana</i> plants at different views	57
3.21	Demonstration of the semi-sphere and plant data segmentation phase and the replacement of semi-spheres with full sphere data phase using the 1 st view of the 60 th dataset	58
3.22	The reconstructed views of the first 6 range images of the 60 th dataset	59
3.23	The reconstructed views of the rest of the 6 range images of the 60 th dataset	60
3.24	The first 6 reconstructed views of the 60 th dataset	61
3.25	The second 6 reconstructed views of the 60 th dataset	62
3.26	the synthesized 3D polygonal mesh obtained from dataset 60 using “Global Registration” tool in Geomagic	63
4.1	Illustration of the experimental setup used by Yang for measuring the “wet volumes” of one of the plants in the lab	66
4.2	Problems with the manual pre-processing of the 3D triangular mesh .	67
4.3	Illustration of the radius measurement process of one of the reference spheres using electronic caliper	68
4.4	3D triangular meshes of the Arabidopsis plants for four different nights	78
4.5	Growth patterns of the Arabidopsis plants showing the changes in the canopy surface area for datasets 30-40	79
4.6	Growth patterns of the Arabidopsis plants showing the changes in the canopy surface area for datasets 60-70	80
4.7	Graphical representation of the comparison of canopy surface area measurement between the proposed (automated) method and Yang’s method for 4 different lines of the Arabidopsis plants (datasets 30-40)	81
4.8	Graphical representation of the comparison of canopy surface area measurement between the proposed (automated) method and Yang’s method for 4 different lines of <i>Arabidopsis thaliana</i> plants (datasets 60-70)	82

4.9	Pictorial explanation of the negative peaks in the growth rate of canopy surface area among the datasets 60-70	82
4.10	Growth patterns of the Arabidopsis plants showing the changes in the 3D stem volume for datasets 60-70	83
4.11	Graphical representation of the comparison of 3D stem volume measurement between the proposed (automated) method and Yang's manual method for 4 different lines of the Arabidopsis plants (datasets 60-70)	83
4.12	Difference between Yang and our automatic pre-processed stem used in measuring 3D stem volume	84

Chapter 1

Introduction

This chapter briefly outlines the problems tackled by this thesis and the motivation for this research. The main contributions of the thesis are summarized and the thesis outline is also presented here.

For the last few decades, plant scientists, genetic engineers, and bio-technologists have been working together to develop genetically modified seeds to increase the productivity of plants as well as to find more means of their use as renewable resources. It is important for them to be able to measure the 3D growth, both quantitatively and non-invasively, to see the effects of genetic alteration on the plants. Currently, this is a difficult task as the observation depends on subtle organic changes.

Traditionally, three types of quantitative measurements have been used to determine plant growth; namely, interferometry methods, mechanical methods, and computer vision methods. Interferometry methods [1, 2], being non-contact and non-invasive, require a complex mirror setup and are capable of measuring 3D information but only for a small number of points on the plant, which is insufficient in most cases. Mechanical methods [3, 4], on the other hand, require transducers to be attached to the plant; not only is this invasive but the 3D information is only provided at the transducers' locations. Moreover, the effects of the transducers' contact on the plant is still undocumented. Computer vision methods, especially, 2D and 3D optical flow [5, 6, 7, 8, 9] or 3D range flow [9, 10, 11, 12, 13, 14], are non-contact and non-intrusive, more accurate, and relatively inexpensive (i.e., usually require relatively low-priced equipment like cameras and computers). Optical and range flow methods can provide dense growth, leaf motion and leaf expansion measurements. But problems associated with flow approaches include that local rigidity is assumed and that the lighting must be fixed. Moreover, the acquisition rate for the data must be adequate (e.g., 15-30 images per second for image data and 1 scan every 2-3 minutes for range data).

In this thesis, instead of using optical or range flow methods, we used a number of 3D range scans (2D image with depth information of points in a scene from a

specific point) of a plant (*Arabidopsis thaliana*), taken from different viewpoints, to reconstruct a 3D polygonal mesh of it. ShapeGrabber range sensor is used to acquire the scanned data and to merge these scans into 3D polygonal meshes, we use Geomagic Studio 12 CAD software. Then, from these polygonal meshes, canopy surface areas and 3D stem volumes are computed to determine the plant’s growth over a time cycle. 12 range images of the Arabidopsis plant(s) are acquired as they are rotated 30° about their center on a circular table. The range sensor is at a fixed location with its line-of-sight towards the plant(s). Such 12 range images together make up a single dataset indicating the plant’s growth in a particular time over its entire growth cycle. To perform the registration process in Geomagic, 6 ping pong balls are used as reference spheres and each adjacent range image must have at least 3 or more common spheres visible. These reference spheres are imaged as semi-spheres in the original range images (as the laser scanner can only see those parts of an object that are visible from its line-of-sight). However, Geomagic requires full spheres and not semi-spheres for its registration of adjacent images. Thus, to date, Zhao [15] and Yang [16] manually replaced these semi-spheres with artificially generated spheres using Geomagic. This is a tedious and error prone task. One of the major contributions of this research is to automatically generate synthetic spheres, detect and localize the semi-spheres, and then to replace them with the “perfect” full sphere data inside the original range images. After the pre-processing, the merging (registration) is accomplished on these modified range data to generate 3D polygonal meshes so that they can be further used to quantitatively measure plant growth.

1.1 Problem Statement

This research is a continuation of the work done by Zhao [15] and Yang [16]. In their theses, Zhao and Yang used the following three steps to obtain the synthesized 3D polygonal meshes from the 3D range images:

1. In order to merge each 3D range image properly, ping pong balls were used as the reference spheres.
2. From every dataset, consists of 12 raw range images, a single 3D synthesized polygonal mesh was generated.
3. Before performing the quantitative analyses, unwanted artifacts (e.g., the background circular table, the pot(s), and soil) were trimmed away. The reference spheres were also removed before the 3D polygonal meshes were computed.

The aforementioned approach has some major drawbacks:

1. First, the whole procedure was performed manually, requiring large time resources. For instance, it took more than 4 hours for Yang to complete the registration process for a single dataset and she used 75 datasets to measure the overall growth cycle of a set of *Arabidopsis thaliana* plants. Moreover, another three weeks were needed to process the synthesized 3D polygonal meshes, resulting from the registration, before measuring plant growth from them.
2. Second, the raw range images generated by the ShapeGrabber laser scanner (3PI files) are generally large in size, ranging from 30-50 MB. To construct a single scene, both Zhao and Yang used 12 range images that had to be aligned and merged together. Because of this large dataset, the registration process consumed much manual and computational time.
3. Third, it should be emphasized, considerable manual labor was required throughout the registration process due to the incompleteness of 3D range data, specially the reference spheres. Because of this, automation of the registration process using Geomagic Studio 12 was difficult. We describe these difficulties in more detail:
 - One of the main problems with the reference spheres is that there were “holes” in the data where part of the surface is inadequately sampled. The specular reflectance property of the polished surface of the reference spheres could be one of the reasons for this incompleteness of the range data. It is possible that due to the specular reflective property of the reference spheres, the ShapeGrabber sensor failed to measure adequate surface information for the reference spheres.
 - As Yang mention in her thesis, ShapeGrabber SG1002 3D scanner (used during the experiment), was not able to clearly capture the target objects under bright visible light as its red laser beam is 660 nm, which is in the visible spectrum. Although, to minimize the interference with the visible spectrum light (e.g., daylight), Yang conducted the experiment between 8:00 P.M. to 8:00 A.M. daily.
 - Moreover, occlusion of reference spheres via plant foliage can be observed in many of the later range images during the flowering stage of the plant growth. Due to this phenomenon, the scanner sensor was unable to fully capture the target spheres.
 - Since the range sensor can only see the 3D environmental points that are visible from its line-of-sight, only semi-spheres (or less) was recovered in a single scan.

Because of these aforementioned reasons, Geomagic Studio 12 was unable to detect the semi-spheres as reference objects during the registration process automatically, as full sphere surface data are needed. To solve this, Zhao and

Yang drew a boundary around the incomplete semi-spheres manually and used Geomagic’s “Best Fit” tool to fit a perfect sphere to incomplete semi-sphere points. The accuracy of this fit in Geomagic fully depends on the initial manual selection of the boundary area. The manual enhancement of semi-spheres was performed on each visible semi-sphere in the 12 views of each dataset. Even after this manual enhancement, further manual assistance was needed for Geomagic to accomplish “Target Registration”. Both Zhao and Yang opened all the 12 views of each dataset in Geomagic’s “Display Manager” and manually rotated them to find out the matching pair of spheres in adjacent range scans. They did this for all the visible spheres in a dataset as Geomagic needs to know these information to merge these images properly. In brief, they manually aligned them before performing “Target Registration” in Geomagic. Yang performed this tedious manual alignment on all 75 of her datasets. Because of these reasons, the full automation or semi-automation of the registration process is very desirable. Therefore, the main goal of this thesis is to automate the registration process to reduce human interaction and to increase speed and accuracy of quantitative plant growth analysis.

1.2 Motivation

In the past, quantitative plant growth was made by using “wet” volumes (submerging a plant in a large container with a known amount of water and measuring the volume displacement of the water) that resulted in the destruction of the plant or using transducer which measured leaf motion and (maybe) plant elongation (the effect of the contact of the transducer and the plant is unknown till to the date). These days, with genetic modification of a plant, it is more important than ever to be able to quantitatively measure the 3D growth of a plant in a non-invasive and non-contact manner. Moreover, the rapid growth of plant science increases the demand of this kind of quantitative measurement of plant growth. In their theses, Zhao and Yang tried to provide a plant growth measurement system using ShapeGrabber laser scanner and Geomagic Studio. However, due to numbers of reasons (section 1.1), such as the incomplete 3D range data, the absence of Geomagic macros (i.e., to automate Geomagic button pressing and other selection-based action), they were unable to provide a complete or even semi-automatic registration process. As a result, the growth measurement process of *Arabidopsis thaliana* became very time consuming and less accurate than desired. So, the main motivation of this thesis is to fully automate the registration process to provide a self-sustained and more accurate tool for the registration process.

1.3 Thesis Contributions

The major contribution of this thesis is the automation of the entire registration process. To do this, the following associated goals are accomplished.

1.3.1 Generating Full Sphere from Semi-sphere Data

The reference spheres data inside the original 3PI files are incomplete. The reasons for this incomplete data include the specularly on the reference spheres (i.e., the ping pong balls). Specular reflection reflects the laser ray away from the scanner’s sensor. As a result, it is possible that the laser sensor failed to collect any information for that surface area. Secondly, because the growth pattern of the plants cannot be anticipated in the earlier stages of its growth, possible occlusion of reference spheres may occur via plant foliage, specially, during the flowering stage. Lastly, the laser scanners cannot scan the surface of any object that is not visible from its line-of-sight (e.g., the back faces of the reference spheres). Unfortunately, Geomagic Studio 12 cannot register the range images automatically without full sphere data. In their theses, Zhao and Yang manually fitted spheres to incomplete semi-spheres data using Geomagic’s “Best Fit” tool. However, to overcome this problem automatically, we detect the center and radius of each reference sphere in the original 3D range data using parameter estimation techniques, namely, least-squares algorithm and M-Estimation for sphere fitting. Then using these estimated values as well as the parametric equation of sphere, the 3D sphere co-ordinates are generated. Last of all, to reconstruct each view, the incomplete semi-sphere data are replaced by the newly generated full sphere inside the range images.

1.3.2 Automating the Registration Process using Geomagic Macros

Because registration was manually performed previously, continuous observation and attention was required, which is both tedious and exhausting. By developing macros to perform all the actions in Geomagic, we nearly automate the whole registration process by reducing the need for human interactions. Macros in Geomagic are set of user-defined instructions that are used to eliminate human interaction during repetitive tasks or steps. In Geomagic, macros can be written using VBScript, Python and Javascript. We use VBScript to write these macros that perform Geomagic’s registration process in a number of steps, without requiring selection-based actions (e.g., mouse clicks for selecting a particular tool). In addition, these macros can save the output files in user defined directories for future processing. This use of macros therefore eliminates the laborious human effort used before.

1.3.3 Improving Speed and Accuracy

As the original 3PI files have incomplete reference spheres (just the front faces with holes), the detection of targets for registration as well as the registration process itself are significantly slow. The automation of Geomagic’s registration process, accomplished in this thesis, can be shown to be a very useful tool for quantitative plant growth measurement, leading to significant computational speedup and a more accurate quantitative analyses of plant growth.

Overall, the main goal of this thesis is not to measure the plant growth at the different stages of its growth as Zhao and Yang did in their theses, but to provide a self-sustained infrastructure for the overall registration process using Geomagic Studio 12. We believe that this automation of the registration process is a good first step towards a fully automated system of 3D plant growth measurement.

1.4 Thesis Outline

The remainder of this thesis is structured as follows:

Chapter 2 summarizes the literature survey. This chapter provides a general overview of various parameter estimation techniques because we need to fit a sphere to semi-sphere data by estimating its center and radius. In addition, it surveys some of the recent activities of plant growth measurement using 3D computer vision techniques.

Chapter 3 introduces the proposed methodology used in this thesis. We outline the algorithms applied to the raw range images to overcome the problems stated in Section 1.1. Moreover, this chapter also discusses the macros used to automate the registration process, as well as all the steps needed in the quantitative analyses of the 3D growth measurement of *Arabidopsis thaliana* plant using Geomagic Studio 12.

Chapter 4 presents a detailed analysis of experimental application of our algorithm to some of Yang’s range datasets. This chapter includes a performance analysis of the algorithms used to estimate sphere center and radius. Also, we measure canopy surface area and 3D stem volume of *Arabidopsis* plants from some of Yang’s range datasets using our approach and compare the experimental outcomes with Yang’s results.

Finally, Chapter 5 concludes the thesis and gives future research directions.

appendix A provides estimated average radius and standard deviation of the target spheres of datasets 30-40 using LS, Huber and Bisquare. appendix B shows average residual and standard deviation of datasets 30-40 using LS, Huber and Bisquare. In appendix C we have estimated average radius and standard deviation of the target spheres of datasets 60-70 using LS, Huber and Bisquare. Average residual and

standard deviation of datasets 60-70 using LS, Huber and Bisquare can be found in appendix D. Whole Plants Surface Area Measurement From Yang and Our Experiment are displayed in appendix E. appendix F shows 3D Stem Volume Measurement From Yang Our Experiment. The macros, written in VBScript, used to Automate Various Geomagic's Tools to eliminate human interaction can be found in appendix G.

Chapter 2

Literature Review

This chapter provides a general overview of the various parameter estimation techniques widely used in Image Processing and Computer Vision. It also reviews some of the literature on quantitative plant growth measurement using 3D imaging technology.

2.1 A General Overview of Parameter Estimation Techniques

Estimation theory is a discipline in Statistics and signal processing that provides tools to deal with the computation of multi-dimensional parameter values from experimental data. Parameter estimation theory is often used in the field of Image Processing and Computer Vision. But for the last few decades, the overwhelming growth of 3D imaging systems and 3D CAD software makes parameter estimation techniques even more important. These techniques have become an important component in many applications in Image Processing and Computer Vision, which depend on some form of geometric feature detection and estimation from measured data.

Most parameter estimation problems, generally, can be visualized as a combination of the following four features [17]:

1. **Criterion:** The selection of the best optimization function, which can possess either a minimization or a maximization criterion.
2. **Estimation:** The choice of best method to optimize the chosen objective function.
3. **Design:** Efficient and optimal implementation of the chosen method in order to achieve the best result from the objective function.

4. **Modeling:** The determination of the mathematical model best describing the system and the error in the measurement.

Assume that \mathbf{p} is the m dimensional vector containing the parameters to be estimated, If the system is noise-free, then the output vector \mathbf{z} can be represented as a vector function, \mathbf{f} , which relates \mathbf{z} to \mathbf{p} as follows:

$$\mathbf{f}(\mathbf{p}, \mathbf{z}) = 0. \quad (2.1)$$

Because, in practice, a system is never noise-free, observed measurements \mathbf{y} (e.g., the noisy input vector) are only available for \mathbf{z} corrupted with noise, ϵ :

$$\mathbf{y} = \mathbf{z} + \epsilon. \quad (2.2)$$

Usually, a number of measurements, \mathbf{y}_i ($i = 1, \dots, n$), are taken for the system and the parameter vector \mathbf{p} is estimated using \mathbf{y}_i . As the measured data is noisy, Eq. 2.1 does not hold and we need to derive a new function F that relates \mathbf{y}_i to \mathbf{p} :

$$F(\mathbf{p}, \mathbf{y}_1, \dots, \mathbf{y}_n). \quad (2.3)$$

Usually, Eq. 2.3, known as the *cost function* or the *objective function*, needs to be optimized to find the best solution according to some criteria (or constraints). If there are no constraints on \mathbf{p} and the function F has first and second order partial derivatives, the necessary conditions for a minimum to exist are given by Eq. 2.4 and 2.5 as follows:

$$\frac{\partial F}{\partial \mathbf{p}} = 0 \quad (2.4)$$

and

$$\frac{\partial^2 F}{\partial \mathbf{p}^2} > 0. \quad (2.5)$$

Therefore, the basic idea of parameter estimation is to minimize the cost function while satisfying various constraints if applied.

2.2 Basic Categories of Parameter Estimation

Parameter estimation techniques can be subdivided into two main categories:

1. Least-Squares Fitting and
2. Robust Estimation.

In this thesis, our main target is the problems related to sphere fitting using multidimensional range data, most of the mathematical models and examples, used in this chapter, are based on sphere.

2.2.1 Least-Squares Fitting

Because of the simplicity of its computation, Least Squares (hereinafter referred to as LS) is one of the most widely used parameter estimation methods. Based on differences in the error function, LS methods can be divided into two main categories:

1. Algebraic Techniques and
2. Geometric Techniques.

2.2.1.1 LS Fitting Based on Algebraic Techniques

Algebraic fitting is based on an implicit equation, $F(\mathbf{x}, \mathbf{p}) = 0$, with the parameter vector $\mathbf{p} = (p_1, p_2, \dots, p_q)$ describing the object to be fitted. In this method, the error is defined by the amount of deviation (residual) that violates the system of equations. The non-equality of the equation, $F(\mathbf{x}, \mathbf{p}) \neq 0$, indicates that the given points do not fully lie on the geometric feature.

The equation of a sphere having center at (x_0, y_0, z_0) and radius r is given by:

$$(x - x_0)^2 + (y - y_0)^2 + (z - z_0)^2 = r^2. \quad (2.6)$$

Substituting $x_0 = -\frac{a}{2}$, $y_0 = -\frac{b}{2}$, $z_0 = -\frac{c}{2}$ and $r^2 = \frac{a^2+b^2+c^2}{4} - d$ yields an alternative equation:

$$x^2 + y^2 + z^2 + ax + by + cz + d = 0. \quad (2.7)$$

In Eq. 2.7, the sphere is expressed in terms of linear parameters, a , b , c , and d . The center co-ordinates and the radius of the sphere can be estimated from these values. It should be noted that Eq. 2.7 only has geometric meaning if its parameters a , b , c , and d satisfy the constraint:

$$\frac{a^2 + b^2 + c^2}{4} - d \geq 0 \quad (2.8)$$

Otherwise, the resulting radius would not be a real number. If a data point, (x_i, y_i, z_i) , does not fully lie on a sphere, using Eq. 2.6 we can derive the definition of its deviation as follows:

$$\Delta_i = (x_i - x_0)^2 + (y_i - y_0)^2 + (z_i - z_0)^2 - r^2, \quad (2.9)$$

or equivalently, using Eq. 2.7 as:

$$\Delta_i = x_i^2 + y_i^2 + z_i^2 + ax_i + by_i + cz_i + d. \quad (2.10)$$

Eq. 2.11 below is the objective function for an algebraic function using the LS norm.

$$F_{Algebraic} = \sum_{i=0}^n (x_i^2 + y_i^2 + z_i^2 + ax_i + by_i + cz_i + d)^2, \quad (2.11)$$

where the LS norm of a vector is the magnitude of that vector, i.e. for $\mathbf{p} = p_1, \dots, p_n$, the magnitude of \mathbf{p} is given by $\|\mathbf{p}\|_2 = \sqrt{p_1^2 + \dots + p_n^2}$.

2.2.1.2 The Insufficiency of Algebraic Techniques

The algebraic distance based LS method is computationally efficient as the deviation function is linear in its parameters. However, in spite of this advantage, the results of algebraic fitting are often not satisfactory. Among the many disadvantages of algebraic fitting are [18, 19]:

1. Algebraic techniques are not reliable because of their high sensitivity towards noise. As a result, sometimes it is difficult to test the reliability of the estimated parameters as these values can be biased because of outliers,
2. The fitting errors are not properly weighted and the outliers can significantly influence the result, and
3. The fitting procedure may end up with an unintended geometric features (e.g., a hyperbola instead of an ellipse).

To overcome these problems, many researchers prefer to use geometric techniques instead.

2.2.1.3 LS Fitting Based on Euclidean Norm

Geometric fitting techniques are based on the actual *Euclidean* or the *shortest distance* of the measured sphere data. The original Euclidean distance of a data point (x_i, y_i, z_i) from the estimated sphere uses the computed center co-ordinates, (x_0, y_0, z_0) , and the computed radius r to measure the distance of this data point from the estimated sphere. The equation of deviation for geometric fitting is as follows:

$$\Delta_i = \sqrt{(x_i - x_0)^2 + (y_i - y_0)^2 + (z_i - z_0)^2} - r. \quad (2.12)$$

Using the LS norm, the objective function is defined as Eq. 2.13:

$$F_{Geometric} = \sum_{i=0}^n (\sqrt{(x_i - x_0)^2 + (y_i - y_0)^2 + (z_i - z_0)^2} - r)^2. \quad (2.13)$$

Although simple, the algebraic fitting is more sensitive to outliers than the geometric fitting while the latter is computationally more expensive than the prior. Geometric fitting is more robust and accurate than the algebraic fitting. So, if it can be known beforehand that the system is (relatively) free of noise, the LS method based on algebraic fitting may be the best option to use.

Variation and improvisation of the LS methods, both algebraic and geometric, can be found in many scholarly articles, many of which even attempted to improve their performances by getting over the shortcomings. In his paper, Zhang [17] discussed

the pros and the cons of the gradient weighted LS method. In case of ordinary LS method, optimal (in terms of minimum covariance) solution is promised if the errors are uncorrelated and their variances are constant. But in case of a system of equations having unequal variances, ordinary LS does not yield an optimal solution. In order to obtain a constant variance function, it is sufficient to divide the original function by its gradient and in that case, the gradient weighted LS proves to be effective. In the case of the gradient weighted LS method, the minimum of the sum of squares is found by setting the gradient to zero. However, the gradient weighted LS method, being a nonlinear minimization problem, does not provide a closed-form solution. Therefore, the estimated solution is only an approximation and in practice, iterative procedure needs to be run.

Both algebraic and geometric distance based LS methods consider only the values of co-ordinates of measured points and not the direction towards which those data points have been acquired using 3D imaging systems (e.g., laser scanners and optical range cameras). The geometric scan-directed method, a novel idea proposed by Witzgall *et al.* [20, 19], considers the values of co-ordinates of the measured points as well as the direction of acquisition. In their experimental setup, authors used a LADAR (LAsER Detection And Ranging) scanner, capable of generating millions of data points by sending out a laser signal and analyzing its reflection back to the instrument. Among the assumptions of the algorithm are that the data points are acquired in the direction of scan and the impact of a data point (x_i, y_i, z_i) on a sphere is found on a ray, referred to as “scan ray”, emanating from the instrument position, $(0, 0, 0)$ (origin), so that the intended target point lies at the intersection of the scan ray with the sphere. The scan ray, as it does not intersect the sphere, experiences a “miss”; otherwise, a “hit”. Although every data point, as it is in the dataset, arises from a hit. But as the sphere is not in best-fit position, misses are to be expected. The version of “directional” fitting reported by the authors distinguishes between two deviations based on “hit” and “miss”. The procedure deletes those “miss” points and minimize the point cloud. The full point cloud is then again screened for points that cause misses of the re-minimized sphere, and these points are deleted before the next re-minimization. This process is repeated unless the number of misses has stabilized. The objective is to stop at a sphere fitted to a stable set of data points all providing hits. Recent research shows that the proposed method, still subject to more experiments, successfully solves the sphere fitting problem. The experiment, conducted in this research, indicates that for certain applications it may not be enough to fit geometric features on the co-ordinates of points alone, but to consider the directions in which those points are acquired as well.

A robust, but simple, non-parametric algorithm based on geometric fitting for the LS method is proposed by Ahn *et al.* [18]. In their research, the authors developed an efficient technique for the fitting of any geometric structure including circles, spheres, ellipses, hyperbolas, and parabolas. The main achievement was to develop a com-

mon technique that is not feature specific (e.g., circle or sphere specific algorithm) rather than provides solution for many geometric features like circles, spheres, ellipses, hyperbolas and parabolas.

Fitzgibbon *et al.* [21, 22] can be named as pioneers for their proposed ellipse-specific algorithm. They designed a non-iterative fitting method specifically for ellipses. The method incorporates the ellipticity constraint, $4ac - b^2 = 1$ into a normalization factor by minimizing the algebraic distance. This algorithm always returns ellipse parameters even from data corrupted by significant noise. After the development of the Fitzgibbon *et al.*'s ellipse-specific fitting algorithm, Halir and Flusser [23] analyzed this algorithm. They characterized the drawbacks of Fitzgibbon *et al.*'s algorithm method and proposed improvements. The approach of Fitzgibbon *et al.* has both singularity and numerical instability problems often yielding a significantly incorrect solution. By decomposing and rearranging the constraint and scatter matrices, Halir and Flusser overcome the singularity problem. They evaluated their algorithm for a large amount of range data and their findings showed that their proposed approach preserved favorable properties such as a guaranteed ellipse specific solution and robustness against noise. In addition, their proposed method removes the numerical stability problem and yields reliable optimal solutions.

Gander *et al.* [24] examined both algebraic and geometric distance problems based on synthetic data for circles and ellipses. They reported that the latter are more stable although the former must be acknowledged for their simplicity. They concluded that the comparison between these two methods would not be very enlightening due to the absence of proper estimation or objective criterion. So, they experimented different non-linear algorithms (e.g., Gauss-Newton, Newton, Gauss-Newton with Marquardt modification, Variable projection, and Orthogonal distance regression) to compute the geometric fit with respect to stability and efficiency. The general conclusion based on a small dataset includes that these non-linear algorithms were expensive compared to algebraic solution, newton method was the most efficient of all. However, the variable projection algorithm was the most expensive and finally, for ellipse fitting problem, orthogonal distance regression algorithm was the most promising one.

One of the major drawbacks of the non-linear LS method is the randomized restarting needed to overcome the local minima or maxima. Most of these algorithms start with initial guesses for the parameters and then refine the values iteratively. This can result in unbounded running time for most non-linear LS algorithms. Burr *et al.* [25] used "inverse transformation" to overcome this problem along with the "stereographic projection". The first algorithm takes advantage of the property that for spheres that pass through the inversion point (i.e., if all the data points and inversion point lie on a sphere), the transformed points will lie on a plane. It follows that points distributed roughly on a sphere, with the least sum of squares fit sphere passing through the inversion point, will also lie near a plane. The key property taken advantage of in this algorithm is that points on a sphere in the d -dimensional normal space will lie on

a d -dimensional sphere on the $d + 1$ -dimensional hypersphere. In the case presented, points on a 3-sphere in \mathbb{R}^3 will lie on a 3-sphere on the 4-sphere in the transformed space. This 3-sphere defines a unique hyperplane in \mathbb{R}^4 , and can be easily found again using the technique of least squares fitting to a hyperplane. These proposed algorithms transform the non-linear unbounded problems in bounded time problems. Their experimental results showed that their proposed algorithm outperformed the current state-of-the-art algorithms and exhibited favorable time complexities even for high dimension parameter space.

Most papers on parameter estimation usually only focus on the problems related with estimation theory. However, Lukács *et al.* [26] addressed a more generalized problem of parameter estimation that includes two major problems to the date. First, finding the principal curvatures of the surfaces and second, fitting of that particular surface (as defined by these curvatures) to the measured data using a non-linear LS method. More precisely, the problem addressed by Lukács *et al.* can be decomposed into two logical steps; segmentation, where the data points are grouped into sets each belonging to a different surface and fitting, where the best surface of an appropriate type is fitted to each set of points. However, Lukács *et al.* report no major improvement of the LS method.

2.2.2 Robust Estimation

Unlike the classical statistical model, robust statistics models provide a means to think of alternative estimators that are not affected by large local deviations from the model (we call these “bad” data points, **outliers**, to distinguish them from **inliers**, the “good” data). More precisely, a robust estimator attenuates the effect of outliers on the computed results. These outliers could be a side-effect of deviations from assumptions or could be caused by measurement error. If the percentage of outliers is not too large (the break point) the computed solution using the robust estimator can have a reasonable efficiency and reasonably small bias (from the outliers). For example, the median is a robust measure of its central tendency, while the mean does not have this property. Another example consists of fitting a line to a collection of 2D points. If 99% of the points are close to a line with the correct slope and y intercept but 1% is wildly off (the outliers) then using traditional LS fitting will yield an incorrect solution for the slope and y intercept while a robust fitting will completely (nearly) suppress the effect of the outliers.

2.2.2.1 M-estimators

M-estimation [27, 28, 29, 30] is one of the most popular robust techniques that deals with the sensitivity of the LS regression to outliers in noisy data. These estimators are normally ignore unusual or deviated data. M-estimation method can also be regarded

as a generalization of maximum-likelihood estimation. M-estimation can be thought of as iterative weighted LS, where particular method decide the weight differently at each iteration.

Fox and Weisberg [28] described the robustness of M-estimators against noisy data. Earlier, Fox [27] experimented with and reported the performances of three famous M-estimators: namely, ordinary LS estimator (assuming that the errors be normally distributed), the Huber estimator and the Turkey Bisquare or Biweight estimator. The authors also compared the results based on their objective functions and corresponding weight functions. Table 2.1 shows the objective and weight functions for these three aforementioned robust estimators.

Method	Objective Function	Weight Function
LS	$\rho_{LS}(e) = e^2$	$\omega_{LS}(e) = 1$
Huber	$\rho_H(e) = \begin{cases} \frac{1}{2}e^2 & e \leq k \\ k e - \frac{1}{2}k^2 & e > k \end{cases}$	$\omega_H(e) = \begin{cases} 1 & e \leq k \\ \frac{k}{ e } & e > k \end{cases}$
Bisquare	$\rho_B(e) = \begin{cases} \frac{k^2}{6} \left\{ 1 - \left[1 - \left(\frac{e}{k} \right)^2 \right]^3 \right\} & e \leq k \\ \frac{k^2}{6} & e > k \end{cases}$	$\omega_B = \begin{cases} \left[1 - \left(\frac{e}{k} \right)^2 \right]^2 & e \leq k \\ 0 & e > k \end{cases}$

Table 2.1: Objective function and weight functions of the LS, Huber and Bisquare estimators [27]

Table 2.1, as described by Fox, shows that the values of the objective functions for OLS and Huber, increase without bound as the residual e departs from 0. However, the change in the rate of increase is more drastic for the OLS than Huber estimator. In contrast, the Bisquare objective function values eventually level off (for $|e| > k$). One of the major drawbacks of OLS estimator is that it assigns equal weight for every observation. But for Huber and Bisquare estimators these weights are adaptive. The value k for the Huber and Bisquare is known as the tuning constant. The smaller the k value, the more resistance there is against outliers. But in the case of a normal or Gaussian error distribution, a smaller k value results in higher expense for both Huber and Bisquare estimators. This is one of the major problems with these two M-estimators. So, in practice, to reduce the case, the value of k is assigned as $k = 1.345\sigma$ and $k = 4.685\sigma$ for the Huber and Bisquare estimators, respectively (where σ is the standard deviation of the normal error distribution). It may be noteworthy that in case of normal error distribution, OLS estimator provides the optimal solution and computationally less expensive than the other two.

Zhou *et al.* [29] proposed a sphere center detection algorithm based on M-estimation to avoid the ambiguity and inaccuracy results reported for the LS method when the error distribution is not normal. Zhou *et al.* claimed that most of the state-of-art algorithms for positioning the center coordinates of the spherical target are

based on the LS method and thus are vulnerable to outliers as there is no guarantee that the error distribution of a system is always normal. In practice, due to specular reflectance property, occlusions and accessibility limitations of parts of a surface, point clouds may exhibit a large number of outliers and the estimated results can be radically inconsistent. Most of the state-of-art algorithms that use standard LS methods, focus on the minimization of sum of the squared residuals, $\sum_i r_i^2$, but Zhou *et al.* reduced the effect of outliers by replacing this function with another weighted function:

$$\min \sum_i \omega(r_i) r_i^2, \quad (2.14)$$

where ω is a weight function, the r_i are the residuals and σ is the standard deviation of residuals. Among many weight functions, the authors choose the one proposed by Professor Zhou Jiangwen [31] as ω^1 . The aforementioned weight function, ω , ensures that if the resulting residual of data exceeds a certain limit that is 2.5 times larger than the standard deviation, the data are regarded as outliers. Therefore, the corresponding weight is set to zero so that the data has no effect on the estimated value(s). Because of the adaptive nature of the weight functions, the M-estimation based methods are more robust and reliable than the LS methods in most cases.

2.2.2.2 Bounded-Influence Estimators and MM-estimators

Although M-estimator is a popular robust method for dealing with outliers, it can be vulnerable to high-leverage observations. Basically, leverage implies how far away a value of the independent variable is from the mean value. The farther away the observation, the more leverage it has. To avoid this kind of unexpected phenomenon, bounded-influence estimators [17, 28] like least-trimmed squares (LTS) regression have been proposed to setup higher breakdown point than M-estimators. For LS methods, solution is achieved by minimizing sum of squared residuals over n points. However, instead of minimizing the sum of squared residuals over n points, a subset of those points (k , for example), are used. The $n - k$ points with the largest residuals are excluded so that they do not influence the estimation. However, the method being binary (the data points are either included or excluded), no closed form solution exists. Therefore, finding a LTS solution is basically done by finding the subset k , that provides the lowest sum of squared residuals among every possible combination from n points. As a result, as n increases, the number of combinations grows rapidly which is one of major problems with LTS estimator. However, LTS estimator has

$$\omega_i = \begin{cases} 1 & |r_i| \leq 1.5\sigma \\ \frac{1.5\sigma}{r_i} & 1.5\sigma < |r_i| \leq 2.5\sigma \\ 0 & 2.5\sigma > |r_i| \end{cases}$$

where r is the residual and σ is the standard deviation of residuals. The function implies that if the r is 2.5 times larger than σ , the data are regarded as outliers. In such cases, to nullify the effect, the corresponding weight is set to zero, or else, different weight is given to each data point.

proved to be an efficient starting point for M-estimators. The M-estimation, along with the use of a bounded-influence estimation to provide initial guess, is often called MM-estimation [28]. The MM-estimators are more attractive than the M-estimators as they retain the high break-down point property (nearly 50%) of the bounded-influence estimator as well as share the efficiency of M-estimators.

2.2.2.3 L_1 Regression

In general, L_1 regression [28] attempts to minimize the sum of the absolute errors (the L_1 norm). On the other hand, L_2 regression (OLS regression), minimizes the sum of the squared errors (the L_2 norm). As a result, L_1 regression provides much less weight to large deviations or outliers. Because of the nature of the error function, L_2 regression is more sensitive towards noise than L_1 regression.

2.2.2.4 Regression Diagnostics

Regression diagnostics is one of the oldest methods for robust estimation [32]. This method attempts to eliminate data that are possibly wrong and reject them by an analysis of a globally fitted model in an iterative manner. Zhang [17] discussed the pros and cons of this method. He noted that the major problem of this method is to find a quality initial guess, as the success of this estimation method depends on it. Similar to the Bisquare estimator, a poor initial guess for Regression diagnostics may lead to failure of rejecting the outliers. As a result, this technique does not always guarantee a correct solution. However, Zhang noted that the regression diagnostics technique works well for problems with a moderate percentage of outliers.

2.2.2.5 Least Median of Squares (LMedS) Estimators

The least median of squares (LMedS) method estimates the parameters by solving the nonlinear minimization problem:

$$\min (\text{median}_i r_i^2), \quad (2.15)$$

where r is the residual. Unlike LS, this estimator yields the minimum value of the median of the squared residuals rather than finding the minimum sum of squares. Zhang [17] discussed both the advantages, robustness toward outliers, and the disadvantages, impossible to convert to a weighted LS problem, of the LMedS estimator.

It is noteworthy that most of these aforementioned robust estimators were developed between the mid-1960s and the mid-1980s. The literature show that among these estimators, the M -estimators, the MM-estimators and the L_1 estimators are the most widely used ones.

2.3 Recent Plant Growth Measurement Techniques using Computer Vision

As mentioned in Chapter 1, to measure plant growth, plant researchers use three types of measurement techniques:

1. Interferometry Methods,
2. Mechanical Methods, and
3. Computer Vision Methods.

In their MSc theses, Zhao [15] and Yang [16] discussed these three methods, their uses, their advantages and disadvantages, and some of the research where these methods have been applied. So, to avoid repetition, we are not going to discuss these methods here. However, Table 2.2 taken from Yang [16] is presented here to provide a quick overview of these three methods by summarizing their representative examples and describing their major advantages and disadvantages.

Approaches	Benefits	Limitations	Citations
Interferometry	<ul style="list-style-type: none"> • Non-contact • Non-invasive • Micron accuracy 	<ul style="list-style-type: none"> • Requires complex setup with mirrors and lasers. • Performs measurement at 1 or a few points. • Unable to measure leaf motion. 	Fox and Puffer [1, 2] Jiang and Staudte [33] Dyrseth [34] Kadono <i>et al.</i> [35]
Mechanical Transducers	<ul style="list-style-type: none"> • Simple • Low complexity 	<ul style="list-style-type: none"> • This is not a non-contact method. • Only 1 or few points can be measured. 	Lang [3] Pasumarty <i>et al.</i> [4] Lüthen <i>et al.</i> [36]
Computer Vision Approaches	<ul style="list-style-type: none"> • 3D and non-invasive • Non-contact • Required inexpensive equipment • Micron accuracy • Uses range images • Able to measure leaf expansion • Provides dense growth measurement 	<ul style="list-style-type: none"> • Sensitive to lighting condition and vibration. • The sequences of the range images must be differentiable. 	Barron and Liptay [5, 6] Liptay <i>et al.</i> [37] Aboelela <i>et al.</i> [38] Spies <i>et al.</i> [39, 40, 41, 42, 43] Ortiz-Uribe <i>et al.</i> [44]

Table 2.2: Advantages and disadvantages of three approaches to measure quantitative plant growth [16]

It is noteworthy that Zhao and Yang first used 3D volume and 3D areas from merged 3D laser range scans to measure the growth cycle of *Arabidopsis thaliana*. Some recent articles have appeared on using range scanning to measure plant growth. Apart from this, detail discussion on other categories of plant growth measurement techniques can be found in Zhao and Yang’s theses.

An accurate system of plant growth measurement is an essential part of most of the experiments that investigate the effects on plants due to altered environmental factors. The traditional approach is to harvest a subsample of the test plants over time (which is time consuming and requires a large number of replicated plants while suffering from the fact that the harvested individual trees can no longer be used for further growth study). An alternative non-destructive approach is to monitor the subtle organic changes in plants over time using allometric relationships [45]. However, a significant amount of time and labor is also required to record various variables (e.g. plant height and twig and branch length) for a large number of trees.

Keightleya and Bawden [46] measured the wood volume of *Vitis vinifera* plants (commonly known as grape vines), from the images derived using a tripod mounted laser scanner and compared the results with standard biological water submersion measurements. From digital calculations, the plant volume was measure using the combinations of 2, 3, 4, 6 and finally, 10 scans and likewise, volume measurements was made by submerging the vine trunks and cordons in water and measuring the displacement. Experimental results showed that standard error for the digital technique dropped rapidly as additional scans were added to volume calculation. Interesting enough that similar phenomenon is also reported by Zhao and Yang. Also, in both cases, the estimated digital volumes were greater than those of water submerged volumes, this method reveals a new, rapid and non-destructive method to remotely measure standing biomass.

Seidel *et al.* [47] experimented with 63 potted juvenile *Fagus sylvatica* L. trees by measuring total above-ground biomass, the biomass of axes (e.g., stems and twigs) and the total leaf area. To do so, they used a portable 3D laser scanner (the ZF Imager 5006) along with the phase difference (interferometry method). They used a relationship between total number of detected hits for a tree and the tree’s biomass. The major target of this experiment was to test the potentiality of the proposed method for measuring the above-ground biomass and compare the results against traditional biomass harvests and other established allometric estimates of biomass. Experimental results showed that growth measurements using a laser scanner has good correlation with above-ground biomass. The results were more accurate for plants with leaves rather than for defoliated plants and this is also the case with Zhao and Yang. Their experimental outcomes were more accurate for the vegetative stage rather than the flowering stage of *Arabidopsis thaliana*. However, their proposed method outperformed other alternative non-destructive methods. They also showed that 3D laser scanning is a promising technique for the non-destructive monitoring of

biomass and growth in young trees. The main aim of this research was to verify the feasibility of using TLS to measure the biomass and volume of grape vines.

With recent advances in 3D imaging instrumentation and software, 3D laser scanning has become a common method for the optical measurement of the 3D objects. As a result, 3D imaging techniques are now being put to use for research in the plant sciences for evaluating plant growth. Some of these articles, reported by Keightleya and Bawden and Seidel *et al.*, are briefly mentioned here. Hosoi and Omasa [48] used a portable 3D laser scanner to calculate canopy leaf area density profiles for deciduous trees. Watt *et al.* [49] measured total tree height and the tree's biomass using allometric relationships (differential growth rates of the parts of a living organism's body) based on the terrestrial laser scanner data. On the other hand, Lim and Treitz [50] used Airborne laser scanners to derive trees biomass.

2.4 Conclusion

In this chapter, various parameter estimation techniques, mainly LS and robust estimation techniques, were surveyed and their advantages and disadvantages stated. Finally, some of the recent achievements in the field of plant growth measurement using 3D laser scanning were presented.

Chapter 3

Experimental Methodology

This chapter outlines the pre-processing methods applied on each view of the raw range images so that Geomagic Studio 12 can automatically create synthesized 3D polygon meshes from them and then measure the canopy surface areas and 3D stem volumes from the merged images of the Arabidopsis thaliana plant.

In this thesis, we use the range images collected from the 3D scans of the *Arabidopsis thaliana* plants using ShapeGrabber SG1002 laser range scanner. These images were recorded by Yang [16] in 75 datasets. Each dataset consists of 12 range scans of 4 pots of plants (wild type, pBI 121 plasmid control, and two genetically modified lines called 10^4 and 3^1). These pots were placed on a rotating platform. The range scanner was positioned about 30 cm from the plants with a view angle of roughly 45° . The platform was rotated by 30° increments, showing the plant at 12 different views about a full 360° rotation. 30° rotational increments provided different views of the plants but had significant overlap of the plants' body in the adjacent views, allowing Geomagic to merge these scans to construct 3D model of the plants. Merging these views allowed a triangular mesh of the plants to be constructed from which plants growth can be measured. The merging process required that there be at least 3 common visible reference spheres in each set of adjacent views. Six reference spheres were used to guarantee this condition. Figure 3.1 shows the experimental setup used by Yang.

After Yang scanned the images, she calculated the canopy surface areas (leaves are not flat, for example) and 3D stem volumes of the plants using the triangular meshes computed from each dataset of 12 scans. This calculation of a triangular mesh from 12 raw 3D range images was achieved by a *manual* registration process using Geomagic Studio. The reasons behind the choice of manual registration for Yang are mentioned in Section 1.1. However, two major problems are invoked due to this approach:

- First, it requires human interaction that can introduce significant errors to the

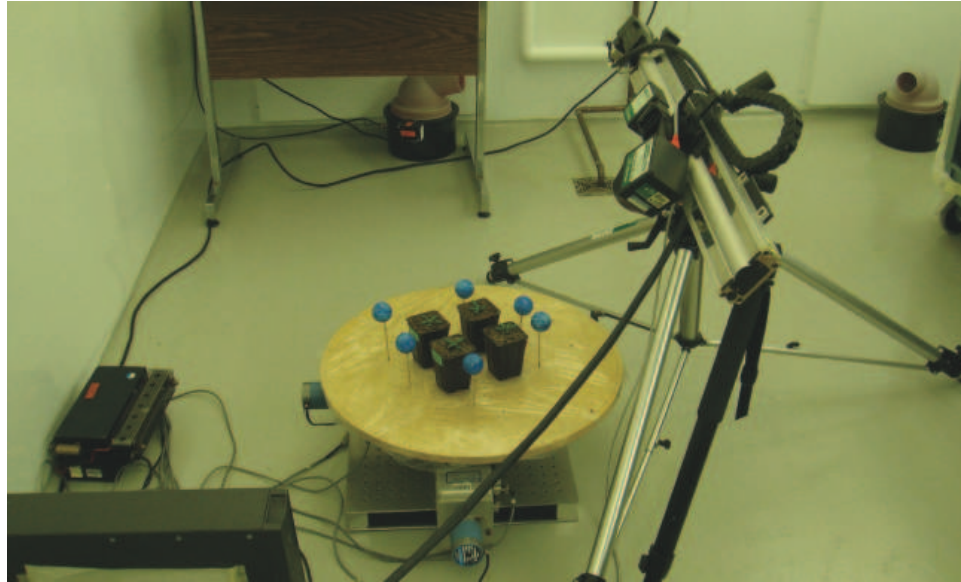


Figure 3.1: The experimental setup used by Yang in the Transgenic lab no. 3 at the Biotron Experimental Climate Change Research Center, the University of Western Ontario [16]

subsequent growth measurements.

- Second, it takes hours (more than 4) to process a single dataset.

We introduce several pre-processing techniques to overcome the problems listed above so as to replace human interaction with automatic registration. We do this by detecting semi-spheres in the range images and replacing these semi-sphere with “perfect” synthetic sphere data. Also, macros in Geomagic Studio 12 are used to replace the selection-based actions (e.g., mouse “clicks”) to select appropriate buttons to perform the registration process.

Before describing the proposed methodology, two different kinds of file formats are described here that are used during the implementation phase. This will allow the readers to more readily understand the proposed methodology and the reason of using two formats here. Table 3.1 describes the format of the 3PI files. 3PI is the native file format for the ShapeGrabber scanner. One of the advantages of 3PI is data is stored in ASCII and can be changed at will by a user. However, once a 3PI file is opened and modified by Geomagic Studio, it cannot be re-saved as a 3PI file but rather as a WRP file, where WRP is Geomagic’s native file format and is unfortunately proprietary. As a result, once a file is saved in the WRP format, it can only be further manipulated by Geomagic Studio (but it cannot be modified using user-defined functions without Geomagic). Therefore, we use a file format that

is both known and alterable using both user-defined functions and Geomagic. The ASCII representation of the STL (Standard Tessellation Language) is used to achieve the aforementioned goals and Table 3.2 gives a general overview of the STL file format. Thus, 3PI files are converted to STL files that are used in all further pre-processing. Once all kind of pre-processing is done on STL files, we convert them in WRP format to speedup Geomagic’s actions.

Topic	Description
Organization of Data	<ul style="list-style-type: none"> - During scanning, data is acquired profile by profile (i.e., a profile is the data collected from the processing) of 1 full laser line). - In a profile, points are in ascending order along the X-axis.
Co-ordinate System	No specific co-ordinate system is defined for this file format.
Comments	<ul style="list-style-type: none"> - Any line starting with a pound (#) sign is a comment. - Structured comments, provide additional information, start with a colon sign (:) followed by the pound (#) sign. - For example: <ul style="list-style-type: none"> - #:Number of Points per Profiles: <integer> indicates the maximum number of points in a profile. - #:Number of Profiles: <integer> indicates the maximum number of profile in the file. - #:Profile: <integer> indicates a particular profile. - #:Pose Transformation: describes the standard rigid transformation applied to the scan data.
Data Points	<ul style="list-style-type: none"> - Each valid data point is represented by one line in the file. - Each line consists of the coordinates of the point, the intensity value and the order of the point in the profile. - Co-ordinates of a point are floating point values, the range for the intensity value and the order of the point is 1200-14000 and 0-1280, respectively.

Table 3.1: 3PI file format (ShapeGrabber laser scanner’s native format)

The methodology followed in this thesis is as follows:

1. For each semi-sphere in the 1st view of the 1st dataset:
 - i. **Segment the Semi-spheres (still a manual process):** Each semi-sphere is manually segmented using Geomagic Studio 12. For each visible semi-sphere in the original 3PI file, an individual STL file is generated containing the semi-sphere data for that particular view. Since there are

Topic	Description
Starting String	solid (lower case)
Body	facet normal n_1 n_2 n_3 outer loop vertex $v1_x$ $v1_y$ $v1_z$ vertex $v2_x$ $v2_y$ $v2_z$ vertex $v3_x$ $v3_y$ $v3_z$ endloop endfacet (Here, the values of n or v are floating point number in sign-mantissa 'e'-sign-exponent format.)
Ending String	endsolid (lower case)

Table 3.2: STL file format

most 6 visible semi-spheres there are at most 6 STL files. It may be noteworthy that both the 3PI and the STL files contain the same semi-sphere data but have different formats.

- ii. **Estimate the Parameters (Using LS Method):** Initially, the radius and the center coordinates are estimated from the STL files containing the semi-sphere data using a LS sphere estimation method. As the semi-sphere data inside the STL files are manually segmented, the probability of having outliers (in this particular place, “outliers” refers affiliated parts of semi-sphere data, like the stands and overlapping leaves, not the “noisy data” produced by the scanner) is relatively low. So, LS should return a reasonable solution here. This, as well as the simplicity of the implementation and the computation are the major reasons for using the LS method at this stage. However, these initial estimated values play a vital role as they serve as the initial guess for the robust estimation stage.

2. Step 1 is repeated for all the views of the 1st dataset.

3. For each view of the 1st to 75th datasets:

- i. **Segment the Semi-spheres (Automatic Segmentation):** Each semi-sphere is automatically segmented from the 3PI files using the estimated radius and the center coordinate obtained from step 1 and 2. This automatic step relies on the assumption that the reference spheres and the range sensor have not being moved and that each view is generated by the same rotational increment of (30°) as before. Likewise, a maximum of 6 individual STL files are generated containing semi-sphere data for each view.

- ii. **Estimate the Parameters (Using Robust Estimation):** Now, with robust estimation, the sphere center coordinates and radius are estimated using the estimated values from LS method as the initial guess. As affiliated parts of semi-sphere data may be introduced due to automatic segmentation, refinement of parameters is done using robust estimation techniques in this stage.
 - iii. **Segment the Plant Data:** Another STL file, containing only the plant data, is generated from the original 3PI files by deleting the semi-spheres using the estimated values of their center coordinates and radius from step 3(ii).
 - iv. **Replace the Semi-Sphere with Full Sphere Data:** “Perfect” full sphere data are generated using the estimated parameter values from step 3(ii) and parametric equation of spheres. Then, the semi-sphere data are replaced with “perfect” full sphere data and saved as STL files for further manipulation.
 - v. **Reconstruction of Each View’s Data :** There are now 7 STL files generated from step 3[iii] and step 3[iv], 6 STL files containing full sphere data (the actual number may vary depending on the number of visible semi-sphere in the original 3PI files) and 1 STL file containing the plant data. These files are then combined using Geomagic Studio 12 to reconstruct each original view. At this point, the reconstructed view contains full sphere data in the place of the incomplete semi-sphere data.
4. **Process of Registration:** Each 12 reconstructed views of each dataset are then registered using Geomagic Studio 12 to generate the synthesized 3D polygon mesh.
5. **Measuring Plant Growth:** Using the 3D polygon meshes generated from Step 4, we compute the area and the volume of the plants to estimate the plants’ growth cycle over the time.

Note that according to the proposed methodology, the manual detection of semi-spheres from the original raw images is done only once. But in practice, we performed this manual detection more than once as Yang seems to have moved the position of the reference spheres as well as the scanner a number of times during the scanning process (however, this did not affect her results). Table 3.3 shows the ranges of datasets where the position of all the 6 reference spheres remained static. Each dataset at the beginning of these range intervals had to be manually segmented.

Figure 3.2 shows a flow chart for the automation process described above.

Position Number	Range of Datasets
Position: 01	00-08
Position: 02	09-11
Position: 03	12-51
Position: 04	54-55
Position: 05	56-62
Position: 06	63-68
Position: 07	69-71
Position: 08	72-78
Position: 09	79-80
Position: 10	81-83

Table 3.3: List of the ranges indicating up to which datasets the position of the reference spheres was unchanged. Note that datasets 52 and 53 and parts of dataset 51 are missing.

3.1 Implementation of Automatic Registration Process

The automation of the registration process comprises of four major stages:

1. Process of segmentation and estimation
2. Replacement of semi-sphere with full sphere data
3. Reconstruction of views
4. Process of registration

The sections following gives the details about the implementation. Figure 3.3 shows the detail of the stages related to the automation of the aforementioned registration process.

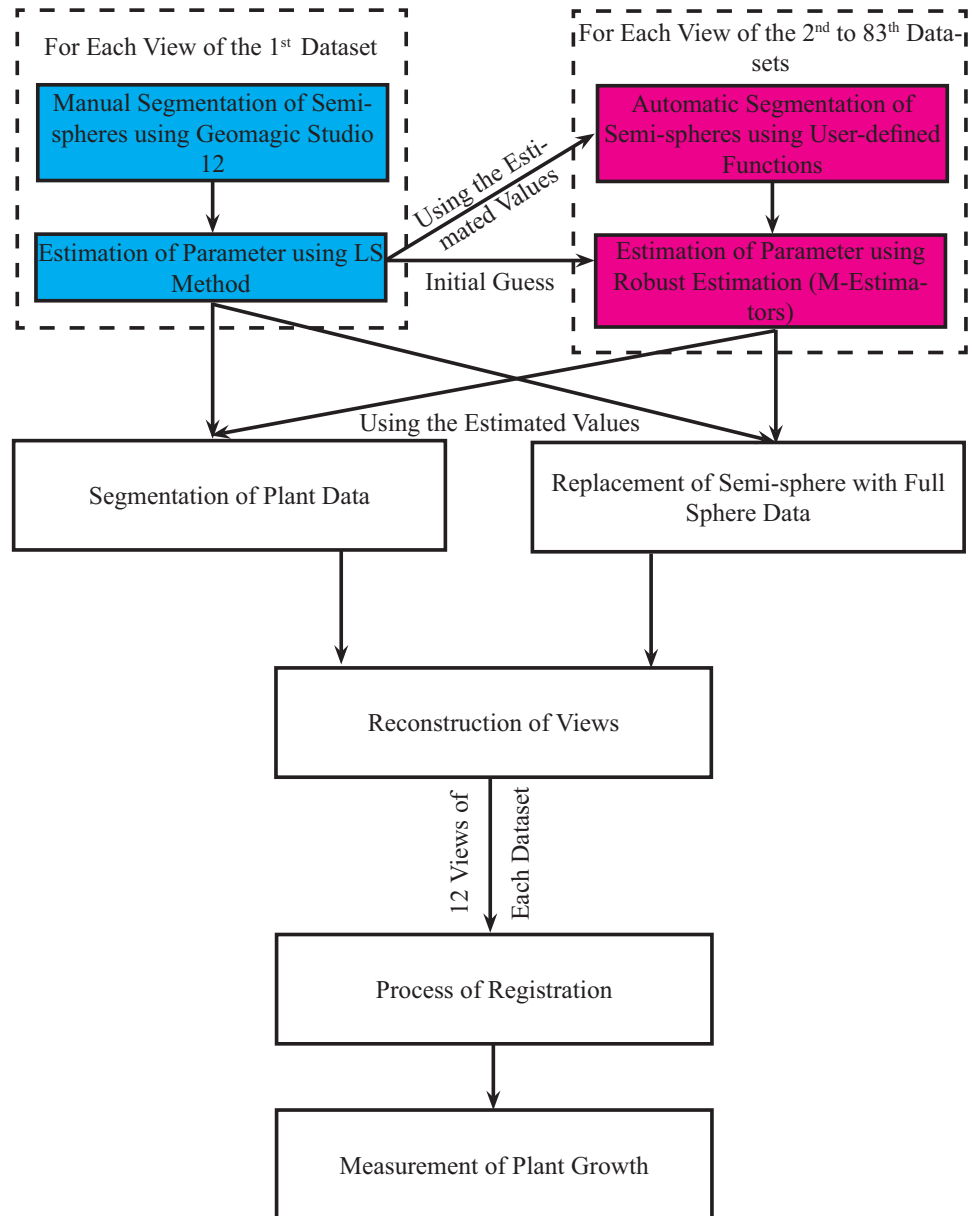


Figure 3.2: Steps related to the proposed methodology

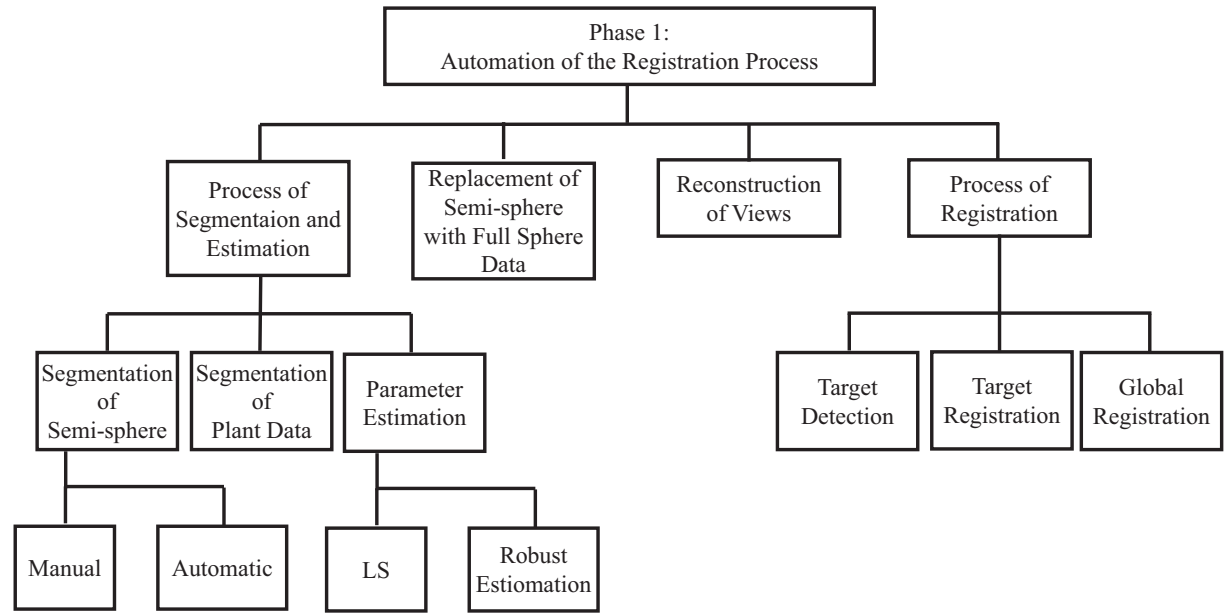


Figure 3.3: Stages related to the automation of the registration process

3.1.1 The Process of Segmentation and Estimation

During the segmentation phase, the location of all 6 reference spheres is estimated from each view either manually or automatically. For both manual and automatic segmentation, Geomagic Studio 12 and user-defined functions are used, respectively. The main goal of this step is to separate each semi-sphere from the original 3PI file and then save the remaining files in STL file format, so that the incomplete semi-spheres can be replaced by full sphere data, facilitating further manipulation. These segmented semi-spheres data are used to estimate the center coordinates and radius. Initially, the LS method is used to estimate these parameters and then fine tuning is done using robust iterative M-estimation with the help of the previously mentioned values as the initial guess. After the parameter estimation phase, these estimated values serve the purpose to generate plant only files by removing the semi-spheres data as well as to replace the semi-sphere data with “perfect” full sphere data. 7 STL files in total, 6 semi-sphere files and 1 plant only file (semi-spheres removed), are generated for each view at this phase. Note that the number of semi-sphere files may vary (≤ 6) depending on the visibility of reference spheres in the original 3PI file. These newly generated files are used in the reconstruction phase.

3.1.1.1 Segmentation of Semi-Spheres

This stage is accomplished in two different ways:

1. **Manual Segmentation of Semi-Spheres:** Manual segmentation of semi-spheres is performed using Geomagic Studio 12. Theoretically, this stage is needed only for the 1st dataset. But in practice, this is performed for all the first of datasets where the reference spheres are in constant locations, among the 75 datasets, as Yang changed the spheres’ position during the scanning process. For further explanation, we just consider the 1st dataset. Each of the 12 views (12 3PI files) of the 1st dataset is opened in the “Model Manager” of Geomagic and semi-spheres are segmented manually one by one using “Selection” tool. While saving these semi-spheres files, the STL file format is used instead of the 3PI format. We use the STL format here as Geomagic Studio does not allow any altered files to be saved in 3PI format, which is native to ShapeGrabber laser scanner. We can alter 3PI files using any editor, of course.

Moreover, Geomagic’s native format, WRP, is a propriety format and not accessible to us. Once any file is saved in the WRP format it can not be manipulated afterward (except by Geomagic, of course). Moreover, the STL format is a well known file formate can be saved in either ASCII and binary. We use the STL format is here for both readability and ease of further processing.

2. **Automatic Segmentation of Semi-Spheres:** Automatic segmentation is performed on each view of datasets 2-75 (the first view of various subranges

of the datasets, where the reference spheres are moved, was first manually segmented). Automatic segmentation is accomplished using user-defined function, **Segment_Semi_Sphere** (). To segment the 3D points related to semi-spheres the estimated parameter values from the estimation phase (Section 3.1.1.2) are used. Although this step is explained here, in practice, it comes after the manual segmentation and the estimation of the initial center coordinates and radius of the semi-spheres of the 1st datasets were the reference spheres are moved. Because the position of the reference spheres is assumed to be static during the whole scanning process (but Yang [16] moved them to improve the spheres' visibility) and so, the position of any semi-sphere in any dataset can be located once the center coordinates and radius of the semi-spheres of the 1st dataset where reference spheres are moved are computed.

Let us assume that the estimated center coordinates of the m^{th} semi-sphere, $m = 1, 2, \dots, 6$, of the n^{th} view, $n = 1, 2, \dots, 12$, of the 1st dataset are $(xc_{m,n,1}, yc_{m,n,1}, zc_{m,n,1})$ and the radius is $r_{m,n,1}$. Then, for all 3D points, (x_i, y_i, z_i) , where

$$\sqrt{(x_i - xc_{m,n,1})^2 + (y_i - yc_{m,n,1})^2 + (z_i - zc_{m,n,1})^2} \leq (r_{m,n,1} + \varepsilon), \quad (3.1)$$

belong to the m^{th} semi-sphere of the n^{th} view of the rest of the datasets (in dataset ranges where the reference spheres have not been moved). In Eq. 3.1, $\varepsilon = 0.5$. is a term used to slightly increase the estimated radius value (so that all sphere points are definitely included in Eq 3.2).

3.1.1.2 Estimation of Parameters (Center Coordinates and Radius of Semi-Spheres)

To estimate the center coordinates and radius, two different approaches are used in this thesis.

1. **Estimation of Parameters using LS Method:** To estimate the center coordinates and the radius of the semi-spheres for data obtained using manual segmentation, LS method is used. The main reasons for selecting this method include ease of designing an efficient error function, simplicity of the method itself and ease in implementation and computation. Moreover, due to manual segmentation, the possibility of having affiliated sphere elements is relatively low.

A user-defined MATLAB function, **LS_Sphere_Fit** (), is used to estimate the parameters using the ordinary LS method. This function is a modification of the solution of a sphere fitting problem provided by Ken Garrard, one of the members of MATLAB Central [51]. This function takes the 3D point cloud of

sphere as input and returns the estimated center coordinates and radius along with the individual residual as well as the average residual. Eq. 3.2 is used in the implementation because the equation expresses the parameters, a , b , c , and, d , in a linear manner:

$$x^2 + y^2 + z^2 + ax + by + cz + d = 0. \quad (3.2)$$

By solving the system of equations, the estimated values of the center coordinates, (x_c, y_c, z_c) , and the radius, r , of the sphere are determined from a , b , c , and, d using Eq. 3.3 and Eq. (3.4), respectively:

$$(x_c, y_c, z_c) \equiv \left(-\frac{a}{2}, -\frac{b}{2}, -\frac{c}{2}\right) \quad (3.3)$$

and

$$r = \sqrt{\frac{a^2 + b^2 + c^2}{4} - d}. \quad (3.4)$$

Note that these estimated values are used as the initial guess for the robust estimation of spheres. The values obtained from this stage are very important as the convergence of the robust estimation depends on a good initial guess as it is an iterative calculation.

2. **Estimation of Parameters using Robust Estimation:** Because the automatically segmented semi-spheres in later datasets may be introduced with extremely outside data (e.g., the stands used for the reference spheres and part of plant foliage close to the spheres), further refinement is done using a robust technique, namely M-Estimation. Moreover, data can be corrupted with noise during scanning process. The estimated values of center coordinates and radius for the 1st dataset serve as the initial guess for this stage. One of the main reason (other than the noises introduced during the scanning process) of using M-Estimation is to protect the estimated parameter values from outliers introduced due to automatic segmentation. Because if a little non-sphere data close to the sphere is included it can affect the merging stage with wrong position of target spheres.

When implementing M-Estimation, we examined both the Huber and the Bisquare estimators, to draw comparisons between their performances and their accuracy. Important factors related to the implementation of M-Estimators are *MaxIter*, the maximum number of iterations allowed for the estimation, *TolFun*, the termination tolerance (difference in adjacent residual sum of squares calculations), and *TolX*, the termination tolerance on the estimated coefficients. During our experiments, we use MATLAB'S built-in function “*nlinfit*” to implement the Huber and the Bisquare estimators. The values of the aforementioned parameters are set to the default values¹.

¹The default values of *MaxIter*, *TolFun*, and *TolX* is 100, 1e-8, and 1e-8, respectively, in MATLAB.

3.1.1.3 Segmentation of Plant Data

After estimating the center coordinates and the radius for each semi-sphere for all the datasets, these values are used to delete the semi-spheres data from the original 3PI files, generating a file that contains only the plant data.

If the estimated center coordinates and the radius of one of the semi-spheres in a particular view is (x_c, y_c, z_c) and r , respectively, then we delete all the (x_i, y_i, z_i) satisfying:

$$\sqrt{(x_i - x_c)^2 + (y_i - y_c)^2 + (z_i - z_c)^2} \leq (r + \varepsilon) \quad (3.5)$$

from the 3PI files. Eq. 3.5 is satisfied only for those points lying on or within the surface of a particular sphere with radius r . However, an additional parameter, ε , is used with the radius to ensure the successful removal of all semi-sphere data from the file. If a little non-sphere data close to the sphere is also removed its effect on the merging stage will be negligible. Figure 3.4(a) shows the original image of the 2nd view of the 12th dataset and Figure 3.4(b) shows the same image after removing the semi-spheres data.

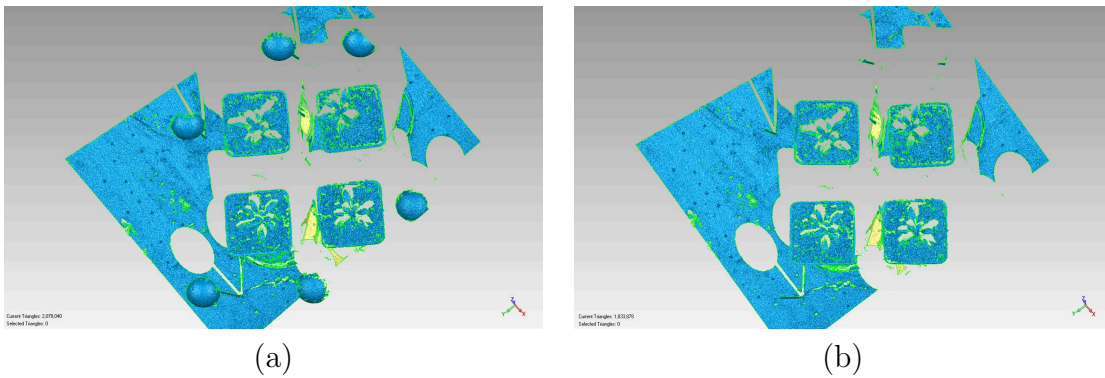


Figure 3.4: Segmentation of plant data; (a) the original raw 3PI image of the 2nd view of the 12th dataset, (b) the same view after removal of the semi-sphere data from the original image

3.1.2 Replacement of Semi-sphere with Full Sphere Data

In this phase, the incomplete semi-sphere data are replaced with full sphere data to aid the automation of the overall registration process. Initially, the 3D coordinates of a full sphere are generated using the estimated center coordinates and radius values from the estimation phase (Section 3.1.1.1). After that the newly generated sphere “perfect” data are saved as individual STL files in ASCII mode.

To generate the 3D coordinates in MATLAB, the parametric equations of sphere were used. The estimated center coordinates and radius values are used in these equations so that the location of the newly generated full spheres are exactly the same as the semi-spheres in the original 3PI files during the scanning process. The parametric equations of a sphere are:

$$\begin{aligned} x &= x_c + r \cos \theta \sin \varphi \\ y &= y_c + r \sin \theta \sin \varphi \\ z &= z_c + r \cos \varphi. \end{aligned} \tag{3.6}$$

In this equation, θ is the azimuthal angle that varies from 0 to 2π while φ is the polar angle that varies from 0 to π . Moreover, in these equations, r is the radius, and (x_c, y_c, z_c) is the center coordinates of the sphere. During implementation, 250000 points are generated using the parametric equations of sphere with an angle increments of 0.0126 for $\Delta\theta$ and 0.0063 for $\Delta\varphi$. Once the 3D full sphere points have been generated, the coordinates were saved in a STL file. STL files, which represent the surface geometry of three 3D objects as facets, independent of attributes like color or texture, can be represented in both ASCII and binary mode. Although binary files are more compact, the ASCII format of STL files has been used here for both readability and ease of modification/ manipulation. To store the 3D points in a STL file, the standard format of an ASCII STL file is maintained so that Geomagic Studio can read it. As mentioned in Table 3.2, surface normal for a triangle needs to be informed in the STL file. To calculate the surface normal, N , Eq. 3.7 has been used. The equation takes the vector cross product (\times) of two edges of a triangle to calculate the surface normal. For a triangle having three 3D points, p_1 , p_2 and p_3 , the vectors $U = p_2 - p_1$ and $V = p_3 - p_1$ can be computed and then the unnormalized surface normal can be computed as $N = U \times V$. Surface normals can be used by Geomagic to shade the surfaces. To achieve the goal, a modified version of Bill McDonald's, one of the contributors of MATLAB Central, *surf2stl ()* [52] function is used.

$$\begin{aligned} N_x &= U_y V_z - U_z V_y \\ N_y &= U_z V_x - U_x V_z \\ N_z &= U_x V_y - U_y V_x \end{aligned} \tag{3.7}$$

Once the full sphere STL files have been generated, these STL files along with the plant only STL file from the segmentation phase (section 3.1.1.3) are fed into the next phase to reconstruct the original views with complete reference spheres. Figure 3.5(a) shows one of the segmented semi-spheres of the 1st view of the 1st dataset with the semi-spheres and Figure 3.5(b) shows the full sphere after the replacement of the semi-sphere data.

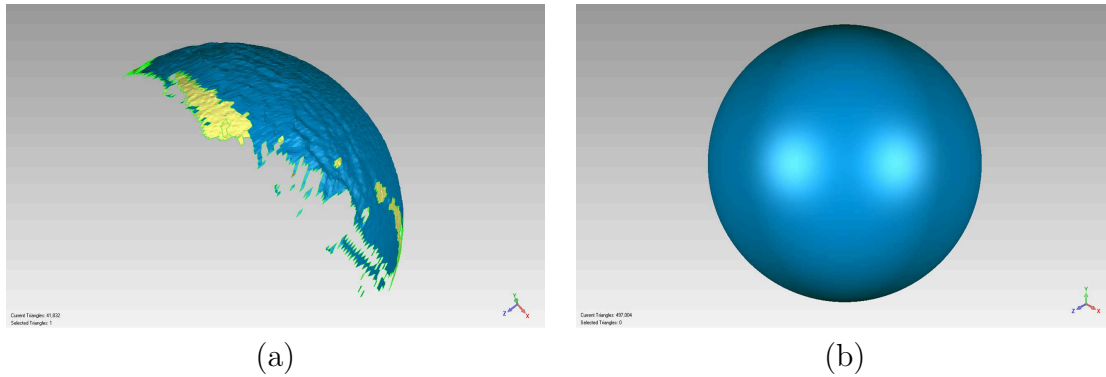


Figure 3.5: Replacement of the semi-spheres with the full sphere data; (a) segmented semi-spheres from the 1st view of the 1st dataset, (b) the same image after replacing the incomplete semi-sphere data with the full sphere data using the estimated center coordinates and radius values

3.1.3 Reconstruction of Views

In the reconstruction phase, every view of the each datasets is regenerated with full sphere data. In the original 3PI files, the reference spheres are incomplete as they appear as noisy, holey semi-spheres rather than full spheres. To merge the 12 views in each dataset into a single polygonal mesh, the full sphere files from Section 3.1.2 and the plant only files from Section 3.1.1.3 are combined together using Geomagic’s tool “Combine” (Polygons → Combine → Combine). This command creates a single polygonal object combining multiple user selected (active) polygon objects. To remove the need human interaction, this command is recorded as a macro using VBScript (Combine.vbs). This phase returns the original views of each dataset with the full spheres in the place of incomplete semi-spheres. The list of macros (written in VBScript), used in this thesis, is given in Table 3.4.

Figure 3.6a shows the original raw image of the 1st view of the 30th dataset and Figure 3.6b shows the reconstructed view with full sphere data.

3.1.4 Process of Registration

Registration is a process of re-orientating two or more objects, point or polygon, that comprises a single scene. This is a useful process to make a more complete scene by coinciding the identical regions of different objects so that important information can be retrieved from that scene using further analysis.

All the previous pre-processing are done only to automate this time consuming and laborious phase. In the registration phase, the reconstructed views with full

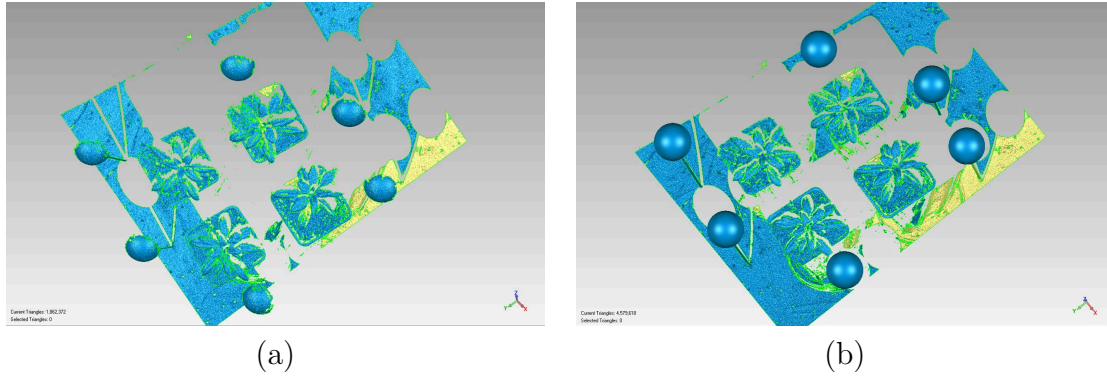


Figure 3.6: Reconstruction of views; (a) the original raw 3PI image of the 1st view of the 30th dataset, (b) the same view with full sphere data after the reconstruction process

sphere data (section 3.1.2) are used to generate the 3D models of *Arabidopsis thaliana* showing the different stages of its growth cycle. To create 3D synthesized polygon meshes from the reconstructed images, 12 different views of each dataset is merged together to create a complete 3D model of that particular growth stage. Afterwards, the growth pattern (specially, area and volume) of the *Arabidopsis thaliana* can be measured from these 75 composite 3D images.

This phase is composed of processes accomplished using several tools of Geomagic Studio 12. These commands are recorded as macros to reduce human interaction during the whole process of registration. Steps related to this phase are as below:

1. For each view of the 1st dataset:
 - i. **Detect Sphere Targets (Alignment → Scan Registration → Detect Sphere Targets)**: This Geomagic command detects the center coordinates of reference spheres and generates point features to aid during “Target Registration” step. The result of this step is a point feature label, named as Target 1, 2, ..., N , in the “Features” folder. Geomagic automatically generates these labels to uniquely identify each reference spheres and the feature folder is Geomagic’s self-created folder where it keeps all these labeled features for further use during “Target Registration”. The spheres must be labeled as feature points so Geomagic knows which spheres correspond to which sphere over time (Yang [16] did this manually). This is the one of the steps for which replacement of semi-sphere data with full sphere data is done to facilitate automation. However, “Detect Sphere Targets” is basically manual operation but in well controlled environments it can be automated. This tool is sensitive to

a great deal of factors relating to curvature in the model. Moreover, for incredibly dense target model, this operation will fail as Geomagic’s current algorithm is unable to work with extremely dense model. Again, the targets need to be complete and properly sampled to make this tool work. As this is a very sensitive action, sometimes unexpected results may occur. As in first place, our sphere data was so dense that Geomagic’s “Detect Sphere Targets” failed to detect target spheres properly. We reported this bug² regarding the “Detect Sphere Targets” tool when the amount of data for targets is large.

However, this problem can be resolved with or without using Geomagic. To overcome this problem without using Geomagic is to make sure that while creating the full spheres, number of 3D points are generated in such a way so that this tool can properly identify the targets. Otherwise, two other Geomagic’s commands can be used to modify the large data so that “Detect Sphere Targets” and “Target Registration” can be applied properly³.

- **Convert to Points** (Polygons → Convert → Covert to Points): This tool is used to convert a polygonal object to a point object so that the large data can be re-sampled.
- **Sample** (Points → Sample → Uniform): This tool is used to reduce the number of points on flat surfaces uniformly. In the case of curved surfaces as spheres have, the command reduces the number of points to a specified density. It only works on Unordered Point objects. In practice, *0.5mm* is specified as the degree of point-reduction so that points are thinned to have this distance between any two points.

However, down sampling of data may directly affect the performance of the registration process. So, it is advisable to create the full spheres in such a way so that “Detect Sphere Targets” works perfectly.

- ii. **Target Registration** (Alignment → Scan Registration → Target Registration): This is the main registration process that registers or merges two or more point or polygon objects based on targets found by Detect Sphere Targets. At least three targets must have been found on each object to perform “Target Registration”. So, in order to perform registration properly, at least three of the six reference spheres from each view must be visible and detected properly during the “Detect Sphere Targets” step. During

²We sent a mail to Geomagic Support Center (support.geomagic.com) mentioning that “Detect Sphere Targets” tool does not work properly for our data and the “Target Registration” phase is sometimes skipped while running macros. Their technical team, especially, the macro team, replied us mentioning that they found a bug with these two tools when the amount of data is large for target objects. Their existing algorithm is unable to handle dense target data.

³These steps are suggested by the technical team of Geomagic to overcome the problems with macro to some extent.

this step, 12 views of a single dataset are merged together to generate a single 3D mesh of that scene. It is noteworthy that similar to “Detect Sphere Targets”, “Target Registration” is also preferable as manual operation as this is extremely sensitive to environmental factors like the curvature in the model.

- iii. **Target Cleanup** (Alignment → Scan Registration → Target Cleanup): Once the registration is done, the target spheres are removed using “Targets Cleanup” tool. This Geomagic command removes spherical or circular sticker registration targets from an object.
- iv. **Global Registration** (Alignment → Scan Registration → Global Registration): One of the major difficulties in measuring plant growth is that the point cloud data provided by the scanner is often not dense enough. Moreover, due to growth chamber ventilation that we could not control, sudden movements of plant leaves or stem may be captured in the range images during the scanning process. These sudden movements may affect the registration process resulting poor performance. To attenuate such undesirable errors, refinement of the previous registration needs to be done. This is accomplished by the Global Registration step, which refines two or more roughly registered point or polygon objects. This step also includes “Overlap Reduction”, a part of the “Global Registration” tool, performed after “Global Registration” is done. This option slightly bends the objects to accomplish a more perfect registration.

2. Apply step 1 on each view of the rest of the 74 datasets.

All these actions are automated using Geomagic’s macros. After the registration phase, 75 triangular meshes (composite scenes) are generated showing *Arabidopsis thaliana* at the different stages of its growth. These 3D images are then used in the growth measurement phase. Figure 3.7 shows the overall registration process where the icons are the corresponding symbols of these tools in Geomagic. Table 3.4⁴ lists all the macros of Geomagic and their equivalent code written in VBScript.

Figure 3.8(a) shows the synthesized 3D polygonal mesh after performing “Target Registration” using the reference spheres and Figure 3.8b shows the final polygonal mesh after removing the targets and performing “Global Registration”. These images are generated using the 30th dataset.

⁴This table gives a basic introduction to the macros used here. Further information regarding the arguments and the detail implementation can be found in the appendix G.

Name of the Tool	Equivalent VBScript Code
Open a file	geo.open
Save as	geo.saveas
Combine	geo.combine_objects
Select All Objects in the Display Manager	geo.select_all_objects
Merge	geo.merge_objects
Detect Sphere Targets	geo.detect_sphere_targets
Convert to Points	geo.modify_current_points
Sample	geo.sample
Target Registration	geo.target_registration
Target Cleanup	geo.target_cleanup
Global Registration	geo.global_registration
Obtain the Surface Area	geo.query

Table 3.4: List of the Geomagic’s macros and their equivalent VBScript code used to automate the registration process

3.1.5 Measuring the Growth Cycle of *Arabidopsis thaliana* Plants

In this section we describe the steps necessary to measure the growth of *Arabidopsis* plants over their life cycle. It may be noteworthy that measuring plant growth is not our main goal. Rather than we focus on the automation of the registration process that is needed to create the 3D polygonal meshes from which plant growth can be measured. Additionally, this part is still done manually as the provided Geomagic’s tools to measure plant growth are not recordable, yet.

3.1.5.1 Manual Editing (Pre-processing)

To measure growth from the 3D triangular meshes, obtained from the registration process (section 3.1.4), manual editing using Geomagic is required to remove the extraneous elements (e.g., the post, the background table and the soil). The manual nature of this editing may directly affects the accuracy of the measurement. Similar approaches are used here as Yang used in her thesis [16].

1. Using “Boundary From Spline” (**Polygons** → **Boundaries** → **Create** → **Boundary From Spline**) tool, a boundary line is defined between the leaves and the soil.
2. Step 1 is applied to the lower part of the leaves if there is any further soil attached to the leaves.

3. Using “Bounded” (**Select** → **Data** → **Select Components stack** → **Bounded**) tool (i.e., right-click at one of selected triangles in the “Graphic Area”), area selected using step 1 and step 2 is bounded and removed.

After performing the aforementioned steps, the shape of the leaves may not be still perfect due to additional overlapping triangles around their edges. Therefore, to refine the shape of the leaves by smoothing the edges, “Relax Boundary” (**Polygons** → **Boundaries** → **Modify stack** → **Relax Boundary**) tool is used. The level of the smoothness can be controlled using the **Iterations** field. The higher the number for **Iterations**, the smoother the boundary line will become. For leaves, having partial extraneous polygons around their edges, **Partial Boundary** is preferred instead of **Entire Boundary** option. Figure 3.9a shows the extraneous elements in the synthesized 3D polygon meshes (in red) and Figure 3.9b shows the extra triangles around the leaves without a defined boundary. After all these manual pre-processing, the edited synthesized 3D triangular meshes are used to measure the plant growth, especially the surface area and the 3D volume.

3.1.5.2 Measuring Plant Growth using the 3D Triangular Meshes

The surface area and the 3D volume of a plant increases naturally, as it grows. Therefore, we calculated the plant canopy area and volume as measurements of the growth of Arabidopsis plants using its 3D synthesized triangular meshes.

A triangular mesh is a type of polygonal mesh that defines the shape of a polyhedral object in 3D computer graphics and solid modeling [53]. As a triangular mesh is the combination of meshes representing a particular object, surface area of the overall mesh can be computed by summing the areas of each triangle. One of the 3D triangles on the mesh having vertices P_1 , P_2 and P_3 , and the 2 vectors lying on it are $A = P_2 - P_1$ and $B = P_3 - P_1$. And the area of the triangle is $\frac{1}{2}||A \times B||_2$. This way, the overall surface area of 3D triangular mesh is determined by summing up the area of each triangle on the mesh [54].

Moreover, the volume of a triangular mesh can be calculated in Geomagic and the algorithm is as follows [15]: Assume that we have a triangulated surface embedded in R^3 and $z = (0, 0, 0)$ be an additional point in space. For each triangle on the surface with vertices a, b, c , a tetrahedron a, b, c, z can be imagined. Then the volume of the tetrahedron is computed with a sign (positive if z sees a, b, c making a left turn and negative if otherwise). The overall volume of the body is computed by adding all the signed volumes.

Using Geomagic’s embedded functions “Compute Area”, canopy surface area is computed based on the 3D triangular mesh. For the plant canopies, the entire surface area or specific area is obtained by selecting the proper region.

Tools → Analysis → Compute stack → Compute Area

In order to measure volume, the macro needs a watertight polygon mesh. The object can not have any holes or gaps. It can have multiple volumes, but they all need to be closed. Moreover, when measuring volume, direction of the normal of all the triangles have to be in the same direction, “facing up” or “facing away”. “Compute Volume to Plane” is used to measure plant volume as plant body is not closed. This tool uses a plane to project the surface area, too. If the plane is a best fit plane through the center of the data, then the volume is measured in both positive and negative space. Both absolute values have to be added to get the volume. But because the leaves are convex/ concave (and so, we have 3D area), this measurement will not be accurate or consistent over the length of the experiment. That is why a plane is created that is below the data (on the yellow side at a known stable juxtaposition from the foliage) like the table top. Moreover, the position of the plane is very important to measure volume as the further away the plane the large the volume will be. So, to maintain consistency the plane should be always at a fixed distance from the plants. Before calculating the volume, we use the following steps:

1. Use the table, used during the scanning process, as our reference plane to provide consistency during measuring volume to plane.
2. Create a best fitting plane to the reference table using “Best Fit” (**Features** → **Create** → **Plane stack** → **Best Fit**) tool.
3. Create an offset plane at a specific distance from the best fit plane using “Plane Offset”⁵ (**Features** → **Create** → **Plane stack** → **Plane Offset**) tool. The distance between the best fit and offset plant should be always same to provide consistency.
4. Align the offset plane to the XY “World Plane” using “Align To World” (**Alignment** → **Object Alignment** → **Align To World** → **Best Fit**) tool.
5. Compute volume using “Compute Volume To Plane” (**Tools** → **Analysis** → **Compute stack** → **Compute Volume To Plane**) tool.

These steps enable the Geomagic to perform a volume measurement of an open object. This overall procedure is explained in Figures 3.10a, 3.10b, 3.10c, 3.10d, and 3.10f.

⁵For experimental purpose, we set the offset plane just below the foliage. But this creates another problem as it seems somehow the distance between the table and the pots also changed during the scanning process. So, we pick a common distance of -65mm (- indicates above) to place our offset plane. But this will not provide proper result as the distance between the plants and the plane is 1-2mm at some points and again 60-70mm at some points. But setting the offset just below the foliage will also create the similar problem as the distance changed during scanning process.

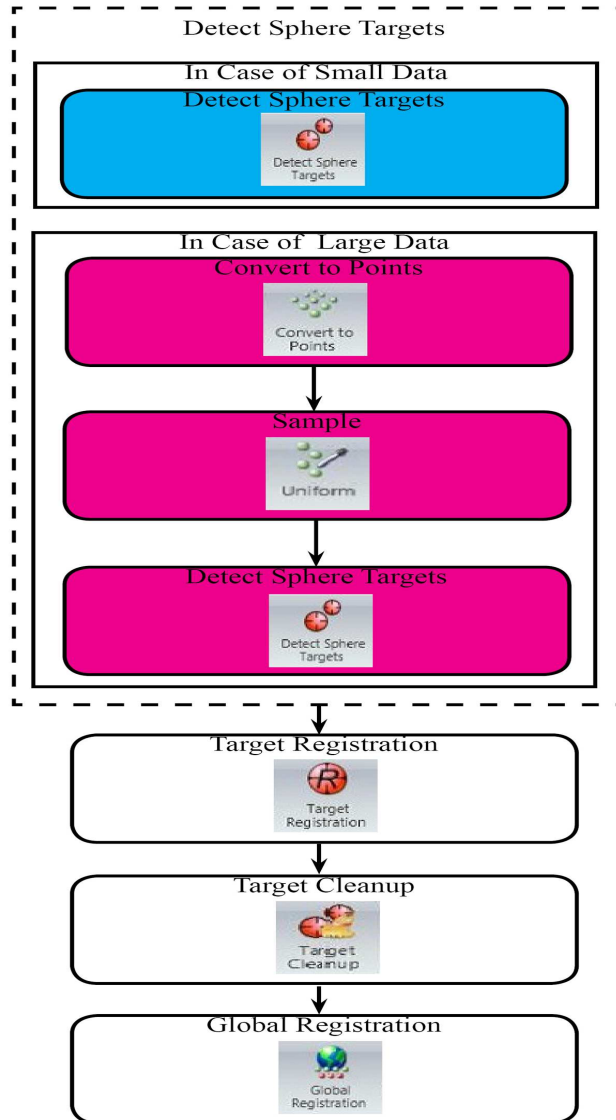


Figure 3.7: Steps related to the overall registration process

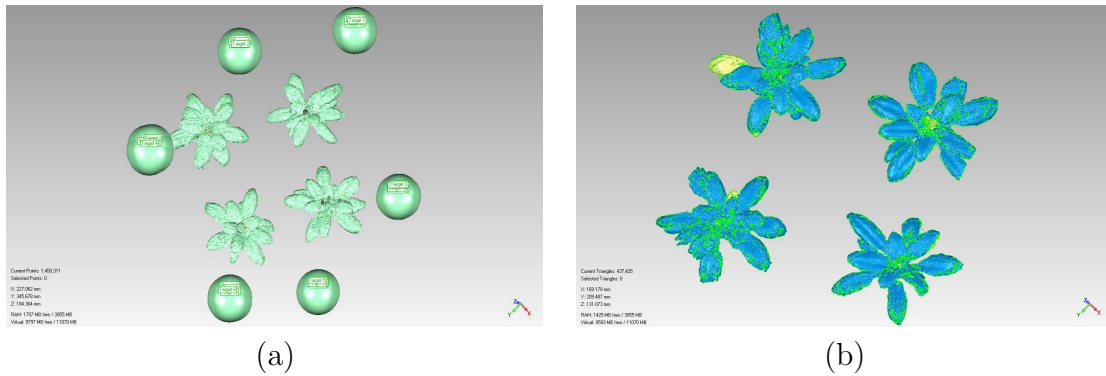


Figure 3.8: (a) The synthesized 3D polygonal mesh after performing "Target Registration" using the reference spheres, (b) the final polygonal mesh after removing the targets and performing "Global Registration"

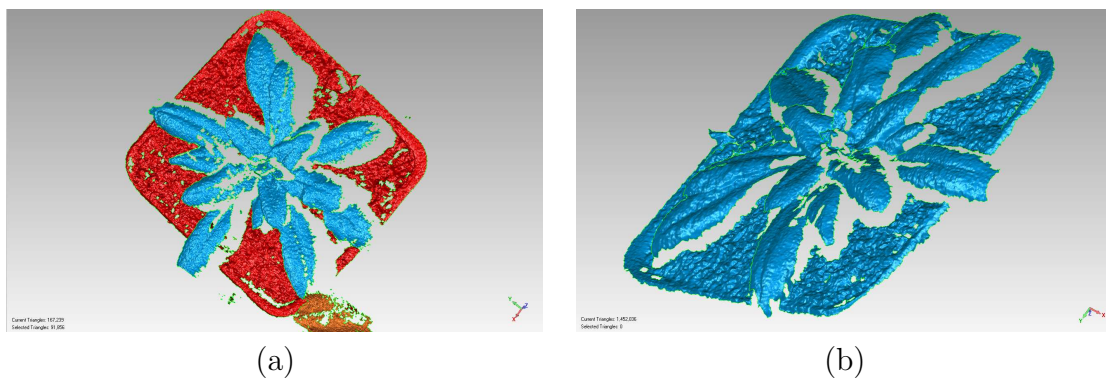


Figure 3.9: Pictorial illustration of problems with the manual editing before measuring plant growth; (a) The extraneous elements (e.g., the soil) in the synthesized 3D triangular mesh (in red) and (b) the extraneous triangles around the leaves without a regular or defined boundary.

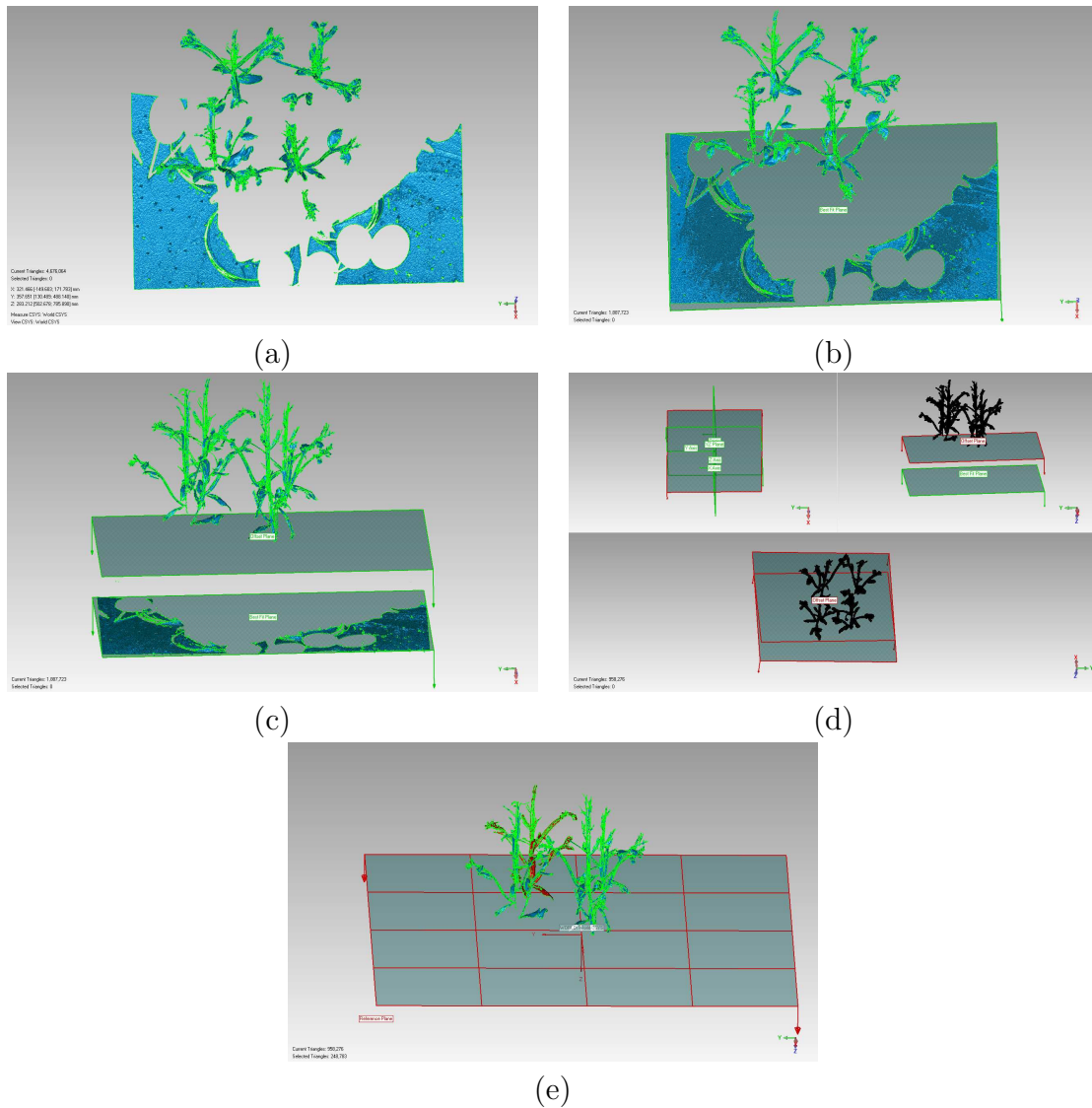


Figure 3.10: Illustration of the volume measurement processing using 65th dataset; (a) The table, used during the scanning process, is re-used as the reference plane to provide consistency during measuring volume to plane, (b) A best fit plane is created using the reference table, (c) Offset plane is created under the plant foliage, (d) Align the offset plane with XY "World Plane", and (e) "Compute Volume to Plane" operation using the aligned XY and offset plane

The proposed methodology is explained below pictorially. It may be noteworthy that the demonstration is based on the 30th showing the vegetative stage of *Arabidopsis thaliana*.

Figures 3.11a-3.11f show the first 6 original raw range images of the 30th dataset collected from the 3D scans of the Arabidopsis plants using the ShapeGrabber Laser Scanner with a 30° rotating angle showing the plants at different views. Figure 3.11a shows the 1st view at 30°, Figure 3.11b shows the 2nd view at 60°, Figure 3.11c shows the 3rd view at 90°, Figure 3.11d shows the 4th view at 120°, Figure 3.11e shows the 5th view at 150°, and Figure 3.11f shows the 6th view at 180°.

Figures 3.12a-3.12f show the rest of the 6 range images of the 30th dataset collected from the 3D scans of the Arabidopsis plants using the ShapeGrabber Laser Scanner with a 30° rotating angle showing the plant at different views. Figure 3.12a shows the 7th view at 210°, Figure 3.12b shows the 8th view at 60°, Figure 3.12c shows the 9th view at 90°, Figure 3.12d shows the 10th view at 120°, Figure 3.12e shows the 11th view at 150°, and Figure 3.12f shows the 12th view at 180°.

Figure 3.13a shows one of the 6 semi-spheres of the 1st view of the 30th dataset, Figure 3.13b shows the same file with the semi-sphere replaced with full sphere data using the estimated center coordinates and radius as well the parametric equations of sphere, Figure 3.13c shows both the semi-sphere and the full sphere files open (both of the files are selected or “active”) in the “Display Manager” of Geomagic Studio 12, and Figure 3.13d shows the plant data after removing the semi-spheres using their estimated center coordinates and radius values.

Figures 3.14a-3.14f show the reconstructed views of the first 6 range images of the 30th dataset with the semi-spheres replaced with full sphere data. Figure 3.14a shows the 1st view, Figure 3.14b shows the 2nd view, Figure 3.14c shows the 3rd view, Figure 3.14d shows the 4th view, Figure 3.14e shows the 5th view, and Figure 3.14f shows the 6th view.

Figures 3.15a-3.15f show the reconstructed views of the second 6 range images of the 30th dataset with the semi-spheres replaced by full sphere data. Figure 3.15a shows the 7th view, Figure 3.15b shows the 8th view, Figure 3.15c shows the 9th view, Figure 3.15d shows the 10th view, Figure 3.15e shows the 11th view and Figure 3.15f shows the 12th view.

Figures 3.16a-3.16f show the first 6 reconstructed views of the 30th dataset after performing the *Convert to Points*, *Sample*, and *Detect Sphere Targets* operations in Geomagic Studio 12. Figure 3.16a shows the 1st view, Figure 3.16b shows the 2nd view, Figure 3.16c shows the 3rd view, Figure 3.16d shows the 4th view, Figure 3.16e shows the 5th view and Figure 3.16f shows the 6th view after performing the aforementioned operations.

Figures 3.17a-3.17f show the second 6 reconstructed views of the 30th dataset after performing the *Convert to Points*, *Sample*, and *Detect Sphere Targets* operations in

Geomagic Studio 12. Figure 3.17a shows the 7th view, Figure 3.17b shows the 8th view, Figure 3.17c shows the 9th view, Figure 3.17d shows the 10th view, Figure 3.17e shows the 11th view, and Figure 3.17f shows the 12th view after performing the aforementioned operations.

Figure 3.18a shows the registered point object after performing “Target Registration” in Geomagic using all the 12 views of the 30th dataset and Figure 3.18b shows the synthesized 3D polygonal mesh obtained from the previously mentioned registered point object with further refinement using “Global Registration” tool in Geomagic.

The area and volume measurement process is not shown here as this is already been covered in Figure 3.10.

The methodology is now explained below pictorially using the 60th showing the flowering stage of *Arabidopsis thaliana*.

Figures 3.19a-3.19f show the first 6 original raw range images of the 60th dataset collected from the 3D scans of the Arabidopsis plants using the ShapeGrabber Laser Scanner with a 30° rotating angle showing the plants at different views. Figure 3.19a shows the 1st view at 30°, Figure 3.19b shows the 2nd view at 60°, Figure 3.19c shows the 3rd view at 90°, Figure 3.19d shows the 4th view at 120°, Figure 3.19e shows the 5th view at 150°, and Figure 3.19f shows the 6th view at 180°.

Figures 3.20a-3.20f show the rest of the 6 range images of the 60th dataset collected from the 3D scans of the Arabidopsis plants using the ShapeGrabber Laser Scanner with a 60° rotating angle showing the plant at different views. Figure 3.20a shows the 7th view at 210°, Figure 3.20b shows the 8th view at 60°, Figure 3.20c shows the 9th view at 90°, Figure 3.20d shows the 10th view at 120°, Figure 3.20e shows the 11th view at 150°, and Figure 3.20f shows the 12th view at 180°.

Figure 3.21a shows one of the 6 semi-spheres of the 1st view of the 60th dataset, Figure 3.21b shows the same file with the semi-sphere replaced with full sphere data using the estimated center coordinates and radius as well the parametric equations of sphere, Figure 3.21c shows both the semi-sphere and the full sphere files open (both of the files are selected or “active”) in the “Display Manager” of Geomagic Studio 12, and Figure 3.21d shows the plant data after removing the semi-spheres using their estimated center coordinates and radius values.

Figures 3.22a-3.22f show the reconstructed views of the first 6 range images of the 60th dataset with the semi-spheres replaced with full sphere data. Figure 3.22a shows the 1st view, Figure 3.22b shows the 2nd view, Figure 3.22c shows the 3rd view, Figure 3.22d shows the 4th view, Figure 3.22e shows the 5th view, and Figure 3.22f shows the 6th view.

Figures 3.23a-3.23f show the reconstructed views of the second 6 range images of the 60th dataset with the semi-spheres replaced by full sphere data. Figure 3.23a shows the 7th view, Figure 3.23b shows the 8th view, Figure 3.23c shows the 9th view,

Figure 3.23d shows the 10th view, Figure 3.23e shows the 11th view and Figure 3.23f shows the 12th view.

Figures 3.24a-3.24f show the first 6 reconstructed views of the 60th dataset without performing the *Convert to Points*, *Sample*, and *Detect Sphere Targets* operations. Figure 3.24a shows the 1st view, Figure 3.24b shows the 2nd view, Figure 3.24c shows the 3rd view, Figure 3.24d shows the 4th view, Figure 3.24e shows the 5th view and Figure 3.24f shows the 6th view.

Figures 3.25a-3.25f show the second 6 reconstructed views of the 60th dataset without performing the *Convert to Points*, *Sample*, and *Detect Sphere Targets* operations in Geomagic Studio 12. Figure 3.25a shows the 7th view, Figure 3.25b shows the 8th view, Figure 3.25c shows the 9th view, Figure 3.25d shows the 10th view, Figure 3.25e shows the 11th view, and Figure 3.25f shows the 12th view.

Figure 3.26 shows the synthesized 3D polygonal mesh obtained after performing “Global Registration” in Geomagic.

3.2 Conclusions

This chapter outlined the proposed methodology followed in this thesis. It describes the two major components of our work: automation of the registration process and measuring the growth cycle. The pre-processing methods to overcome the incomplete sphere data problem were introduced. We demonstrated our methods using the range images from the 30th dataset of the *Arabidopsis thaliana* plants.

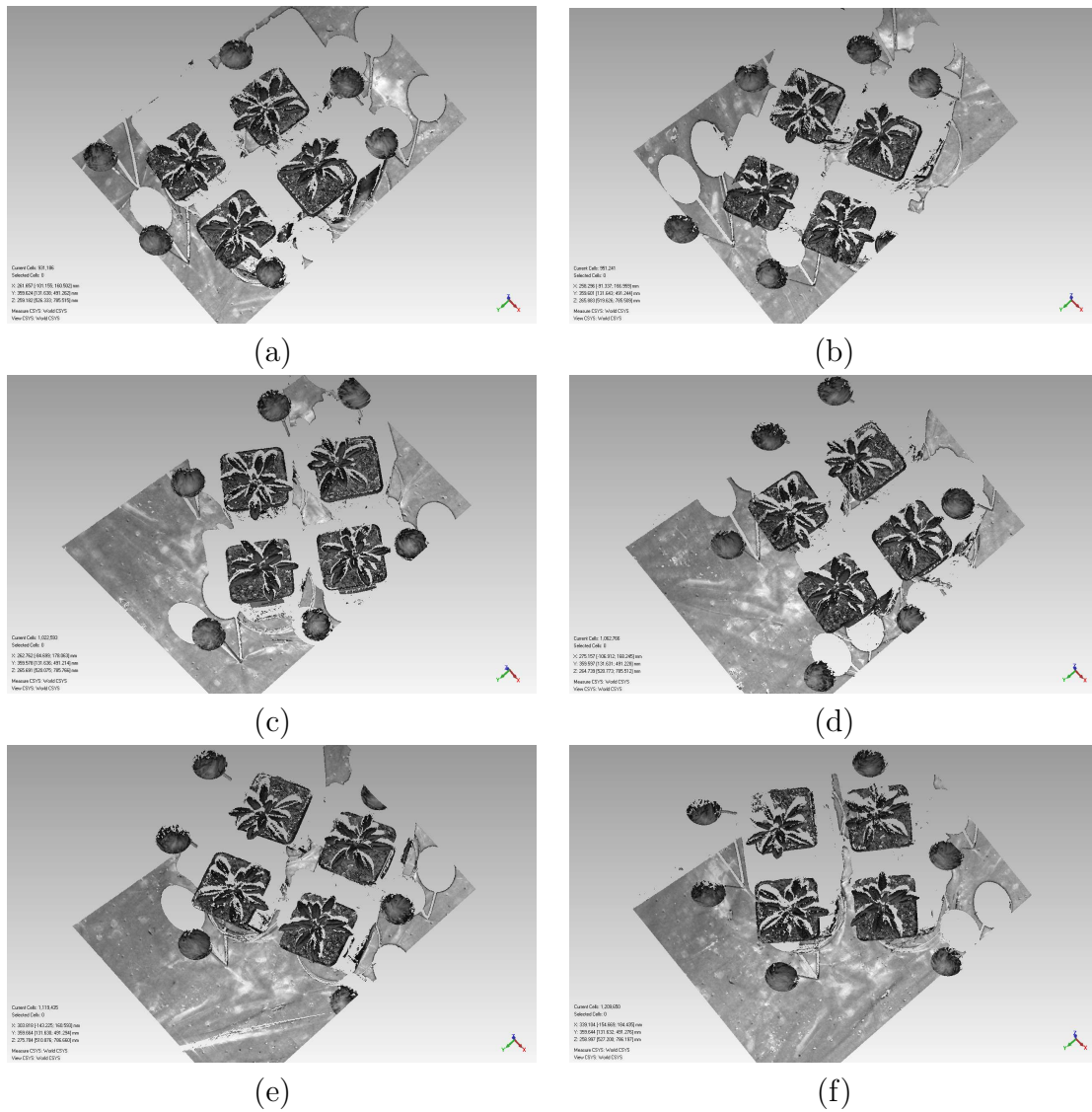


Figure 3.11: The first 6 original raw range images of the 30th dataset collected from the 3D scans of the *Arabidopsis thaliana* plants using the ShapeGrabber Laser Scanner with a 30° rotating angle showing the plant at different views; (a) the 1st view at 30°, (b) the 2nd view at 60°, (c) the 3rd view at 90°, (d) the 4th view at 120°, (e) the 5th view at 150°, and (f) the 6th view at 180°.

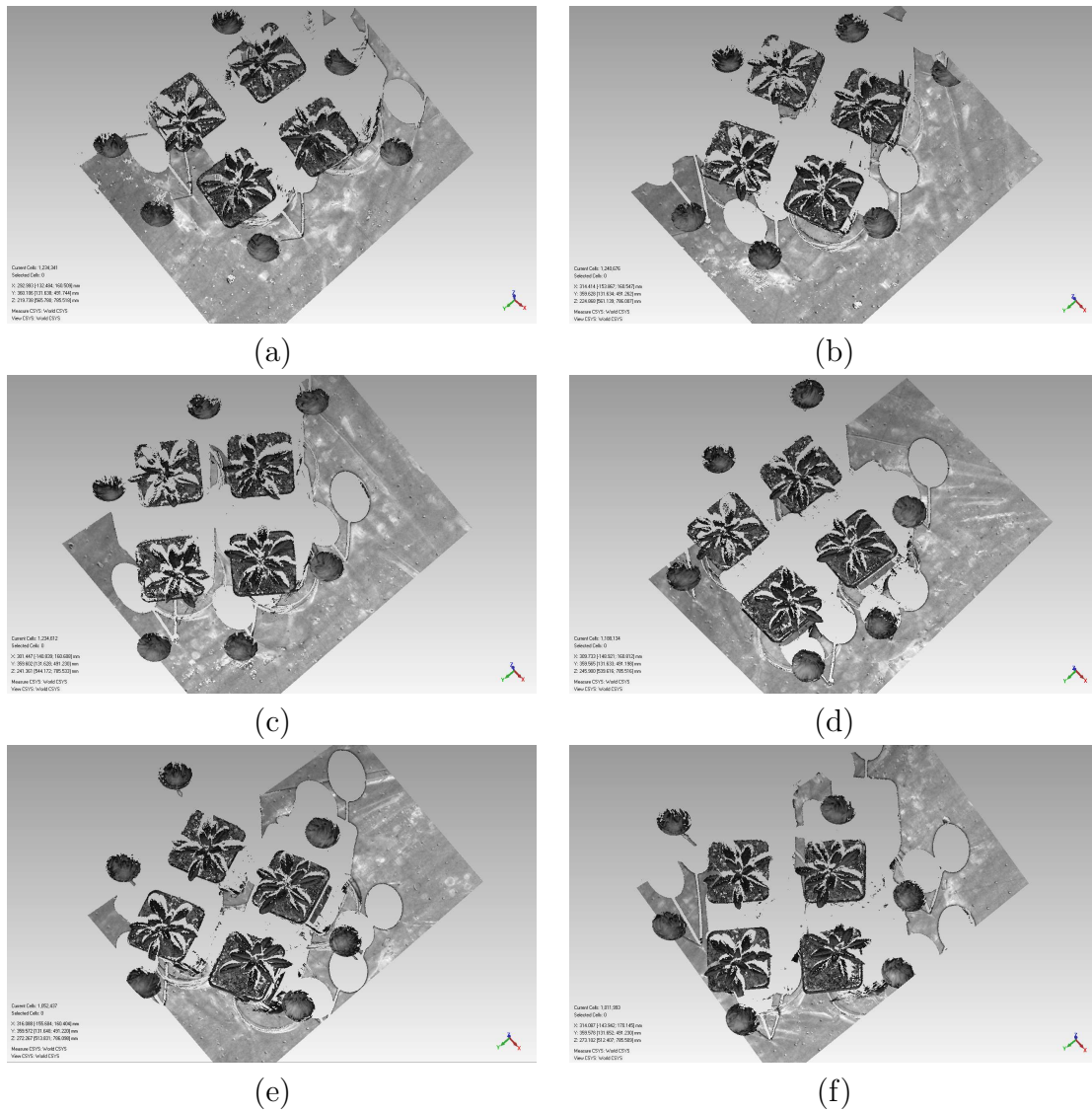


Figure 3.12: The rest of the 6 original raw range images of the 30th dataset collected from the 3D scans of the *Arabidopsis thaliana* plants using the ShapeGrabber Laser Scanner with a 30° rotating angle showing the plant at different views; (a) the 7th view at 210°, (b) the 8th view at 60°, (c) the 9th view at 90°, (d) the 10th view at 120°, (e) the 11th view at 150°, and (f) the 12th view at 180°.

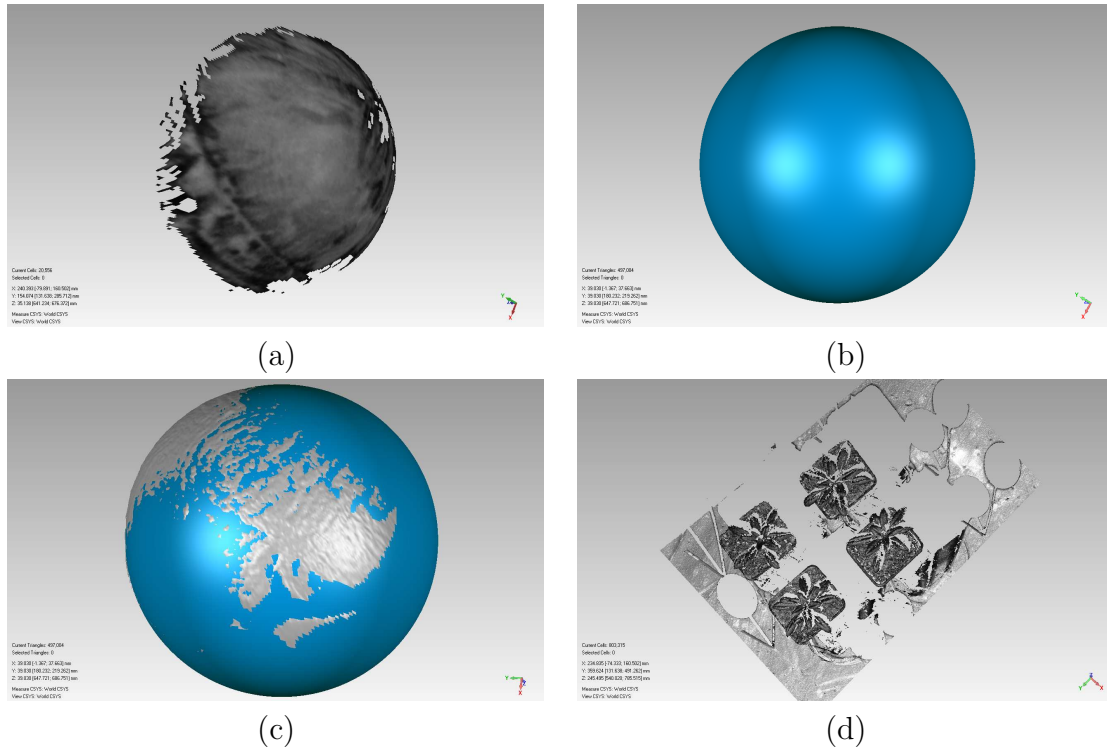


Figure 3.13: Demonstration of the semi-sphere and plant data segmentation phase and the replacement of semi-spheres with full sphere data phase using the 1st view of the 30th dataset; (a) One of the 6 semi-spheres of the 1st view of the 30th dataset segmented manually using Geomagic Studio 12, (b) the same file with the semi-sphere replaced with a full sphere using the estimated center coordinates and radius as well as the parametric equations of sphere, (c) both the semi-sphere and the full sphere files are opened in the “Display Manager” of Geomagic Studio 12, (d) the plant data after removing the semi-spheres using their estimated center coordinates and the radius.

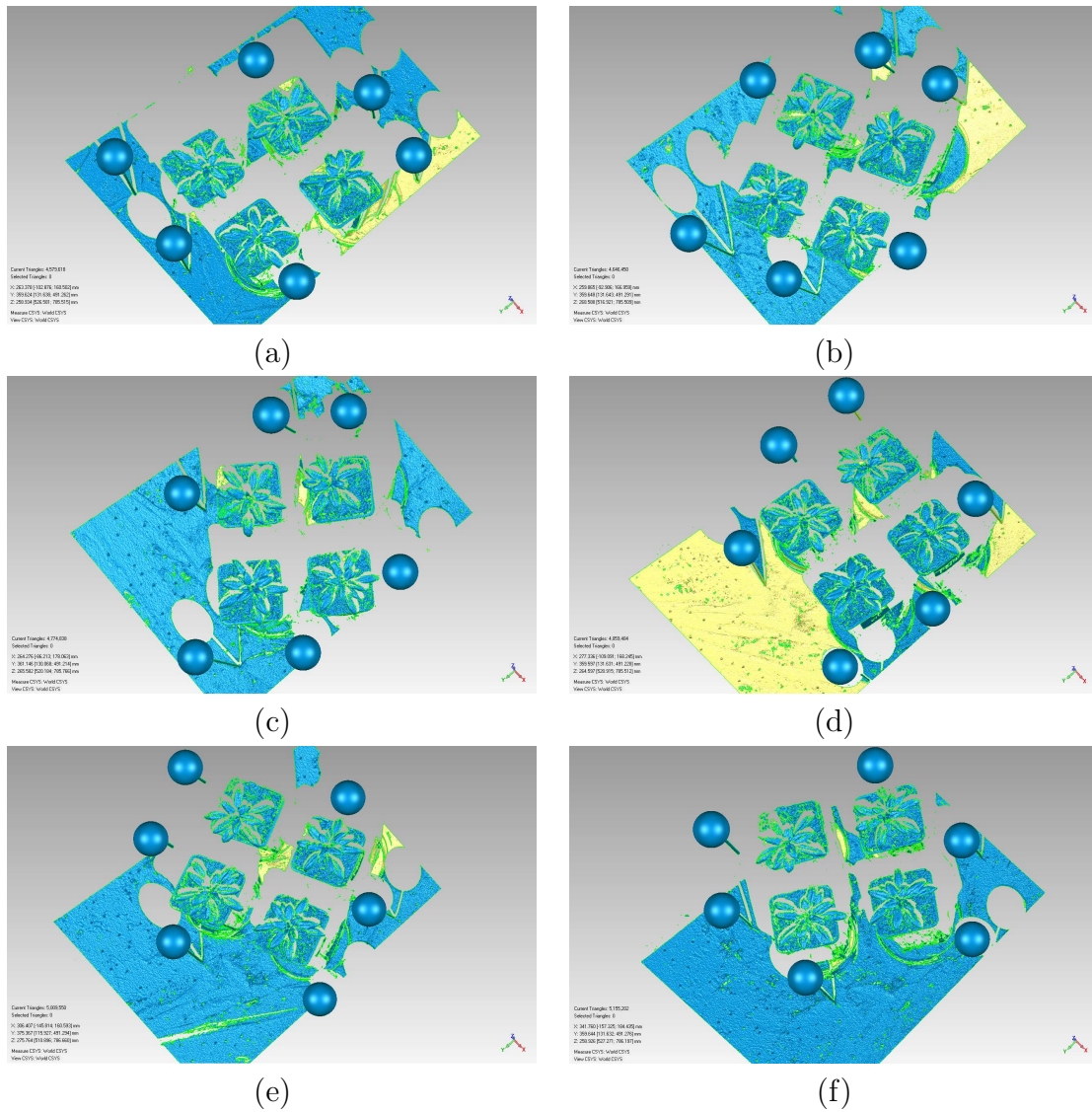


Figure 3.14: The reconstructed views of the first 6 range images of the 30th dataset with the semi-spheres replaced with full sphere data; (a) the 1st view, (b) the 2nd view, (c) the 3rd view, (d) the 4th view, (e) the 5th view, and (f) the 6th view.

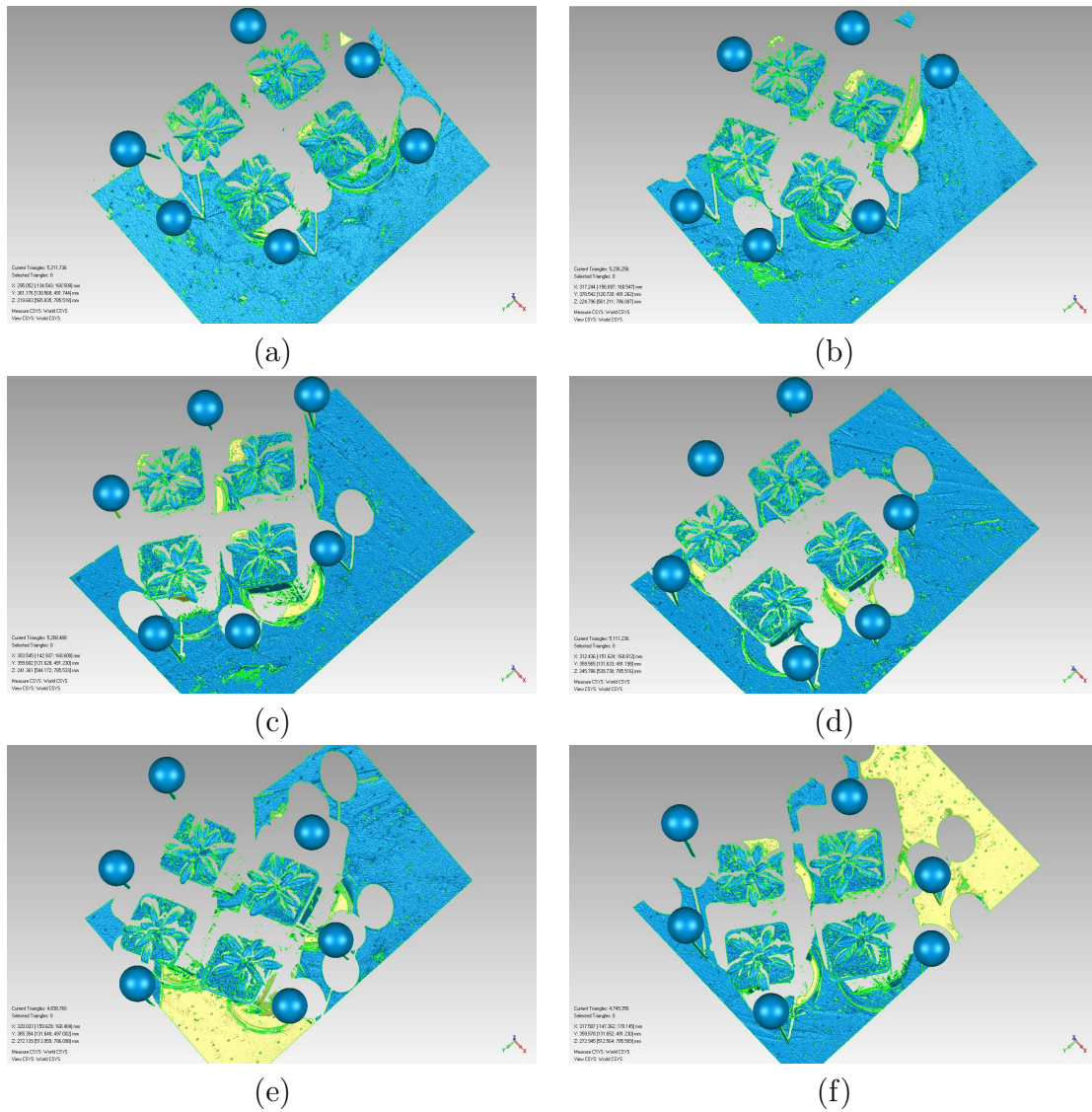


Figure 3.15: The reconstructed views of the second 6 of the 12 range images of the 30th dataset with the semi-spheres replaced with full sphere data; (a) the 7th view, (b) the 8th view, (c) the 9th view, (d) the 10th view, (e) the 11th view and (f) the 12th view.

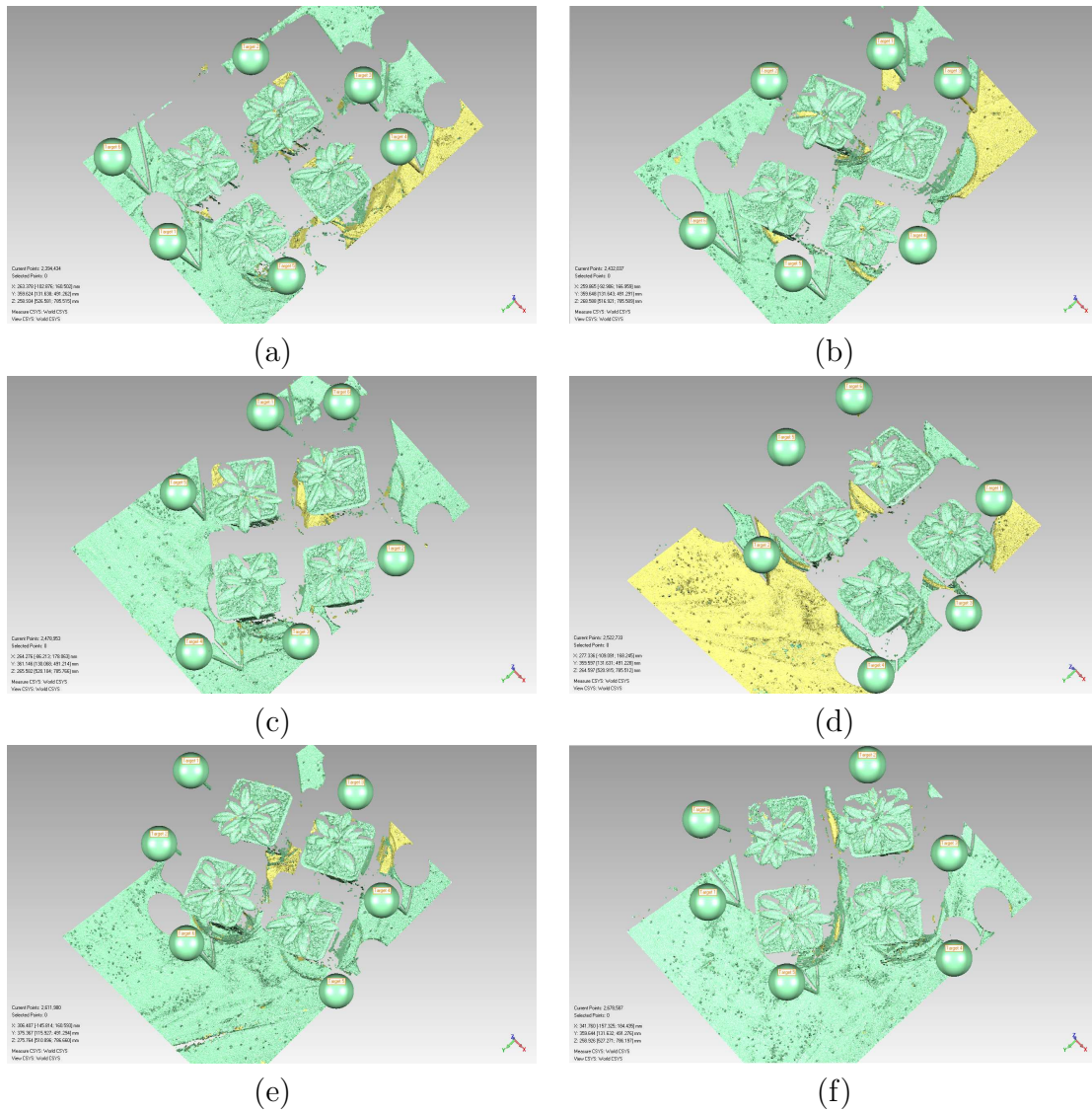


Figure 3.16: The first 6 reconstructed views of the 30th dataset after performing the Convert to Points, Sample, and Detect Sphere Targets operations in Geomagic Studio 12; (a) the 1st view, (b) the 2nd view, (c) the 3rd view, (d) the 4th view, (e) the 5th view, and (f) the 6th view.

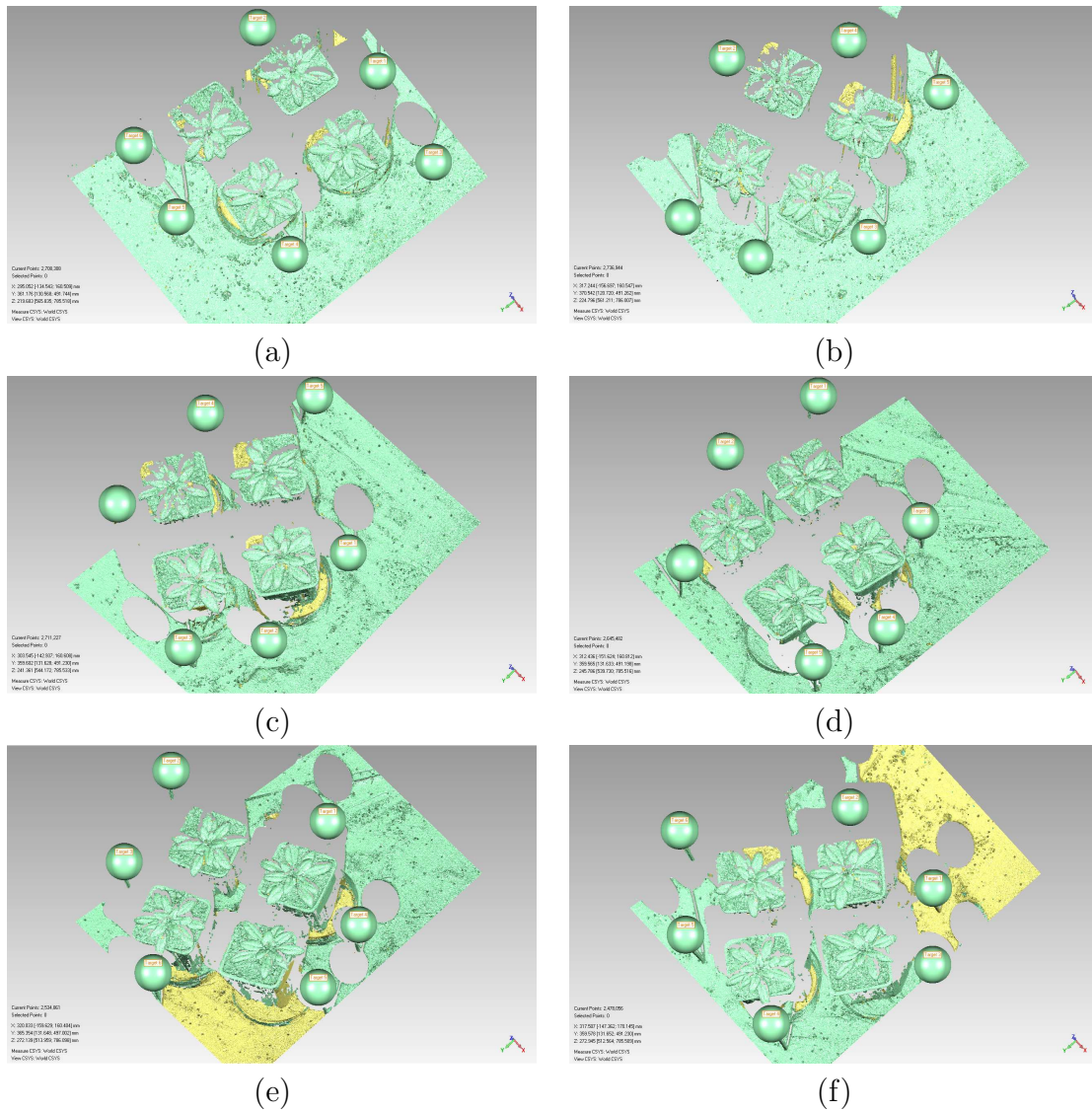


Figure 3.17: The second 6 reconstructed views of the 30th dataset after performing the Convert to Points, Sample, and Detect Sphere Targets operations in Geomagic Studio 12; (a) the 7th view, (b) the 8th view, (c) the 9th view, (d) the 10th view, (e) the 11th view, and (f) the 12th view.

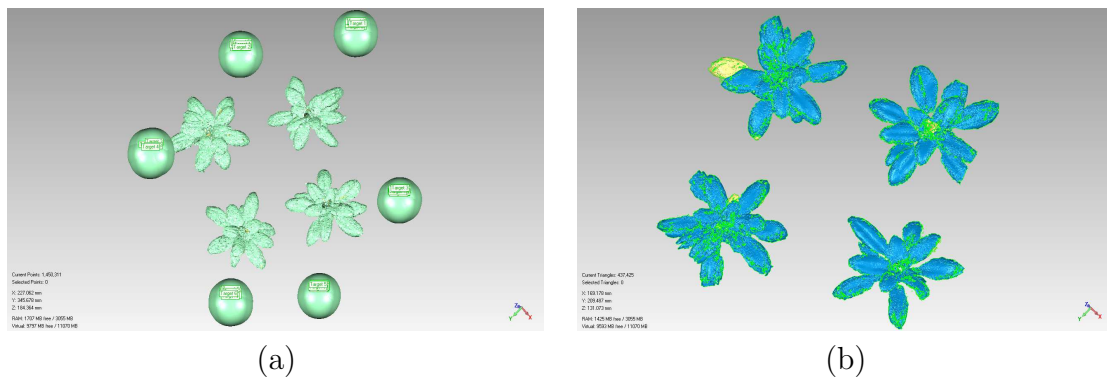


Figure 3.18: Illustration of the registration phase using all the 12 views of the 30th dataset; (a) The registered point object after performing “Target Registration” in Geomagic using all the 12 views of the 30th dataset and (b) the synthesized 3D polygonal mesh obtained from the previously mentioned registered point object with further refinement using “Global Registration” tool in Geomagic.

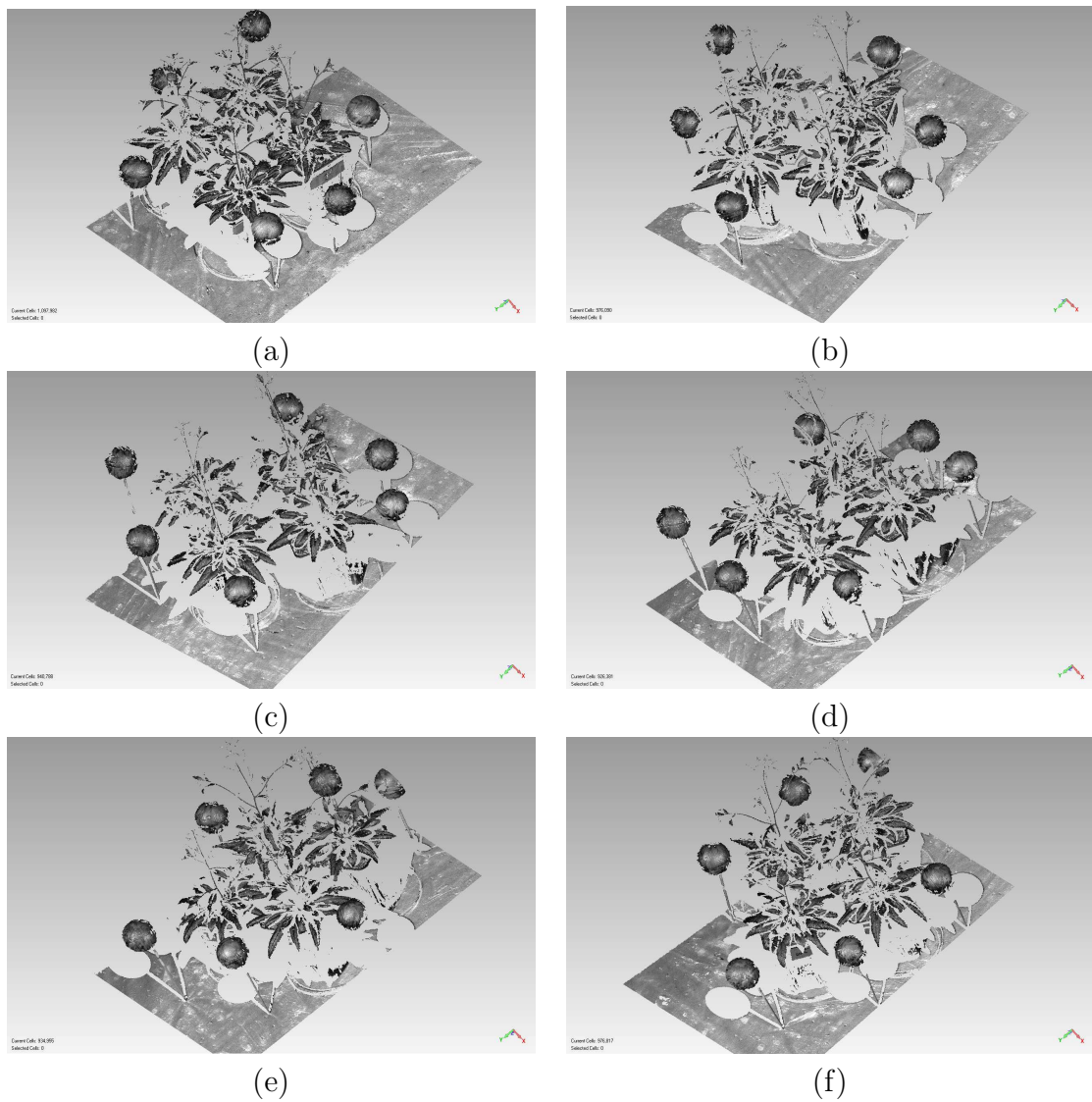


Figure 3.19: The first 6 original raw range images of the 60th dataset collected from the 3D scans of the *Arabidopsis thaliana* plants using the ShapeGrabber Laser Scanner with a 60° rotating angle showing the plant at different views; (a) the 1st view at 30°, (b) the 2nd view at 60°, (c) the 3rd view at 90°, (d) the 4th view at 120°, (e) the 5th view at 150°, and (f) the 6th view at 180°.

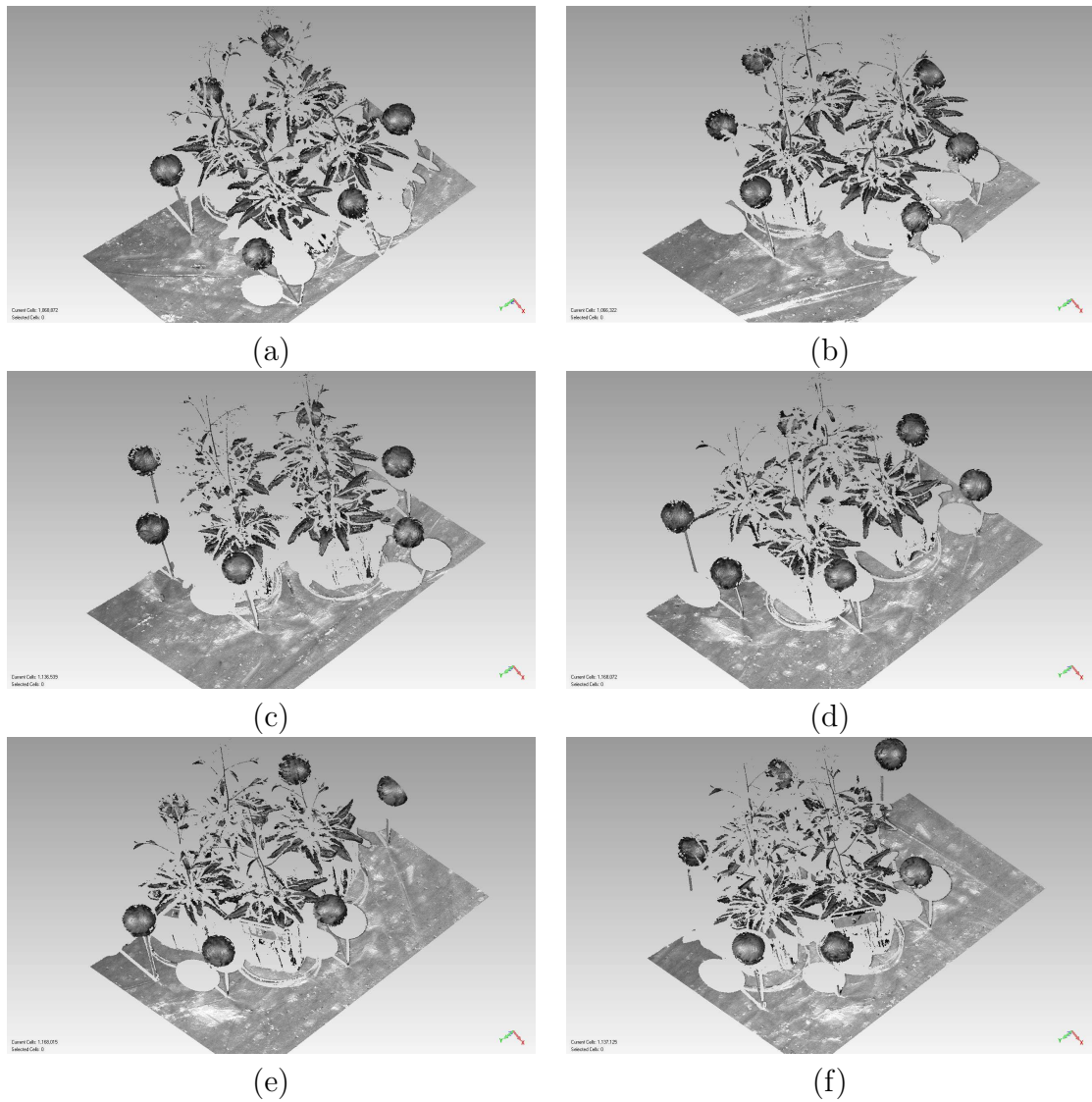


Figure 3.20: The rest of the 6 original raw range images of the 60th dataset collected from the 3D scans of the *Arabidopsis thaliana* plants using the ShapeGrabber Laser Scanner with a 60° rotating angle showing the plant at different views; (a) the 7th view at 210°, (b) the 8th view at 60°, (c) the 9th view at 90°, (d) the 10th view at 120°, (e) the 11th view at 150°, and (f) the 12th view at 180°.

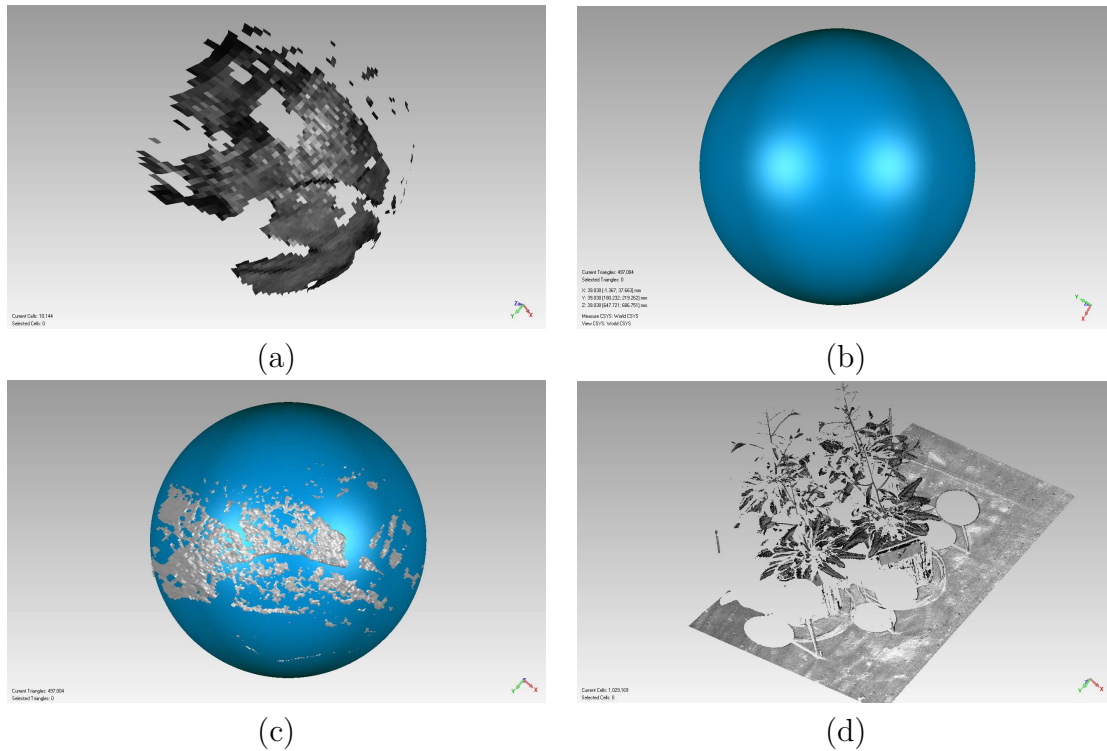


Figure 3.21: Demonstration of the semi-sphere and plant data segmentation phase and the replacement of semi-spheres with full sphere data phase using the 1st view of the 60th dataset; (a) One of the 6 semi-spheres of the 1st view of the 60th dataset segmented manually using Geomagic Studio 12, (b) the same file with the semi-sphere replaced with a full sphere using the estimated center coordinates and radius as well as the parametric equations of sphere, (c) both the semi-sphere and the full sphere files are opened in the “Display Manager” of Geomagic Studio 12, (d) the plant data after removing the semi-spheres using their estimated center coordinates and the radius.

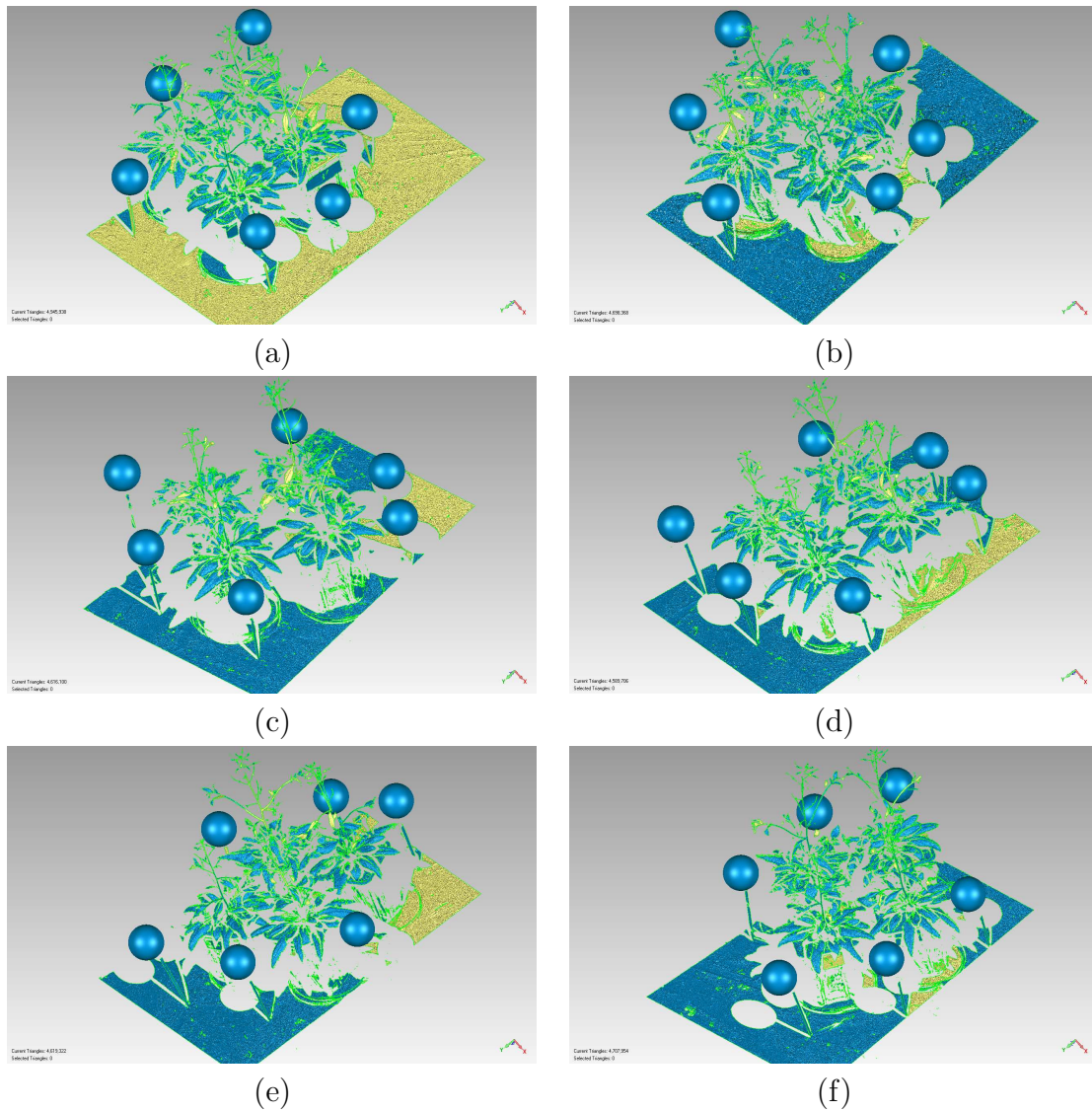


Figure 3.22: The reconstructed views of the first 6 range images of the 60th dataset with the semi-spheres replaced with full sphere data; (a) the 1st view, (b) the 2nd view, (c) the 3rd view, (d) the 4th view, (e) the 5th view, and (f) the 6th view.

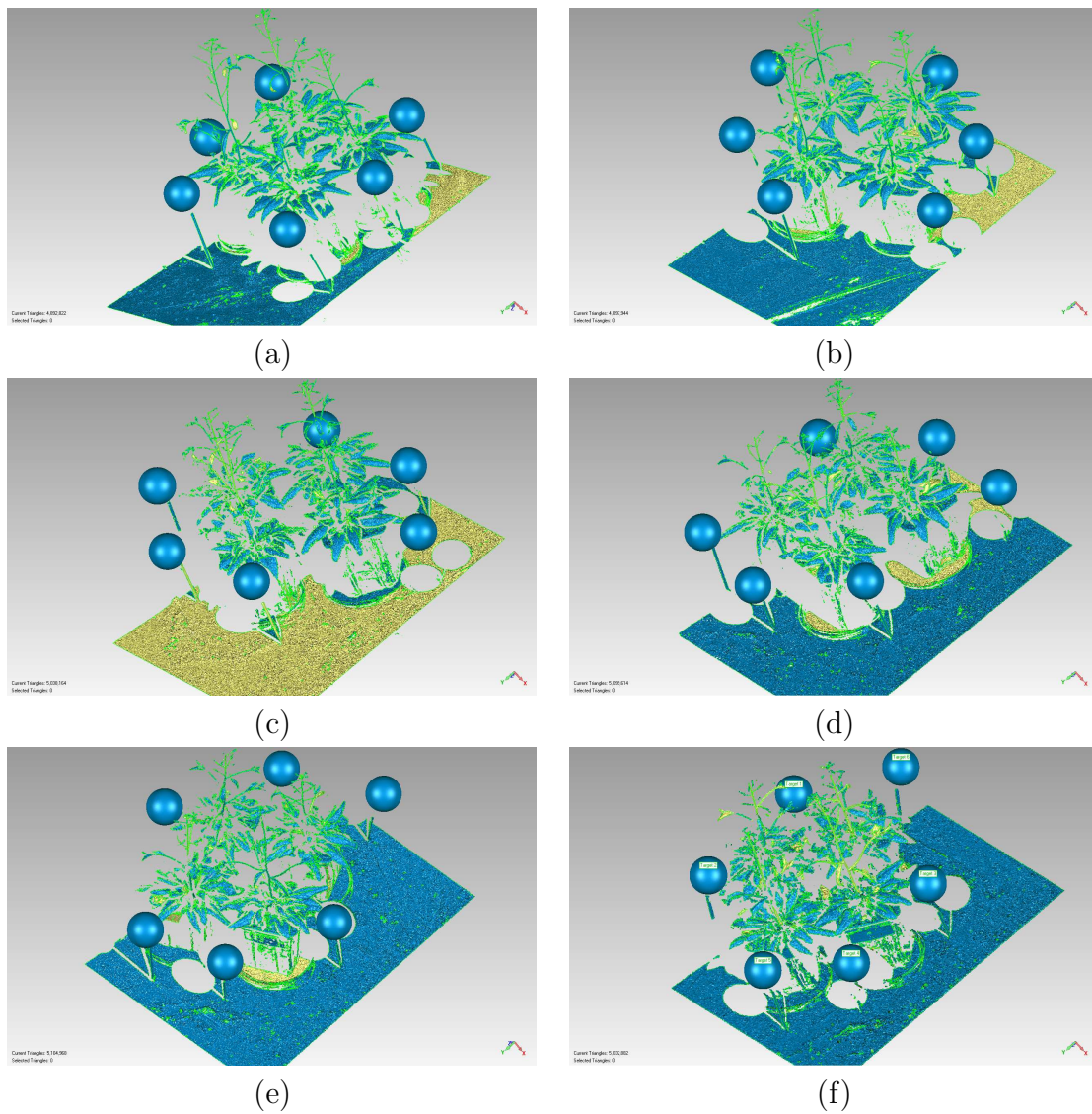


Figure 3.23: The reconstructed views of the second 6 of the 12 range images of the 60th dataset with the semi-spheres replaced with full sphere data; (a) the 7th view, (b) the 8th view, (c) the 9th view, (d) the 10th view, (e) the 11th view and (f) the 12th view.

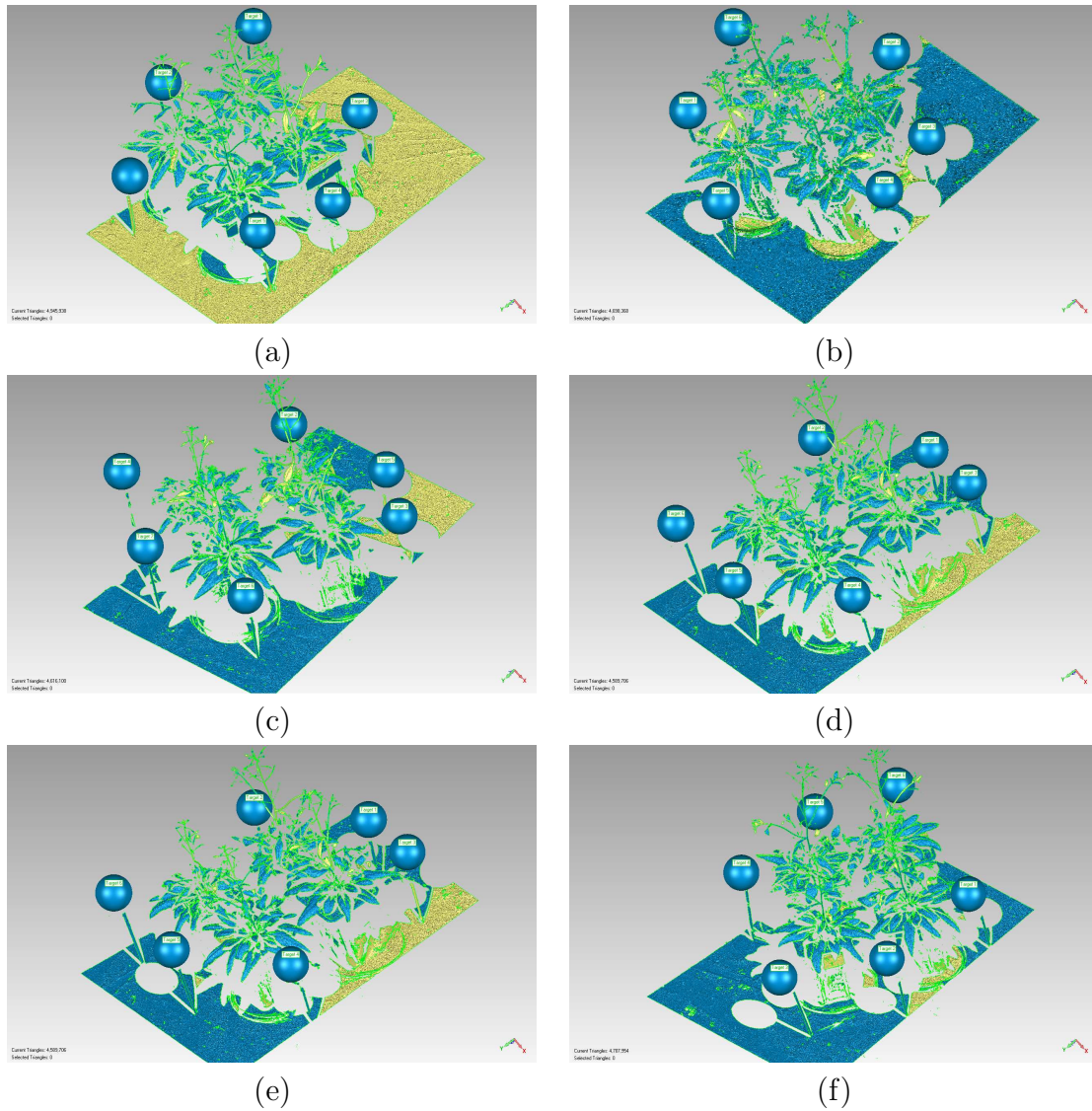


Figure 3.24: The first 6 reconstructed views of the 60th dataset; (a) the 1st view, (b) the 2nd view, (c) the 3rd view, (d) the 4th view, (e) the 5th view, and (f) the 6th view.

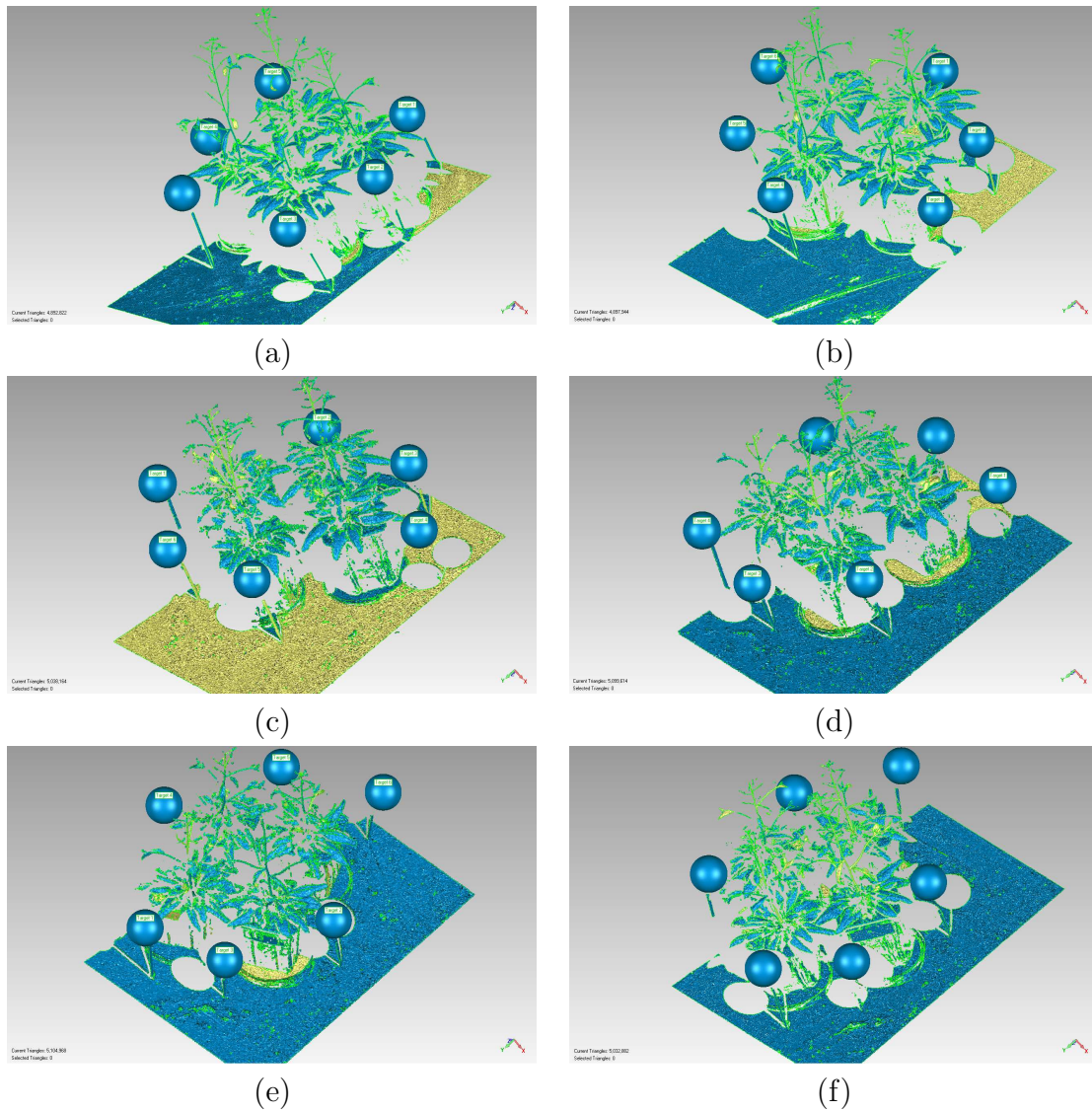


Figure 3.25: The second 6 reconstructed views of the 60th dataset; (a) the 7th view, (b) the 8th view, (c) the 9th view, (d) the 10th view, (e) the 11th view, and (f) the 12th view.

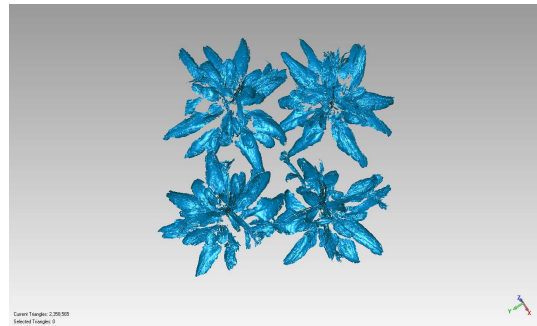


Figure 3.26: the synthesized 3D polygonal mesh obtained from dataset 60 using “Global Registration” tool in Geomagic

Chapter 4

Results and Discussion

This chapter discusses various problems encountered when processing Yang’s Arabidopsis range datasets. It also gives experimental results and a discussion, followed by a description of the various methods used to validate the measurements of plant growth and other experimental outcomes (i.e., the validation of the parameter estimation methods).

4.1 Problems with the *Arabidopsis thaliana* Datasets

During our experiments, we observed that Yang’s *Arabidopsis thaliana* datasets [16] had the following problems:

4.1.1 Missing Datasets

It is a good thing that plant growth measurement using Yang’s datasets is not the main goal of this thesis. We cannot find 30 range views (from the 7th view of the 51st dataset to the 12th view of the 53rd dataset)¹.

4.1.2 Validating the Experimental Outcomes

We do not have any “gold standard” measurements to validate our experimental outcomes. The reasons are twofold:

¹We contacted Yang about this and she said the datasets must be “lost”.

1. **No Available *Manual* Measurements:** To validate our experimental results, comparisons should have been made between the measured volumes of *Arabidopsis thaliana* obtained from the 3D triangular meshes and that of from the manual measurement process (e.g., “wet volume” measurements). Yang [16] tried to do this with measuring the volume of *Arabidopsis thaliana* plants by submerging the entire plant in the water and measuring the volume of the displaced water (this is Archimedes principle). To do this, Yang cut off a complete *Arabidopsis* plant from its root and put its body into a cylinder containing 450 ml water. Theoretically, the plant volume can be estimated by calculating the difference between the volume of the water with and without the plant. However, Yang was unable to measure the volume due to the air bubbles trapped inside the cylinder. She tried to prevent the formation of these air bubbles by creating a vacuum environment for the cylinder fastening a sheet of rubber over the cylinder’s top and sucking the air out but this did not work. Even with these air bubbles, Yang could have conducted these wet volume measurements but unfortunately she did not. As a result, we do not have any volume data from the “wet volume” measurement process to validate our experimental outcomes. Figure 4.1a shows the experimental setup used by Yang during her “wet volume” measurement process and Figure 4.1b shows the air bubbles trapped inside the cylinder due to which she was unable to measure the “wet volume” of *Arabidopsis* plants successfully.
2. **Problem with Yang’s Result:** With no volume data from the manual measurement process, we try to compare our areas and volumes with Yang’s result. But we are unable to do so due to the following problems:
 - i. Because trimming of unnecessary elements (for example, the table, the pots and the soil) from the 3D triangular meshes was performed by manual editing, comparison between the area and volume data of Yang and ours becomes subjective (because Yang’s trimming cannot be reproduced). In order to quantitatively compare our results with Yang’s, her trimmed images are required (and these were not saved).
 - ii. In her thesis, Yang presented her experimental outcomes (i.e. the areas and volumes of *Arabidopsis thaliana*) for each day. But we are provided with the scanned images whose filenames have no information on which day they were scanned. As a result, we cannot be 100% certain about the mapping of a specific dataset with the actual day on which they were scanned.

Because of these aforementioned reasons, we are unable to draw any definite comparisons between our experimental results and Yang’s result.

We know that Yang conducted her experiments for 25 days starting at 8:30 P. M., February 4th, 2010 and ending at 7:46 P. M., February 28th, 2010 (as

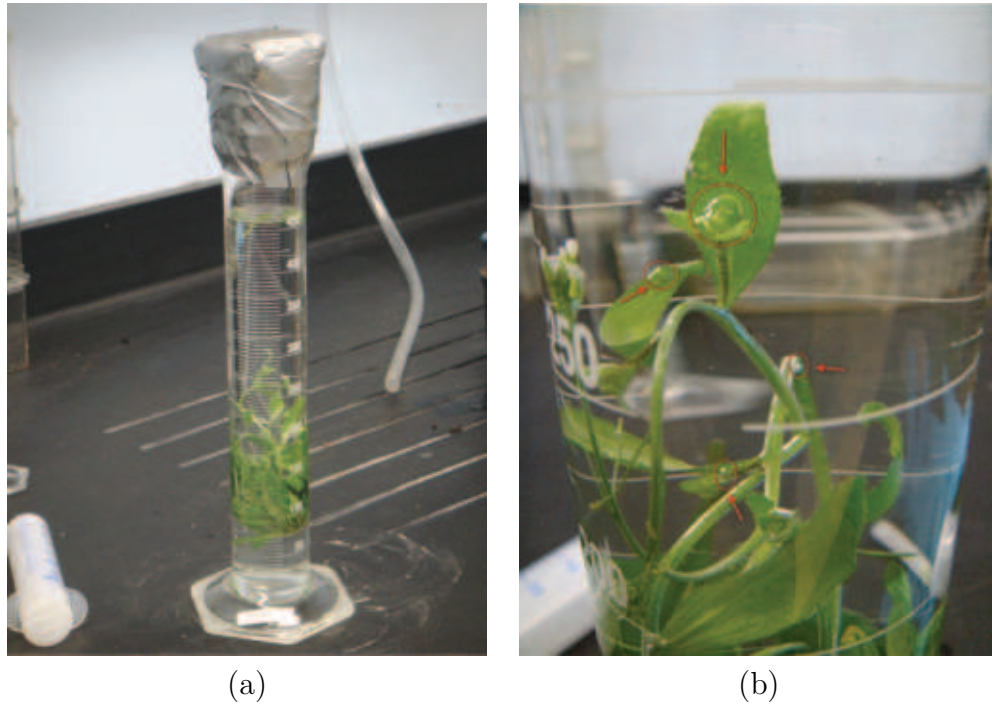


Figure 4.1: Illustration of the experimental setup used by Yang for measuring the “wet volumes” of one of the plants in the lab; (a) Cylinder containing 450 ml Water to Perform the Analog Measurement, (b) Air Bubbles Trapped in the Water. [16]

described in her thesis). She performed 3 scans daily so there should be 75 datasets. However, there are 75 datasets (with 30 range views missing). We mapped each dataset with Yang’s times by mapping her 1st dataset to 8:30 P.M., February 4th. We believe this mapping is the correct one.

4.1.3 Problems with Manual Processing

The major problem with the manual processing the the 3D triangular meshes is that the manual processing directly affects the accuracy of the calculation of plant’s growth (i.e. the areas and the volumes). Specifically, trimming the extraneous mesh components affiliated with plant leaves (for example, the soil) adversely affects the measuring accuracy. Figure 4.2a and 4.2b are examples of plant leaves adjacent to soil. Because there is no well defined edge between the leaf and the soil, ambiguity arises when separating the soil from the leaf in the 3D triangular mesh. We approach this problem in a similar manner as Yang did in her thesis. Using Geomagic Studio 12, a red line is drawn near the leaf edge and all the affiliated components outside

that line are trimmed away (Figure 4.2c). However, this approach could not generate a complete and accurate shape of the leaves in the 3D triangular meshes successfully (we are conservative in that mesh components that are part of the plant and the soil are not trimmed). Moreover, due to the manual nature of this pre-processing phase, enormous time and labor are required to complete the measurement of plant growth.

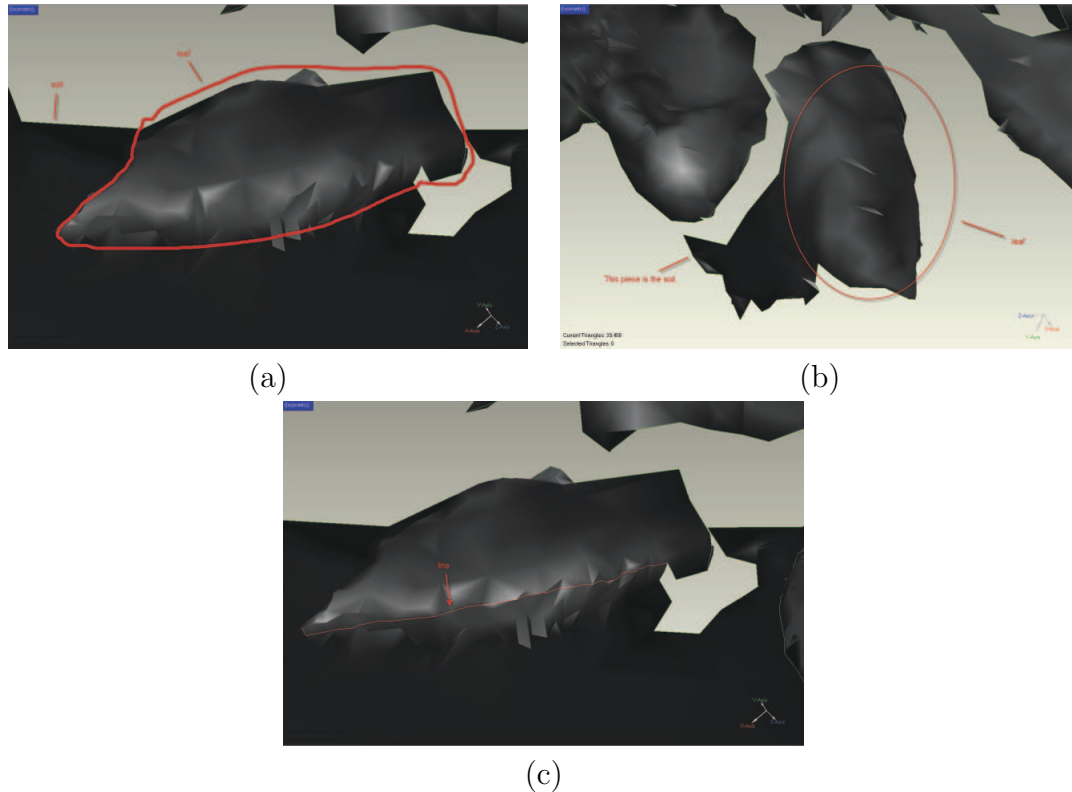


Figure 4.2: Problems with manual pre-processing of 3D triangular meshes; (a) 3D range image of one of the leaves where the leaf is inside the red colored line and the soil is under the leaf, (b) another leaf and its affiliated components highlighted with red circle, and (c) 3D range image of one of the leaves and its affiliated components highlighted with red line [16].

4.2 Methods of Validation

4.2.1 Validation of Sphere Fitting Algorithms

We measure the radius of each reference spheres (i.e. the ping pong balls) used by Yang using an electronic caliper (with the accuracy of 0.02 of a mm) and compare

the values with the resultant radii obtained from our LS and M-Estimation methods. Yang did not mark the balls with any indicator. Therefore, we were unable to identify specific spheres in the range images. Because of this, comparing individual radius values was impossible. Because the physical radius values of the 6 ping pong balls differ from each other (slightly), we use an average radius value to compare our results with the manually annotated values. Figure 4.3a shows the electronic caliper used to measure the radius and Figure 4.3b shows the radius measurement of one of the reference spheres using the electronic caliper.

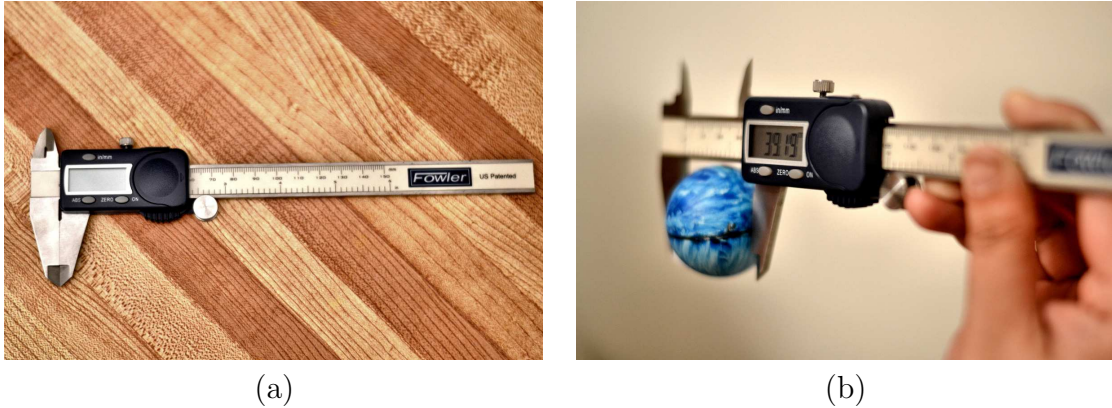


Figure 4.3: Illustration of the radius measurement process of one of the reference spheres using electronic caliper; (a) The electronic caliper used in the lab to measure the radius and (b) The radius measurement process of one of the reference spheres using electronic caliper.

Thus, we also verify the quality of the fitting based on average residual values. The residual of a sample is the difference between the sample or the experimental value and the predicted or estimated value by the function. The “norm of the residual” is an indicator of the goodness of the fit (i.e. a lower norm signifies a better fit). We compute the average norm of the residual using Eq. (4.1) to analyze the performance of the our fitting algorithms:

$$\text{Average Residual} = \frac{\sum_{i=0}^n \|d_i\|^2}{n}, \quad (4.1)$$

where n is the total number of samples and d_i is the residual of the i^{th} sample.

4.2.2 Validation of the Registration Process

The accuracy of the plant 3D surface area and 3D volume measurement depends on the performance of the registration process to a great extent. The better the

registration process, the accurate the plant growth measurement will be. To get a better result, the identical areas of multiple images need to be properly merged or overlapped during registration. If these areas are not properly merged, the distance between any two points of these areas in multiple images will increase resulting larger area or volume of objects in the merged model than their physical area or volume. Because large distance will result in multiple pseudo edges of an object. So, during our experiment, we recorded the average distance and standard deviation of any two points after completing the registration process. For instance, we merged 12 reconstructed range images to generate a single polygonal mesh. Assuming that I_1, I_2, \dots, I_{12} are the 12 images, we have N_1, N_2, \dots, N_{12} set of points (the triangular facet vertices) belong to the respective images. If $n_1 \in N_1, n_2 \in N_2, \dots, n_{12} \in N_{12}$, then the average distance and standard deviation between any two of these points, D_{Avg} and D_{Std} , indicate that on an average the distance between any two such points is D_{Avg} with standard deviation D_{Std} . Naturally, smaller values of D_{Avg} and D_{Std} is preferred; smaller values indicates significant overlapping of the points after the registration process. From these values, we can determine the quality of the merge calculation and this the quality of convergence we achieved during the registration.

4.2.3 Validation of Plants Areas and Volumes

As mentioned earlier, that we do not have any “gold standard” area and volume measurements to compare our area and volume values for validation purposes. However, we compare the pattern of our growth rate with Yang’s results for two subsets of the datasets.

4.3 Experimental Results and Discussion

4.3.1 Performance Analysis of the Parameter Estimation Techniques

To verify the performance of our parameter estimation technique, we measured the radius of each reference sphere using the electronic caliper. We refer to these measurements as the “physical radii” or “actual radii”. The average physical radii, $r_{physical}$, and their standard deviations of the physical radii are:

$$r_{physical} = 19.563\text{mm}, \text{ standard deviation} = 0.059\text{mm}.$$

Table 4.1 shows the experimental results of the radii (average and standard deviation values) obtained from the LS, Huber and Bisquare estimators for datasets 30-40. Similar results are shown in Table 4.2 for datasets 60-70. Both Table 4.1

and Table 4.2 show that in most cases, the Bisquare estimator outperforms the LS and Huber estimators, except for those “highlighted” table entries showing exceptions. Although, for some cases, the average $r_{Bisquare}$ value compares poorly with the average r_{LS} values, the *standard deviations* corresponding to those table entries show that Bisquare performs better than LS, in practice. The only exceptions are for two particular datasets, 39 and 40. This is possibly a side-effect of the poor “initial guess” provided by the LS estimator. Note that among all the datasets, these two exhibit high standard deviation values for LS. Because Bisquare is very sensitive to the “initial guess”, a poor starting value can drastically reduce its performance. The performance of the Huber estimator is poorer than the Bisquare estimator, but, in most cases, it is better than for the LS estimator.

On the other hand, Table 4.3 shows the experimental average residual values (average values and standard deviations) obtained for the LS, Huber and Bisquare estimators for datasets 30-40. Similar results are shown in Table 4.4 for datasets 60-70. Both Table 4.3 and Table 4.4 show that the performances of all the three fitting algorithms are quite similar, where “small” values in these table entries indicate a better fitting by these estimators. However, for some cases, LS outperforms Bisquare estimator as indicated by both the average and standard deviation residual values. Detailed information can be found in Appendices A, B, C, and D.

We note that LS is optimal for mean zero Gaussian error. Indeed, a robust estimator can do at most as well as LS if the error is mean zero Gaussian. But this depends on the parameters for the robust estimator being well chosen. Of course, if the input error is not mean zero Gaussian a robust estimator will almost certainly be better. Our data is rough mean zero Gaussian but with sometimes the semi-sphere segmentation data contains non-sphere data, which a robust estimator can eliminate. In general, it is a good idea to start a robust estimation off with a LS estimate as the initial guess.

From the data in Tables 4.1, 4.2, 4.3 and 4.4, we make the following conclusions:

1. Our experimental outcomes support our claim that the Bisquare estimator is very sensitive to “initial guess”. We believe that the poorer performance showed by this estimator in one or two cases is a side-effect of the poor “initial guess” provided by the LS estimator. Of course, the LS performance, in terms of the average radius and standard deviation values is poor as well.
2. Based on our experimental datasets, the performance of all three estimators is similar in most cases. However, on average, the Bisquare estimator provides better fitting. However, if both performance and simplicity are our selection criteria, then the LS estimator is the best among these three estimators. We were unable to find any cases where the Huber estimator outperformed both the LS and the Bisquare estimators. However, the Huber estimator performance

is better than the LS estimator in some cases, albeit the difference is almost negligible.

3. If average residual only is considered, all the estimators perform equally in that they all provide similar average residual values. However, in some cases, the LS estimator outperforms the other two estimators. The average residual difference is very small in these cases ($<0.001\text{mm}$).
4. In the case of the LS estimator, the average error is approximately 1.395% whereas the error for Huber and Bisquare estimators are 1.559% and 1.343%, respectively. The standard deviations are 0.651, 1.912 and 1.889 for the LS, the Huber and the Bisquare estimators, respectively. Based on the average errors, the Bisquare estimator seems more effective but based on the standard deviation values, the LS estimator seems better. To verify, we conducted a t-test using the online tool “GraphPad Software” [55] to confirm whether they are statistically significant or not. This test is performed by statisticians to determine whether or not a result found from a sample drawn from a population will also be true for the entire population. To decide whether two means of the same k number of samples are the same or not, we consider the differences between the corresponding means. A null hypothesis which states that the means are drawn from the same population is true if the difference between the means is zero; the difference will be different from zero, otherwise. If the null hypothesis is true, then we say that the means are drawn from the same population and are not statistically significant; if the null hypothesis is rejected, then we say that the means are drawn from different population and statistically significant. So for a given confidence level, we will check whether the actual difference exceeds the confidence limit. The paired t-test compares two paired groups and makes inferences about the size of the average difference between the paired measurements. The most important results are the paired p values and the confidence interval. The paired p value (if we assume that the null hypothesis is true, is the probability of obtaining a test statistic at least as extreme as the one that was actually observed). For the LS-Huber pair, p 0.6338, for the Huber-Bisquare pair, p is 0.0001 and for the Bisquare-LS pair p is 0.8815. Now, according to the definition of p , if any of these p -values is less than or equal to a predefined threshold, then the null hypothesis is rejected. In this experiment, we have chosen this threshold (indicating significance level) to be at 0.05 (and hence the confidence interval is 95%) which is the conventional threshold. In this way, only the difference between Huber-Bisquare pair is considered to be statistically significant. The p for the other two pairs show they are not statistically significant. So, from the paired t-test conducted on the average errors of the three estimators, we see that the means are not statistically significant for the LS-Huber and the Bisquare-LS pairs. However, we found it to be statistical significant for the Huber-Bisquare pair. Being statistical

Average Radius \pm Standard Deviation			
Dataset	LS	Huber	Bisquare
30	19.805 \pm 0.349	19.741 \pm 0.247	19.711 \pm 0.211
31	19.829 \pm 0.374	19.766 \pm 0.274	19.737 \pm 0.238
32	19.839 \pm 0.384	19.777 \pm 0.287	19.745 \pm 0.252
33	19.786 \pm 0.326	19.722 \pm 0.227	19.691 \pm 0.195
34	19.791 \pm 0.338	19.731 \pm 0.233	19.701 \pm 0.196
35	19.799 \pm 0.348	19.741 \pm 0.245	19.714 \pm 0.210
36	19.868 \pm 0.643	19.792 \pm 0.449	19.691 \pm 0.234
37	19.888 \pm 0.656	19.811 \pm 0.463	19.707 \pm 0.241
38	19.888 \pm 0.655	19.815 \pm 0.464	19.712 \pm 0.244
39	19.978 \pm 1.066	21.333 \pm 4.207	21.312 \pm 4.180
40	20.187 \pm 1.391	20.571 \pm 2.326	20.448 \pm 2.060

Table 4.1: Estimated average radius and standard deviation values for the reference spheres in datasets 30-40 using the LS, Huber and Bisquare estimators.

significant, the Bisquare estimator should perform significantly better than the Huber estimator for the sample, as well as the entire population. However, because the results are not statistically significant for the other two estimator pairs, LS-Huber and Bisquare-LS, if they are applied to the entire population, it cannot be guaranteed that the pairs perform as well on the whole populations as they did on the sample.

4.3.2 Performance Analysis of the Registration Process

Tables 4.5 and 4.6 show the performance of the registration process used in this thesis based on two parameters, the average residual and the standard deviation of the distance of two points after the completion of convergence process for datasets 30-40 and datasets 60-70, respectively. The overall average residual and standard deviation obtained from Table 4.5 for datasets 30-40 are:

$$\text{Average Distance}_{\text{Between Two Points}}, \bar{d} = 0.433\text{mm}, \text{standard deviation} = 0.352\text{mm}. \quad (4.2)$$

The overall average residual and deviation obtained from Table 4.6 for datasets 60-70 are:

$$\text{Average Distance}_{\text{Between Two Points}}, \bar{d} = 0.601\text{mm}, \text{standard deviation} = 0.551\text{mm}. \quad (4.3)$$

From these results, we can draw the following conclusions:

Average Radius \pm Standard Deviation			
Dataset	LS	Huber	Bisquare
60	19.652 \pm 0.167	19.668 \pm 0.166	19.667 \pm 0.166
61	19.669 \pm 0.171	19.684 \pm 0.169	19.683 \pm 0.168
62	19.665 \pm 0.157	19.681 \pm 0.157	19.680 \pm 0.156
63	19.804 \pm 0.353	19.745 \pm 0.230	19.710 \pm 0.211
64	19.897 \pm 0.482	19.827 \pm 0.390	19.788 \pm 0.358
65	19.923 \pm 0.493	19.857 \pm 0.420	19.815 \pm 0.388
66	19.843 \pm 0.348	19.758 \pm 0.247	19.709 \pm 0.206
67	19.872 \pm 0.385	19.784 \pm 0.286	19.739 \pm 0.256
68	19.925 \pm 0.468	19.855 \pm 0.409	19.814 \pm 0.389
69	19.576 \pm 0.147	19.599 \pm 0.147	19.599 \pm 0.147
70	19.903 \pm 0.529	19.835 \pm 0.443	19.794 \pm 0.405

Table 4.2: Estimated average radius and standard deviation values of the reference spheres in datasets 60-70 using the LS, Huber and Bisquare estimators.

1. Among the datasets used for formulating the results reported in this section, the 30-40 datasets are taken from the “vegetative” stage of the Arabidopsis plant growth cycle where only leaf growth can be observed and the 60-70 datasets are taken from the “flowering” stage of the Arabidopsis plant growth cycle. These later images show the stems, leaves and flowers of the plants. From Tables 4.5 and 4.6, it can be seen that the quality of convergence is better in case for the 30-40 datasets than the 60-70 datasets. One of the major reasons may be the quality of scanning performed in the recovery of these range images. Due to the air flow in the lab (uncontrollable during Yang’s experimental measurements), the stems of the Arabidopsis plants moved slightly from view to view during the scanning process (which is extremely undesirable). This movement results in relatively poor performance of the registration process for datasets 60-70, showing comparatively large quality of fit values. In consequence, the stems are poorly merged and in some cases multiple stems are observed instead of a single one.
2. Practically, from these table entries, we are not able to come to any concrete conclusion about the performance of the registration process used here as these parameters are not reported in Zhao or Yang’s theses. As a result, we can not determine whether our performance is better than their procedures or not.
3. However, these reported parameters can be used as an indicator of performance measurement of the registration process in future experiments on the growth measurement of Arabidopsis plants.

Average Residual \pm Standard Deviation			
No. of Dataset	LS	Huber	Bisquare
30	1.504E-03 \pm 5.479E-04	1.518E-03 \pm 5.687E-04	1.533E-03 \pm 5.893E-04
31	1.554E-03 \pm 6.095E-04	1.569E-03 \pm 6.294E-04	1.584E-03 \pm 6.494E-04
32	1.576E-03 \pm 6.334E-04	1.591E-03 \pm 6.530E-04	1.607E-03 \pm 6.738E-04
33	1.476E-03 \pm 4.993E-04	1.489E-03 \pm 5.194E-04	1.504E-03 \pm 5.422E-04
34	1.449E-03 \pm 5.047E-04	1.462E-03 \pm 5.261E-04	1.477E-03 \pm 5.497E-04
35	1.454E-03 \pm 5.102E-04	1.467E-03 \pm 5.310E-04	1.479E-03 \pm 5.514E-04
36	1.683E-03 \pm 1.202E-03	1.724E-03 \pm 1.300E-03	1.884E-03 \pm 1.690E-03
37	1.702E-03 \pm 1.246E-03	1.743E-03 \pm 1.344E-03	1.912E-03 \pm 1.754E-03
38	1.697E-03 \pm 1.251E-03	1.738E-03 \pm 1.349E-03	1.906E-03 \pm 1.756E-03
39	3.226E-03 \pm 4.926E-03	2.883E-03 \pm 4.084E-03	2.909E-03 \pm 4.145E-03
40	2.149E-03 \pm 2.311E-03	2.120E-03 \pm 2.236E-03	2.345E-03 \pm 2.783E-03

Table 4.3: Estimated average residual and standard deviation values of the reference spheres of datasets 30-40 using the LS, Huber and Bisquare estimators.

4.3.3 Performance Analysis of the Plant Growth Measurement

In Yang’s thesis, from 900 original 3D range views, she generated a total of 83 synthesized 3D triangular meshes, each one synthesized from 12 original 3D range views. Based on these 3D triangular meshes, she calculated the areas of plant canopies and the total visible leaf and stem coverage area. However, we generated only 22 synthesized 3D triangular meshes for our experiment, 11 in the vegetative stage of growth and 11 in the flowering stage of growth, as measuring canopy area and volume is not our main thesis goal. Out of 900 original range views, we selected 264 3D range views, 132 representing the “vegetative” stage of growth and the other 132 representing the “flowering” stage of growth to generate 22 synthesized 3D polygon meshes. From these meshes, we measured the canopy 3D surface areas and 3D plant volumes and compared the results with Yang’s results.

4.3.3.1 Changes in Plant Canopy Area

Figures 4.4a, 4.4b, 4.4c, and 4.4d show the 3D triangular meshes of the Arabidopsis plants at four different nights (the 10th night, the 13th night, the 20th night, and the 23rd night) during the 25 days of scans conducted by Yang. We measured the canopy surface areas from the 3D polygonal meshes of the 30-40 and the 60-70 datasets. Furthermore, the area growth rates were calculated using Equation (4.4). Figure 4.5a shows the growth patterns of these plants for the 30-40 datasets, based on canopy surface area and the patterns their growth rates are shown in Figure 4.5b. Figure 4.6a

Average Residual \pm Standard Deviation			
No. of Dataset	LS	Huber	Bisquare
60	1.252E-03 \pm 1.836E-04	1.252E-03 \pm 1.835E-04	1.252E-03 \pm 1.835E-04
61	1.264E-03 \pm 2.070E-04	1.263E-03 \pm 2.070E-04	1.263E-03 \pm 2.070E-04
62	1.258E-03 \pm 2.026E-04	1.258E-03 \pm 2.025E-04	1.258E-03 \pm 2.026E-04
63	1.686E-03 \pm 6.977E-04	1.703E-03 \pm 7.277E-04	1.726E-03 \pm 7.705E-04
64	1.833E-03 \pm 8.659E-04	1.853E-03 \pm 8.911E-04	1.878E-03 \pm 9.256E-04
65	1.919E-03 \pm 9.658E-04	1.939E-03 \pm 9.886E-04	1.967E-03 \pm 1.025E-03
66	1.823E-03 \pm 7.831E-04	1.845E-03 \pm 8.118E-04	1.877E-03 \pm 8.557E-04
67	1.860E-03 \pm 8.296E-04	1.884E-03 \pm 8.561E-04	1.912E-03 \pm 8.888E-04
68	2.061E-03 \pm 1.110E-03	2.082E-03 \pm 1.131E-03	2.109E-03 \pm 1.158E-03
69	5.594E-04 \pm 1.462E-04	5.591E-04 \pm 1.460E-04	5.591E-04 \pm 1.460E-04
70	2.046E-03 \pm 1.189E-03	2.070E-03 \pm 1.226E-03	2.100E-03 \pm 1.275E-03

Table 4.4: Estimated average residual and standard deviation values of the reference spheres for datasets 60-70 for the LS, Huber and Bisquare estimators.

shows the growth patterns of *Arabidopsis* plants for the 60-70 datasets for canopy surface area measurements and the patterns of the area growth rates are shown in Figure 4.6b. The area growth rate is computed as:

$$\text{Area Growth Rate} = \frac{A_2 - A_1}{A_1}, \quad (4.4)$$

where A_1 and A_2 are the areas of a canopy at two consecutive times [15].

In Figures 4.5 and 4.6 we show the growth rates in the canopy at the vegetative stage of growth for the 30-40 datasets and the canopy/stem foliage growth rates for the flowering stage of growth for the 60-70 datasets.

We compared our measured canopy area with Yang's result to compare the performance of the proposed method. Figures 4.7a, 4.7b, 4.7c, and 4.7d graphically represent the comparison of the canopy surface area measurement between the proposed or automated method and Yang's method for the 4 lines of *Arabidopsis thaliana*, 3¹, 10⁴, pBI 121, and wild type, respectively for datasets 30-40. Similarly, Figures 4.8a, 4.8b, 4.8c, and 4.8d graphically represent the comparison of the canopy surface area measurement between the proposed or automated method and Yang's method for the 4 lines of *Arabidopsis thaliana*, 3¹, 10⁴, pBI 121, and wild type, respectively for datasets 60-70.

A detailed discussion of some important points are as follows:

- It is natural that the canopy surface areas of the plants increased as they grew and this was what we observed as seen in Figures 4.5a and 4.6a.

Dataset	Number of Iterations	Average Distance \pm Standard Deviation
30	24	0.441 ± 0.341
31	14	0.432 ± 0.331
32	14	0.417 ± 0.338
33	21	0.405 ± 0.345
34	16	0.415 ± 0.337
35	13	0.424 ± 0.326
36	16	0.438 ± 0.357
37	16	0.439 ± 0.363
38	18	0.422 ± 0.338
39	14	0.446 ± 0.380
40	29	0.484 ± 0.414

Table 4.5: Performance Analysis of the overall registration process based on the average and standard deviation of distance between two points after the completion of the registration process on datasets 30-40

- Based on the transgenic characteristics, the canopy surface areas of the 3¹ and 10⁴ lines are expected to grow faster than those of wild type and pBI 121 (plasmid-only control) type among the Arabidopsis plants. The 3¹ and 10⁴ lines were genetically modified to produce up to 80% more oil than the wild type. This faster growth can be fully observed in Figures 4.5a and 4.6a. As the number of days increases, the canopy areas of the 3¹ and 10⁴ lines were always larger than those of the wild types and pBI 121 (plasmid-only control) type.
- In Figure 4.5b and 4.6b, the negative growth rates that are observed can be explained by changes in leaf sizes as leaves wilt or as the plant respire in the night-time, according to Zhao and Yang. Some of interesting observations regarding Figure 4.5b and 4.6b are as below:
 - i. Among the datasets 60-70, the number of negative peaks are higher than the datasets 30-40. Yang mentioned that the errors in calculating the volumes of plant stems were due to the ShapeGrabber laser scanner's inability to capture tiny objects properly, such as the plant stems, which were about 1 mm in diameter. However, other factors include the uncontrollable air flow in the lab, that caused the stems to jiggle during the scanning process, were also serious problems. This jiggling results in poor alignment during the registration process and multiple stems are observed, instead of a a single merged stem in the 3D polygonal mesh. Moreover, the scanner was unable to properly scan thin stems and this inadequate sampling results in missing stem parts in some of the datasets. Also, we had a hard time distinguishing the soil and the pots in these images. This may also be

Dataset	Number of Iterations	Average Distance \pm Standard Deviation
60	9	0.557 ± 0.489
61	15	0.658 ± 0.596
62	13	0.678 ± 0.620
63	19	0.555 ± 0.503
64	9	0.590 ± 0.543
65	15	0.563 ± 0.511
66	20	0.561 ± 0.511
67	15	0.581 ± 0.530
68	13	0.625 ± 0.574
39	21	0.643 ± 0.585
70	22	0.602 ± 0.596

Table 4.6: Performance Analysis of the overall registration process based on the average and standard deviation of distance between two points after the completion of the registration process on datasets 60-70

another reason for the inconsistency in results for datasets 60-70. Figure 4.9a shows the multiple stems in the 3D polygonal meshes of 61st dataset, which may be a side-effect of the uncontrollable air flow in the lab during the scanning process. Figure 4.9b shows the inadequately sampled stems in the 3D polygonal meshes of 70th dataset due to the scanner’s inability to capture tiny objects properly.

- ii. Again, the manual nature of the editing may also be a reason behind this negative growth rate or inconsistency of the changes of canopy surface area measurement values.
- Yang mentioned in her thesis, that for calibrating data, her areas and volumes are comparatively larger than the original values and the error rate was relatively higher. This was due to the conservative way plant trimming was manually performed. However, our measured areas are relatively smaller than Yang’s results, as can be seen in Figures 4.7a, 4.7b, 4.7c, 4.7d, 4.8a, 4.8b, 4.8c, and 4.8d. We cannot claim our results are more accurate than hers, as we do not have any “gold standard” to make any quantitative comparisons. Also, the manual nature of editing needs to be considered here (although, we followed the exact steps mentioned in Yang’s thesis for editing).

4.3.3.2 Changes in 3D Stem Volume

We measured the 3D volumes of plant stems and foliage volumes from the 3D polygonal meshes using datasets 60-70 only, because datasets 30-40 represent the “vegetative

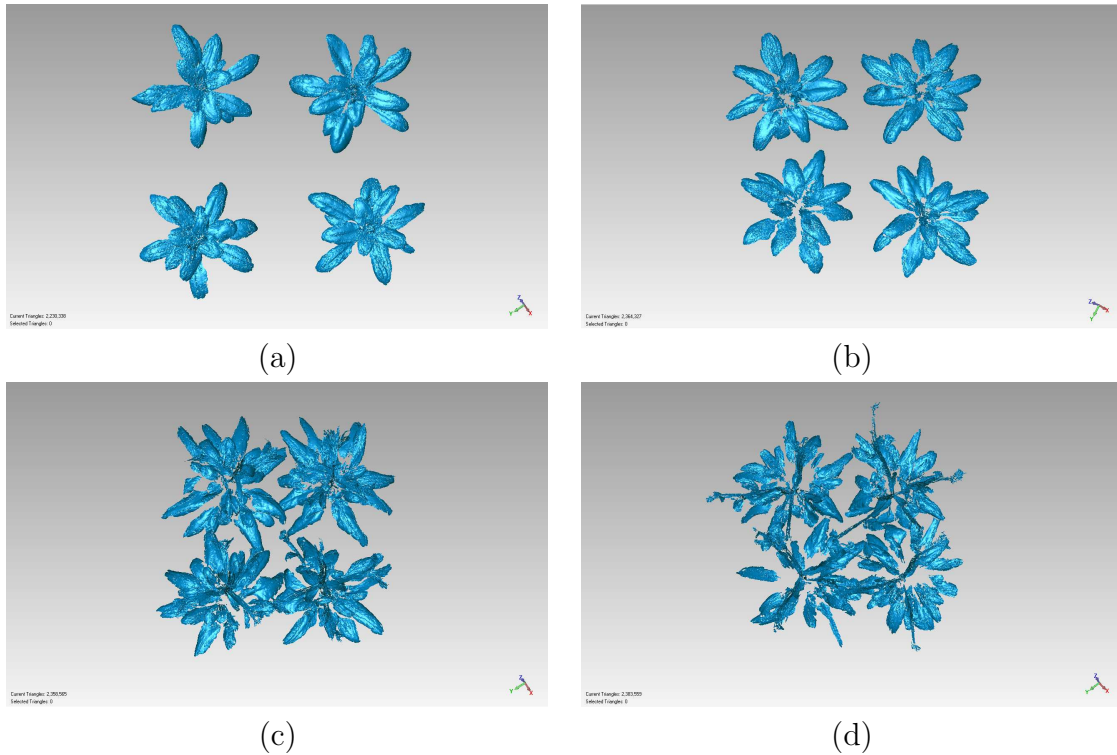


Figure 4.4: 3D triangular meshes of the *Arabidopsis* plants for four different nights during the 25 days of scans conducted by Yang; (a) taken at 20:30 for the 10th night, (b) taken at 02:00 for the 13th night, (c) taken at 20:30 for the 20th night, and (d) taken at 02:00 for the 23rd night.

stage” of *Arabidopsis* plants and do not show any stem growth. To measure 3D stem volume, we used Geomagic’s “Volume to Plane” tool because the plant stems are irregular objects. This measurement fully depends on the position of the plane and distance between the object and the plane. To provide consistency in our measurement, we used the circular table (used during the scanning process) as our reference plane and then placed another offset plane at a specific distance in almost every image. Detail information and parameters to set plane for volume measurement are discussed in Section 3.1.5. These information are very important as the measured values fully depend on them. Furthermore, the volume growth rates are calculated using Equation (4.5) as follows:

$$\text{Volume Growth Rate} = \frac{V_2 - V_1}{V_1}, \quad (4.5)$$

where V_1 and V_2 are the areas of a canopy at two consecutive times [15]. Figure 4.10a shows the growth patterns of the *Arabidopsis* plants, based on 3D stem and foliage volume. Figure 4.10b shows their growth rate.

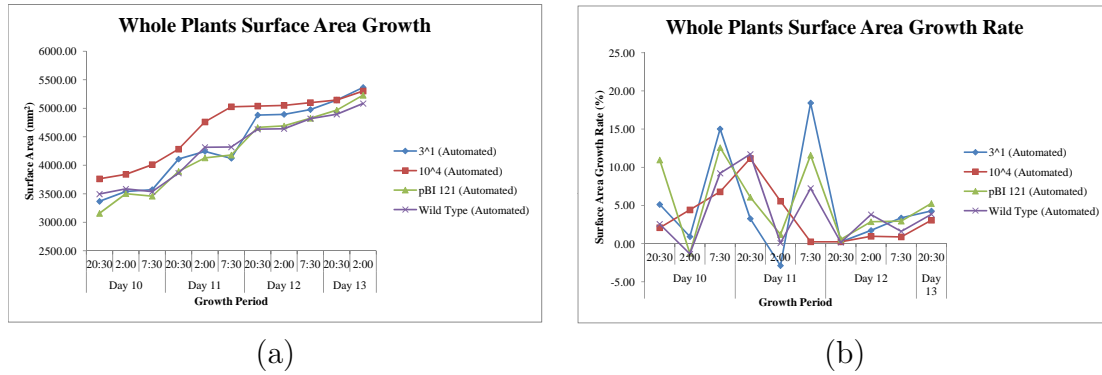


Figure 4.5: Growth patterns of the *Arabidopsis* plants showing the changes in the canopy surface area for datasets 30-40; (a) Growth patterns of the *Arabidopsis* plants showing the changes in the canopy surface area and (b) the patterns of their area growth rate.

We compared our measured 3D stem volumes with those of Yang. However, this comparison is not entirely valid as we had no information regarding Yang's positioning of the plane before measuring stem volume. Figures 4.11a, 4.11b, 4.11c, and 4.11d graphically represent the comparison of the 3D stem volume measurements between the automatic and manual methods for the 4 lines of *Arabidopsis thaliana*, 3^1 , 10^4 , pBI 121, and wild type, respectively for datasets 60-70.

A detailed discussion of the experimental results are as follows:

- The natural incremental volume changes of stems over time is observed from Figures 4.10a, with some minor exceptions. These exceptions are possibly due to the contribution of several factors, including scanner's inability to capture tiny objects, the uncontrolled air flow in the lab. that jiggered the stems during the scanning process, resulting in a poor alignment, missed stem area due to inadequately scanned data in some datasets, and difficulties in segmenting the soil and the pots from the actual plants.
- Although the transgenic characteristics of these plants indicate that the growth of 3^1 and 10^4 lines should be faster than those of wild type and pBI 121 (plasmid-only control) type of the *Arabidopsis* plants, this is not fully exhibited in Figure 4.10b. Inconsistency is observed here, which again can be due to the side-effects of the aforementioned reasons. The 3D stem volume growth rate for wild type and pBI 121 lines were relatively more consistent than 3^1 and 10^4 growth rates. 3^1 showed the highest growth rate. However, instead of 10^4 , the growth rate of pBI 121 was the second best. Of course, it should be noted that a plant's overall growth can not be measured from its stem growth only. Finally, the Wild type *Arabidopsis* plants showed very slow stem growth rate.

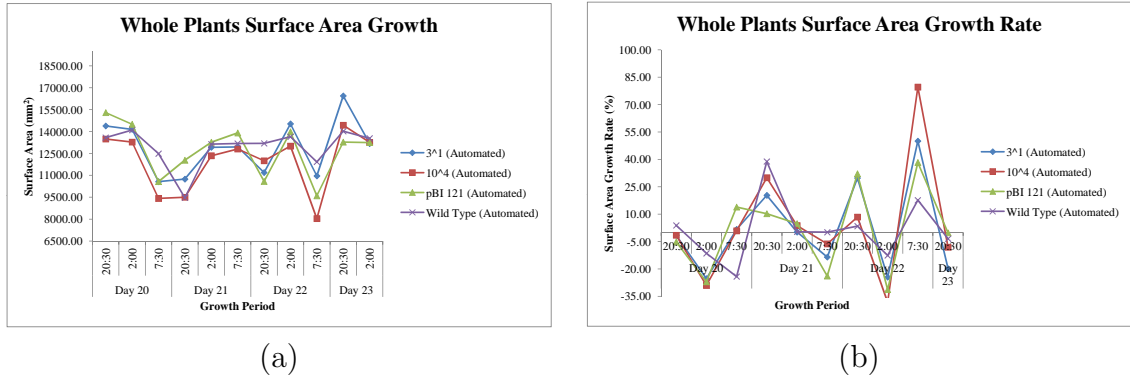


Figure 4.6: Growth patterns of the *Arabidopsis* plants showing the changes in the canopy surface area for datasets 60-70; (a) Growth patterns of the *Arabidopsis* plants showing the changes in the canopy surface area and (b) the patterns of their area growth rate

- Our measured volumes are greater than Yang’s results. as shown in Figures 4.11a, 4.11b, 4.11c and 4.11d. These large values can be due to:
 - i. Incompatibility of the position of the plane. For example, for a similar object, the volumes are $1.358e5$, $6.111e4$, and $1.735e5$ if we position the offset plane 90 mm, 120 mm, and 50 mm respectively above the reference plane.
 - ii. From some of the stem images in the thesis, it looks like Yang only used the principle structure (no leaves or vegetative branches) but we included leaves with the stem (foliage), vegetative branches and leaves attached to it, and also the auxiliary and terminal buds while measuring stem growth. Figures 4.12a and 4.12 show the pre-processed stems used by Yang and us, respectively.

4.4 Conclusion

The experimental outcomes related to the sphere fitting algorithms show that the implemented algorithms (LS and M-estimators) provide good fitting, which is essential for achieving better convergence during the registration process. However, due to the manual nature of the growth measuring procedures, it is obvious that errors are introduced during the measurement of the plant data. For instance, while measuring plant growth via area and volume measurement from the synthesized 3D triangular meshes, trimming the extraneous elements (i.e. the table, pots and soil) in the 3D range images may have caused significant problems as it was done manually. This

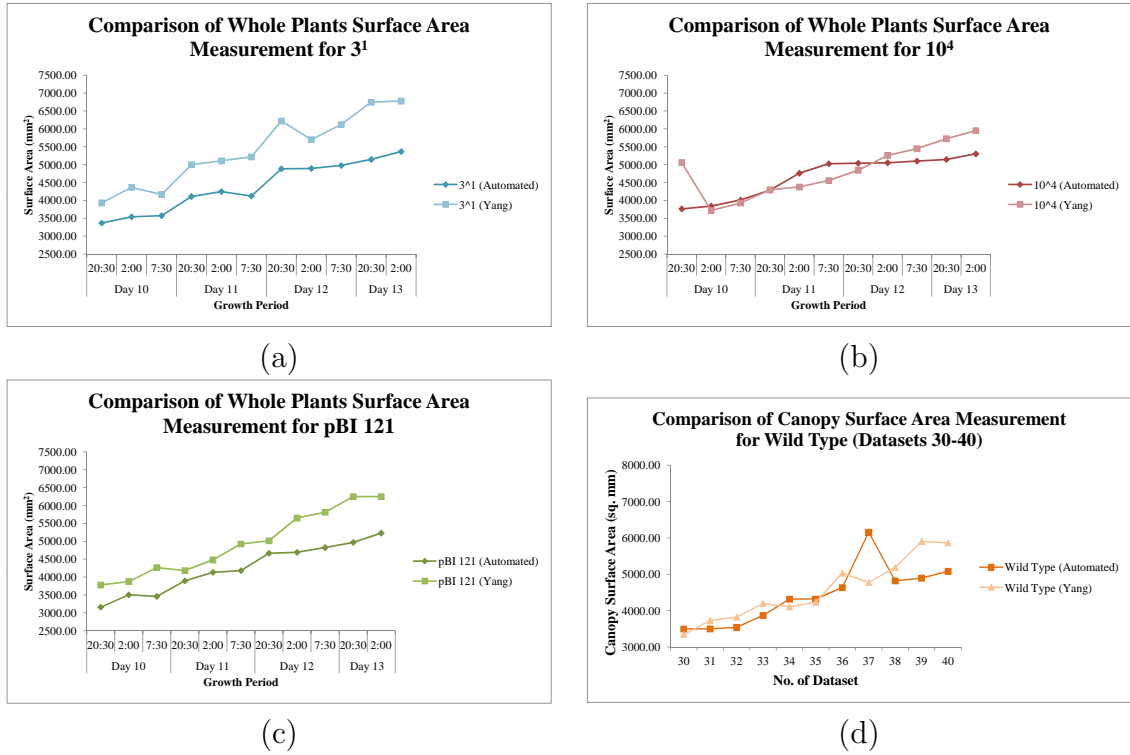


Figure 4.7: Graphical representation of the comparison of canopy surface area measurement between the proposed (automated) method and Yang's method for datasets 30-40; (a) for 3^1 , (b) for 10^4 , (c) for pBI 121, and for wild type

is because it is hard to clearly identify and separate the leaves and their affiliated components. Despite the errors in our experimental measurements (even, the lack of proper “gold standard” for validation), the presented growth patterns strongly support the approach of using 3D imaging technology to measure plant growth and provided more detailed and continuous growth data beyond the traditional destructive growth measurement methods.

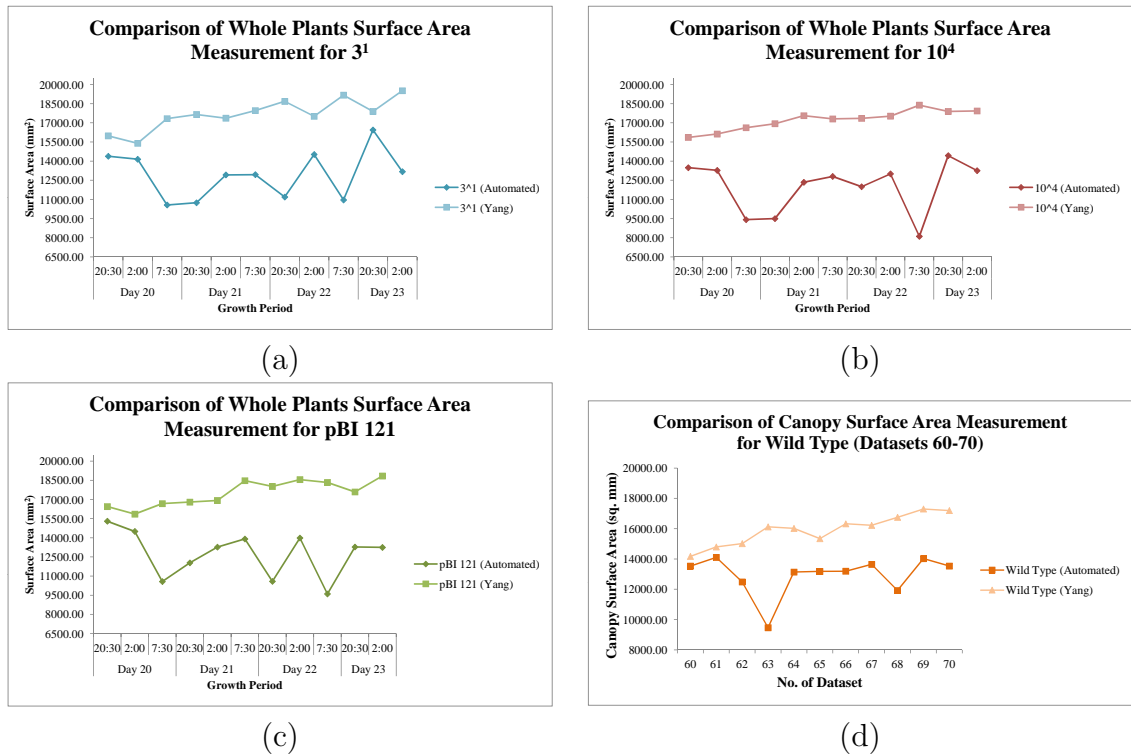


Figure 4.8: Graphical representation of the comparison of canopy surface area measurement between the proposed (automated) method and Yang's method for datasets 60-70; (a) for 3^1 , (b) for 10^4 , (c) for pBI 121, and for wild type

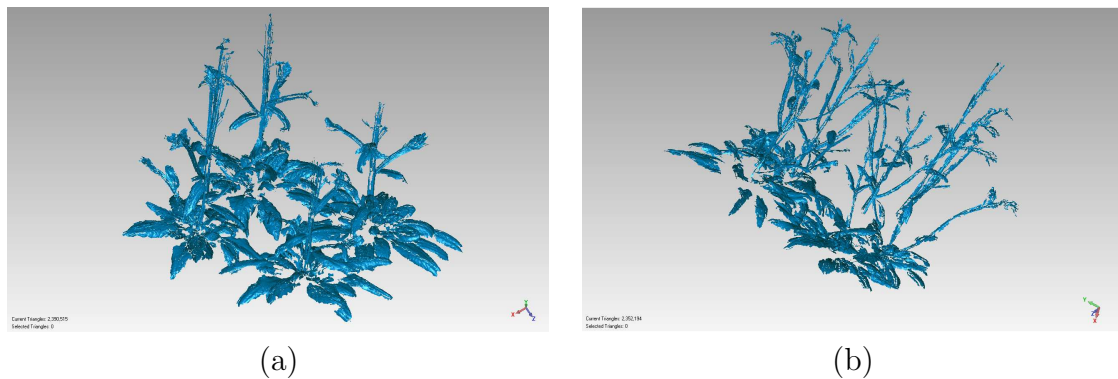


Figure 4.9: Pictorial explanation of the negative peaks in the growth rate of canopy surface area among the datasets 60-70; (a) Multiple stems in the 3D polygonal meshes of 61st dataset which may be a side-effect of the uncontrolled air flow in the lab during the scanning process and (b) Inadequately sampled stems in the 3D polygonal meshes of 70th dataset due to the scanner's inability to capture tiny objects properly.

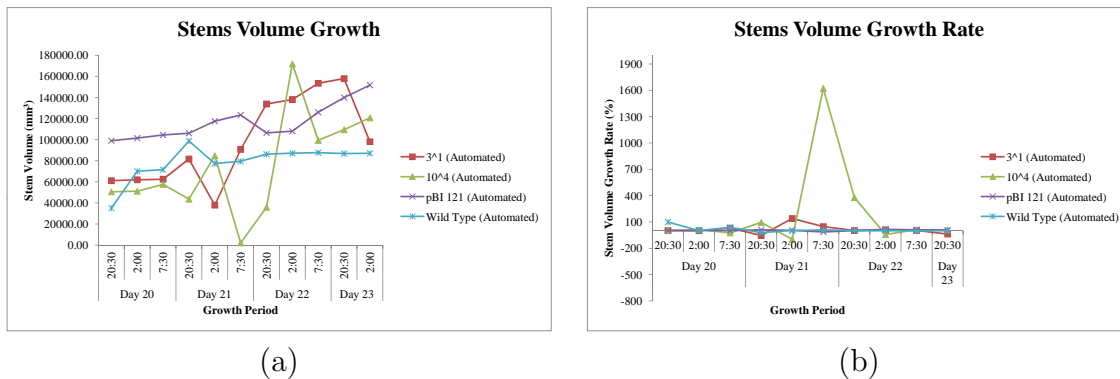


Figure 4.10: Growth patterns of the Arabidopsis plants showing the changes in the 3D stem volume for datasets 60-70; (a) Growth patterns of the Arabidopsis plants showing the changes in the 3D stem volume and (b) the patterns of their stem volume growth rate

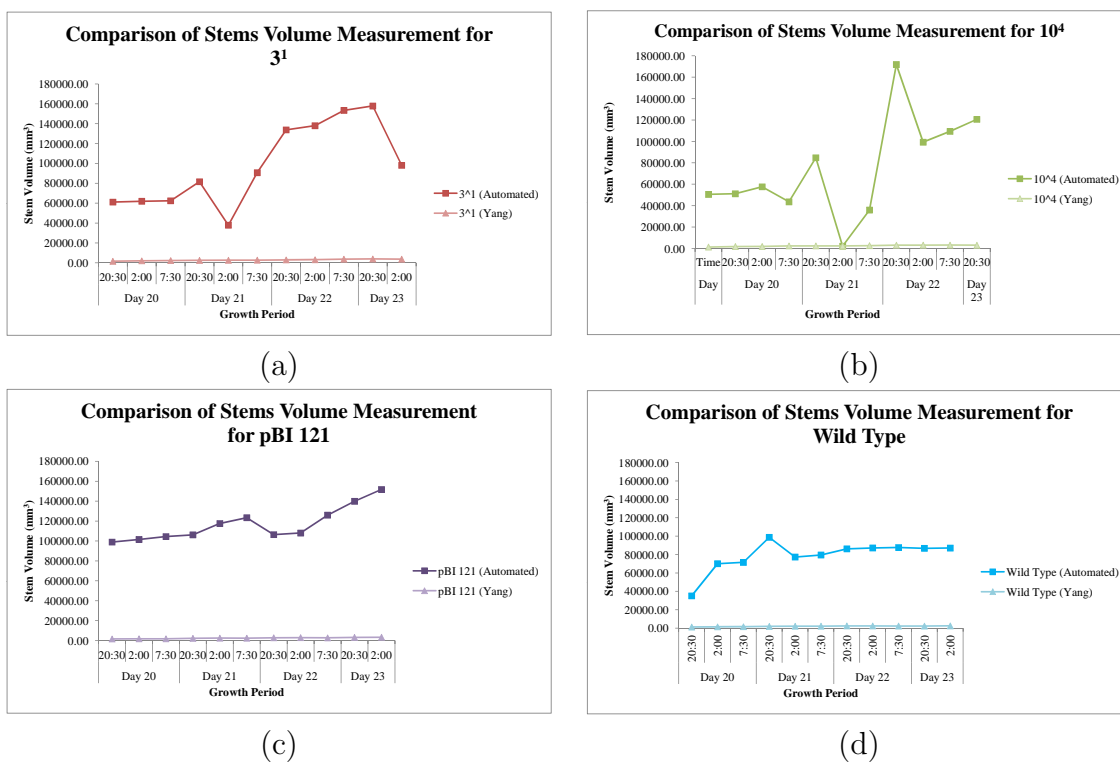


Figure 4.11: Graphical representation of the comparison of canopy surface area measurement between the proposed (automated) method and Yang's manual method for datasets 60-70; (a) for 3¹, (b) for 10⁴, (c) for pBI 121 and (d) for wild type.

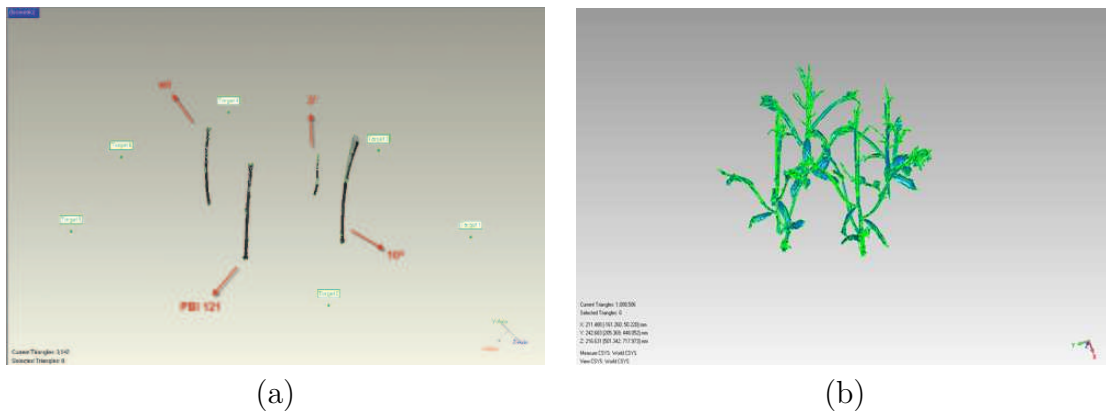


Figure 4.12: Difference between Yang and our automatic pre-processed stem used in measuring 3D stem volume for dataset 70; (a) Yang's pre-processed stem before measuring 3D stem volume and (b) our pre-processed stem before measuring 3D stem volume

Chapter 5

Conclusion and Future Work

5.1 Summary

In this thesis, we automated the manual registration process used by Zhao [15] and Yang [16] during their attempts to measure the growth of *Arabidopsis thaliana* plants quantitatively using Geomagic Studio. We ran our experiments based using Yang’s *Arabidopsis* datasets. Yang used the SG1002 ShapeGrabber range scanner to generate the 3D scanned images of the plant(s) and Geomagic Studio CAD software to merge these scans into 3D polygonal meshes. Then, from these polygonal meshes, 3D areas and 3D volumes were computed to determine the plant’s growth over a time cycle. To perform the registration (merging) process in Geomagic, 6 ping pong balls were used as reference spheres during the scanning process. But these reference spheres were imaged as semi-spheres in the original range images because the laser scanner can only see the visible parts of an object. However, without full spheres, Geomagic is unable to perform the registration of the adjacent images. Therefore, Zhao and Yang manually replaced these semi-spheres with artificially generated spheres using the Geomagic software. One of the major contributions of this research is to automatically detect and localize the semi-spheres in the original range images using parameter estimation techniques, generate synthetic spheres using the estimated parameter values and the parametric equations of spheres, and finally to reconstruct each range view by automatically replacing the semi-spheres with the “perfect” full sphere data. After the pre-processing, the registration is accomplished automatically using macros in Geomagic on these modified range data so that the merged data can be used to quantitatively measure plant growth (see Appendix G).

In Chapter 1, we briefly outlined the problems tackled by this thesis, followed by a detail discussion in Section 1.1 that include the tedious, manual and error-prone registration process used by Zhao and Yang, the incompleteness of 3D range data, especially the often poorly sampled reference spheres. These problems made the

automation of the registration process using Geomagic Studio 12 difficult. The motivation (see Section 1.2) to design and develop a fully automated and self-sustained registration process to provide an automatic and more accurate tool for the plant growth measurement process. The main contributions of this thesis were also summarized here in Section 1.3). Among the contributions listed include the detection and estimation of the locations of semi-spheres inside the range images using parameter estimation techniques, the generation and replacement of full sphere with semi-sphere data using the estimated parameter values and the parametric equations of spheres, and finally, the automation of the overall registration process providing speed and accuracy.

Chapter 2 provides a general overview of the various parameter estimation techniques widely used in Image Processing and Computer Vision. Some of these techniques were used to detect the location of semi-spheres in the range images and to replace these incomplete data with full sphere to aid the automation of the registration process. Two major categories of parameter estimation techniques, namely, LS (Section 2.2.1) methods and robust estimation techniques (Section 2.2.2), and their sub-categories are discussed here. However, this chapter also reviews some of the recent literature, especially, Keightley and Bawden [46] and Seidel *et al.* [47], on quantitative plant growth measurement using 3D imaging technology (Section 2.3).

In chapter 3, we explained the pre-processing methods applied on each view of the raw range view images, so that Geomagic Studio 12 can automatically create synthesized 3D polygon meshes from them and then measure the 3D areas and 3D volumes from the merged images of the Arabidopsis plant. The proposed methodology included several steps, i.e. segmentation of the semi-spheres both manually and automatically, estimation of the parameters, the center coordinates and radius of the reference spheres, using LS and M-estimators to estimate the sphere parameters and perform a segmentation of the measured semi-sphere data from plant data, replacement of semi-spheres with full sphere data in the original range images, reconstruction of each view, and finally, the registration of these views to create 3D polygon meshes to aid the plant growth measurement process. In Section 3.1.5.1, pre-processing of these 3D polygon meshes are outlined so the plant's surface area and 3D volume could be measured from them to estimate the growth over a period of time.

Chapter 4 discusses the various problems of the Arabidopsis plant datasets used in this thesis. These problems include the missing datasets and the absence of "gold standard" to verify the experimental outcomes (see Section 4.1). We also outlined the various methods used to validate the results in Section 4.2 followed by the experimental results and discussion (see Section 4.3). Results showed that the parameter estimation techniques performed well. Although, plant growth measurement was not our primary goal, we presented results to show the growth pattern of the Arabidopsis plants in this chapter. However, the quantitative analysis of plant growth showed that some errors were introduced in our calculations. However, despite these calculation

errors, the presented growth patterns strongly support the approach of using 3D imaging technology to measure plant growth and provide more detailed and continuous growth data beyond the traditional destructive growth measurement methods.

Despite of the errors in the calculation of plant growth measurement, we successfully designed and developed a fully automated and self-sustained registration process using macros in Geomagic to provide an automatic and more accurate tool to aid plant growth measurement process.

5.2 Future Work

On the basis of our experiments, we believe that future work should focus on the following issues:

- **Automatic Range Segmentation:** Although we have already automated the overall registration process, a significant amount of time is still needed to edit the 3D range images. Manual editing of 3D range images is essential to remove the extraneous elements before measuring the plant growth (surface area and 3D volume). Moreover, the manual editing of the 3D triangular meshes significantly affects the accuracy of the surface area and the 3D volume measurements, a system with more accurate and automatic editing functions is needed to be developed which will reduce the unnecessary errors involved in Section and as well as the time required.
- **“Gold Standard” for Validation:** We do not have any “gold standard to validate the performance of the registration process which is an essential part of plant growth measurement. Therefore, during the next experimental setup, steps should be taken to measure the plants using traditional “destructive” or “wet volume” methods after they have been scanned by the range sensor..
- **Re-scanning to Generate Better Datasets:** The whole scanning should be re-done to generate better quality 3D range images. The datasets of the Arabidopsis plants used in our thesis are generate using ShapeGrabber SG1002 scanner. However, this scanner is not able to clearly capture the target objects under bright visible light as its red laser beam is 660 nm, which is in the visible spectrum. Moreover, the scanning environment should be highly controlled. To improve the quality of the range images the following steps can be considered:
 - Instead of using such scanners, infrared laser scanners can be used. Infrared light is electromagnetic radiation with a wavelength longer than that of visible light, measured from the near infrared laser beam at 825 nm (not visible to the human eye and, more importantly, having no effect on plant growth)

- To reduce the editing before growth measurement, the visibility of the extraneous elements (i.e. the soil, the pots and the table) can be minimized during the scanning phase. To do so, soil, pots and the table could be covered using black paper or black plastic bag or even more removed from the image via depth segmentation.
 - Prevention steps should be taken so that the stems of the plants do not move unless this motion is caused by natural cause (i.e. plants' natural growth and due to the increasing weight of the plants' body). The plant motion caused by wind in the experimental growth chamber needs to be eliminated during the experimental measurements.
 - During the experimental measurements, the sphere targets were also seem to be moving or they were bumped at some point. To achieve better alignment in the registration phase, it is better not to move the plants as well as the sphere targets once experimental measurements begin. Also, the reference spheres can be arranged in a slightly less symmetric pattern (i.e. varying the height and the distance between two adjacent targets).
 - The scanner should always remain in a static position through out the experiment. As we are experimenting with growing plants, increasing height may not be anticipated beforehand. To be in the safe side, a reasonable distance should be maintained so that plant's body does not exceed the scanners line-of-sight (which may result in the change of scanner's or table's position). The change in position during the scanning process is not at all desirable as this will directly affect volume measurement ("Compute Volume To Plane" is extremely sensitive to the position of the reference plane).
- **Retaining Automation in Geomagic:** There are some issues that need to be cared of for retaining automation in Geomagic using macros.
 - i. Two of the Geomagic's tools "Detect Sphere Targets" and "Target Registration" used in this thesis are manual operations. They are very sensitive to the curvature in the model and need a controlled environment and therefore proper measures (e.g., sphere targets should be properly imaged but not extremely dense) should be taken so that automation is guaranteed all the time.
 - ii . "Target Cleanup" can act differently than what is expected during the use of the macros. Targets may not exactly overlap each other during registration and can result in larger sphere in the merged image. As the radius of the target is now changed in the merged image, "Target Cleanup" needs to know the exact radius to remove the targets properly. Radius needs to be picked carefully so that the close non-sphere elements (e.g., stems and leaves) are not affected at the same time the target is removed

perfectly. In our case, we had to clean the spheres manually at some points. However, “Global Registration” can be performed without removing the targets but will result in relatively less accuracy.

- iii. We had to record the experimental results of the areas and volumes manually from Geomagic as these tools do not have any automatic functionalities yet.

In this chapter, we summarized the main contributions of our thesis. We conclude the chapter with some suggestions for future work.

We would like to leave the reader with the news that most of our suggestions for future work have been met or exhibited by a new growth chamber build on the 4th floor on the North Campus building. In this chamber, the wind can be turned off during experimental measurements. A 7 degrees-of-freedom robot arm has a SG1002 ShapeGrabber scanner as its payload. Now a plant (maybe an Arabidopsis plant) can be placed on a table, and be scanned by the moving scanner (it can be stopped at controlled positions for scanning) allowing not only side views of the plant but top and bottom (views under and well as above leaves). This equipment was purchased by a CFI grant awarded in 2009 and the lab is in a close to final state now. We expect to measure significantly better range data with this equipment.

Appendix A

Average and Standard Deviation of Average Radius (Datasets: 30-40)

Radius \pm Standard Deviation			
No. of View	LS	Huber	Bisquare
View 01	19.999 \pm 0.370	19.878 \pm 0.231	19.834 \pm 0.187
View 02	20.123 \pm 0.509	19.990 \pm 0.356	19.924 \pm 0.279
View 03	19.789 \pm 0.378	19.754 \pm 0.273	19.735 \pm 0.235
View 04	19.822 \pm 0.431	19.733 \pm 0.317	19.694 \pm 0.276
View 05	19.733 \pm 0.356	19.676 \pm 0.242	19.648 \pm 0.207
View 06	19.684 \pm 0.388	19.643 \pm 0.264	19.622 \pm 0.221
View 07	19.566 \pm 0.167	19.570 \pm 0.138	19.566 \pm 0.129
View 08	19.580 \pm 0.151	19.595 \pm 0.151	19.594 \pm 0.150
View 09	19.627 \pm 0.216	19.615 \pm 0.179	19.608 \pm 0.170
View 10	19.751 \pm 0.410	19.712 \pm 0.301	19.696 \pm 0.272
View 11	19.971 \pm 0.419	19.851 \pm 0.269	19.797 \pm 0.212
View 12	20.017 \pm 0.392	19.873 \pm 0.245	19.810 \pm 0.196

Table A.1: Average and standard deviation of average radius (mm) for dataset 30 obtained from LS, Huber and Bisquare estimators

Radius \pm Standard Deviation			
No. of View	LS	Huber	Bisquare
View 01	20.030 \pm 0.397	19.914 \pm 0.259	19.871 \pm 0.215
View 02	20.200 \pm 0.629	20.107 \pm 0.575	20.056 \pm 0.537
View 03	19.819 \pm 0.374	19.773 \pm 0.267	19.750 \pm 0.228
View 04	19.812 \pm 0.443	19.739 \pm 0.323	19.705 \pm 0.279
View 05	19.738 \pm 0.364	19.689 \pm 0.240	19.661 \pm 0.204
View 06	19.688 \pm 0.383	19.652 \pm 0.261	19.633 \pm 0.220
View 07	19.573 \pm 0.159	19.579 \pm 0.134	19.575 \pm 0.125
View 08	19.593 \pm 0.158	19.607 \pm 0.157	19.606 \pm 0.155
View 09	19.650 \pm 0.264	19.636 \pm 0.204	19.626 \pm 0.185
View 10	19.782 \pm 0.446	19.738 \pm 0.332	19.719 \pm 0.298
View 11	20.010 \pm 0.441	19.873 \pm 0.280	19.811 \pm 0.217
View 12	20.055 \pm 0.429	19.903 \pm 0.255	19.835 \pm 0.193

Table A.2: Average and standard deviation of average radius (mm) for dataset 31 obtained from LS, Huber and Bisquare estimators

Radius \pm Standard Deviation			
No. of View	LS	Huber	Bisquare
View 1	20.044 \pm 0.417	19.928 \pm 0.277	19.884 \pm 0.232
View 2	20.238 \pm 0.704	20.162 \pm 0.702	20.113 \pm 0.669
View 3	19.830 \pm 0.372	19.780 \pm 0.267	19.754 \pm 0.230
View 4	19.833 \pm 0.426	19.747 \pm 0.314	19.708 \pm 0.273
View 5	19.739 \pm 0.367	19.691 \pm 0.240	19.663 \pm 0.205
View 6	19.687 \pm 0.380	19.651 \pm 0.259	19.633 \pm 0.219
View 7	19.574 \pm 0.156	19.581 \pm 0.133	19.577 \pm 0.126
View 8	19.597 \pm 0.160	19.611 \pm 0.159	19.609 \pm 0.156
View 9	19.660 \pm 0.277	19.642 \pm 0.211	19.631 \pm 0.190
View 10	19.797 \pm 0.468	19.749 \pm 0.348	19.729 \pm 0.310
View 11	20.010 \pm 0.444	19.872 \pm 0.281	19.809 \pm 0.215
View 12	20.069 \pm 0.438	19.910 \pm 0.2574	19.833 \pm 0.195

Table A.3: Average and standard deviation of average radius (mm) for dataset 32 obtained from LS, Huber and Bisquare estimators

Radius \pm Standard Deviation			
No. of View	LS	Huber	Bisquare
View 1	19.932 \pm 0.333	19.814 \pm 0.233	19.762 \pm 0.222
View 2	20.065 \pm 0.426	19.904 \pm 0.238	19.820 \pm 0.183
View 3	19.780 \pm 0.386	19.750 \pm 0.276	19.731 \pm 0.237
View 4	19.789 \pm 0.442	19.722 \pm 0.320	19.689 \pm 0.276
View 5	19.784 \pm 0.350	19.705 \pm 0.242	19.670 \pm 0.208
View 6	19.680 \pm 0.371	19.638 \pm 0.252	19.616 \pm 0.211
View 7	19.565 \pm 0.154	19.572 \pm 0.135	19.569 \pm 0.128
View 8	19.578 \pm 0.154	19.594 \pm 0.155	19.594 \pm 0.155
View 9	19.591 \pm 0.163	19.601 \pm 0.154	19.599 \pm 0.151
View 10	19.728 \pm 0.341	19.674 \pm 0.214	19.647 \pm 0.167
View 11	19.959 \pm 0.408	19.840 \pm 0.260	19.787 \pm 0.203
View 12	19.980 \pm 0.387	19.855 \pm 0.249	19.801 \pm 0.201

Table A.4: Average and standard deviation of average radius (mm) for dataset 33 obtained from LS, Huber and Bisquare estimators

Radius \pm Standard Deviation			
No. of View	LS	Huber	Bisquare
View 1	19.972 \pm 0.352	19.848 \pm 0.229	19.793 \pm 0.202
View 2	20.104 \pm 0.471	19.941 \pm 0.270	19.858 \pm 0.185
View 3	19.789 \pm 0.394	19.756 \pm 0.281	19.736 \pm 0.239
View 4	19.823 \pm 0.444	19.739 \pm 0.321	19.700 \pm 0.275
View 5	19.760 \pm 0.367	19.692 \pm 0.242	19.660 \pm 0.204
View 6	19.685 \pm 0.387	19.645 \pm 0.259	19.624 \pm 0.214
View 7	19.582 \pm 0.191	19.578 \pm 0.146	19.571 \pm 0.132
View 8	19.585 \pm 0.148	19.601 \pm 0.149	19.601 \pm 0.150
View 9	19.602 \pm 0.173	19.609 \pm 0.158	19.606 \pm 0.152
View 10	19.730 \pm 0.335	19.688 \pm 0.227	19.668 \pm 0.192
View 11	19.940 \pm 0.399	19.840 \pm 0.259	19.795 \pm 0.207
View 12	19.924 \pm 0.391	19.839 \pm 0.252	19.801 \pm 0.201

Table A.5: Average and standard deviation of average radius (mm) for dataset 34 obtained from LS, Huber and Bisquare estimators

Radius \pm Standard Deviation			
No. of View	LS	Huber	Bisquare
View 1	19.971 \pm 0.354	19.858 \pm 0.229	19.815 \pm 0.187
View 2	20.160 \pm 0.559	20.015 \pm 0.390	19.955 \pm 0.326
View 3	19.797 \pm 0.393	19.760 \pm 0.282	19.739 \pm 0.241
View 4	19.831 \pm 0.448	19.744 \pm 0.324	19.704 \pm 0.277
View 5	19.764 \pm 0.369	19.693 \pm 0.244	19.660 \pm 0.205
View 6	19.685 \pm 0.386	19.647 \pm 0.260	19.627 \pm 0.216
View 7	19.585 \pm 0.200	19.579 \pm 0.149	19.571 \pm 0.132
View 8	19.585 \pm 0.147	19.601 \pm 0.148	19.601 \pm 0.149
View 9	19.609 \pm 0.175	19.612 \pm 0.158	19.609 \pm 0.153
View 10	19.737 \pm 0.342	19.699 \pm 0.245	19.684 \pm 0.221
View 11	19.940 \pm 0.401	19.844 \pm 0.260	19.799 \pm 0.209
View 12	19.925 \pm 0.398	19.843 \pm 0.254	19.806 \pm 0.200

Table A.6: Average and standard deviation of average radius (mm) for dataset 35 obtained from LS, Huber and Bisquare estimators

Radius \pm Standard Deviation			
No. of View	LS	Huber	Bisquare
View 1	19.988 \pm 0.239	19.914 \pm 0.306	19.865 \pm 0.239
View 2	19.949 \pm 0.229	19.885 \pm 0.255	19.866 \pm 0.229
View 3	19.748 \pm 0.268	19.715 \pm 0.302	19.697 \pm 0.268
View 4	19.795 \pm 0.382	19.736 \pm 0.472	19.695 \pm 0.382
View 5	19.897 \pm 0.228	19.749 \pm 0.372	19.659 \pm 0.228
View 6	19.709 \pm 0.274	19.662 \pm 0.326	19.638 \pm 0.274
View 7	19.667 \pm 0.190	19.614 \pm 0.230	19.591 \pm 0.190
View 8	19.620 \pm 0.199	19.635 \pm 0.199	19.635 \pm 0.199
View 9	19.649 \pm 0.198	19.593 \pm 0.263	19.559 \pm 0.198
View 10	20.001 \pm 0.338	19.847 \pm 0.802	19.656 \pm 0.338
View 11	20.218 \pm 0.130	20.122 \pm 1.187	19.683 \pm 0.130
View 12	20.178 \pm 0.139	20.033 \pm 0.670	19.748 \pm 0.139

Table A.7: Average and standard deviation of average radius (mm) for dataset 36 obtained from LS, Huber and Bisquare estimators

Radius \pm Standard Deviation			
No. of View	LS	Huber	Bisquare
View 1	19.899 \pm 0.479	19.941 \pm 0.330	19.899 \pm 0.262
View 2	19.906 \pm 0.368	19.929 \pm 0.272	19.906 \pm 0.246
View 3	19.716 \pm 0.444	19.737 \pm 0.325	19.716 \pm 0.282
View 4	19.705 \pm 0.654	19.748 \pm 0.477	19.705 \pm 0.383
View 5	19.671 \pm 0.707	19.768 \pm 0.381	19.671 \pm 0.224
View 6	19.644 \pm 0.475	19.669 \pm 0.323	19.644 \pm 0.266
View 7	19.595 \pm 0.396	19.622 \pm 0.234	19.595 \pm 0.187
View 8	19.645 \pm 0.203	19.645 \pm 0.202	19.645 \pm 0.202
View 9	19.569 \pm 0.402	19.604 \pm 0.270	19.569 \pm 0.198
View 10	19.673 \pm 1.225	19.870 \pm 0.842	19.673 \pm 0.362
View 11	19.697 \pm 1.465	20.146 \pm 1.199	19.697 \pm 0.131
View 12	19.760 \pm 1.059	20.057 \pm 0.698	19.760 \pm 0.146

Table A.8: Average and standard deviation of average radius (mm) for dataset 37 obtained from LS, Huber and Bisquare estimators

Radius \pm Standard Deviation			
No. of View	LS	Huber	Bisquare
View 1	20.019 \pm 0.487	19.950 \pm 0.341	19.911 \pm 0.275
View 2	20.018 \pm 0.379	19.961 \pm 0.296	19.935 \pm 0.269
View 3	19.773 \pm 0.440	19.739 \pm 0.323	19.718 \pm 0.281
View 4	19.817 \pm 0.655	19.755 \pm 0.479	19.712 \pm 0.386
View 5	19.924 \pm 0.703	19.768 \pm 0.377	19.672 \pm 0.219
View 6	19.722 \pm 0.471	19.673 \pm 0.320	19.648 \pm 0.264
View 7	19.674 \pm 0.373	19.622 \pm 0.228	19.597 \pm 0.186
View 8	19.631 \pm 0.202	19.646 \pm 0.201	19.645 \pm 0.201
View 9	19.649 \pm 0.403	19.606 \pm 0.272	19.572 \pm 0.200
View 10	20.011 \pm 1.220	19.874 \pm 0.848	19.678 \pm 0.371
View 11	20.237 \pm 1.472	20.143 \pm 1.203	19.695 \pm 0.129
View 12	20.188 \pm 1.057	20.044 \pm 0.683	19.756 \pm 0.143

Table A.9: Average and standard deviation of average radius (mm) for dataset 38 obtained from LS, Huber and Bisquare estimators

Radius \pm Standard Deviation			
No. of View	LS	Huber	Bisquare
View 1	21.368 \pm 3.760	22.792 \pm 7.251	22.782 \pm 7.231
View 2	20.708 \pm 1.877	31.260 \pm 27.854	31.255 \pm 27.894
View 3	19.767 \pm 0.414	19.723 \pm 0.311	19.703 \pm 0.273
View 4	19.815 \pm 0.634	19.756 \pm 0.462	19.715 \pm 0.373
View 5	19.909 \pm 0.704	19.758 \pm 0.382	19.663 \pm 0.231
View 6	19.721 \pm 0.482	19.672 \pm 0.332	19.647 \pm 0.277
View 7	19.641 \pm 0.399	19.584 \pm 0.242	19.558 \pm 0.195
View 8	19.540 \pm 0.240	19.591 \pm 0.202	19.591 \pm 0.203
View 9	19.074 \pm 1.058	19.513 \pm 0.138	19.471 \pm 0.123
View 10	19.801 \pm 0.703	21.570 \pm 5.031	21.569 \pm 5.038
View 11	20.018 \pm 0.987	21.005 \pm 3.362	21.010 \pm 3.366
View 12	20.377 \pm 1.539	21.770 \pm 4.921	21.781 \pm 4.952

Table A.10: Average and standard deviation of average radius (mm) for dataset 39 obtained from LS, Huber and Bisquare estimators

Radius \pm Standard Deviation			
No. of View	LS	Huber	Bisquare
View 1	21.286 \pm 3.547	22.200 \pm 5.794	22.137 \pm 5.646
View 2	22.282 \pm 5.631	26.671 \pm 16.554	26.648 \pm 16.561
View 3	19.791 \pm 0.448	19.754 \pm 0.326	19.732 \pm 0.281
View 4	19.834 \pm 0.659	19.773 \pm 0.484	19.731 \pm 0.391
View 5	19.933 \pm 0.750	19.774 \pm 0.409	19.664 \pm 0.224
View 6	19.735 \pm 0.499	19.686 \pm 0.346	19.661 \pm 0.290
View 7	19.647 \pm 0.442	19.581 \pm 0.263	19.550 \pm 0.204
View 8	19.566 \pm 0.234	19.596 \pm 0.219	19.596 \pm 0.220
View 9	19.660 \pm 0.451	19.596 \pm 0.283	19.544 \pm 0.178
View 10	20.016 \pm 1.286	19.952 \pm 1.088	19.681 \pm 0.428
View 11	20.263 \pm 1.565	20.182 \pm 1.333	19.679 \pm 0.122
View 12	20.232 \pm 1.175	20.090 \pm 0.809	19.751 \pm 0.138

Table A.11: Average and standard deviation of average radius (mm) for dataset 40 obtained from LS, Huber and Bisquare estimators

Appendix B

Average and Standard Deviation of Average Residual (Datasets: 30-40)

Average Residual \pm Standard Deviation			
No. of View	LS	Huber	Bisquare
View 1	1.586E-03 \pm 6.552E-04	1.609E-03 \pm 6.828E-04	1.630E-03 \pm 7.075E-04
View 2	1.964E-03 \pm 1.151E-03	2.000E-03 \pm 1.194E-03	2.034E-03 \pm 1.233E-03
View 3	1.395E-03 \pm 5.517E-04	1.403E-03 \pm 5.728E-04	1.413E-03 \pm 5.952E-04
View 4	1.604E-03 \pm 6.467E-04	1.620E-03 \pm 6.703E-04	1.637E-03 \pm 6.960E-04
View 5	1.535E-03 \pm 5.558E-04	1.546E-03 \pm 5.734E-04	1.557E-03 \pm 5.916E-04
View 6	1.433E-03 \pm 4.924E-04	1.445E-03 \pm 5.204E-04	1.457E-03 \pm 5.490E-04
View 7	1.289E-03 \pm 1.701E-04	1.290E-03 \pm 1.713E-04	1.290E-03 \pm 1.725E-04
View 8	1.247E-03 \pm 1.682E-04	1.246E-03 \pm 1.681E-04	1.246E-03 \pm 1.683E-04
View 9	1.355E-03 \pm 3.528E-04	1.357E-03 \pm 3.591E-04	1.359E-03 \pm 3.634E-04
View 10	1.396E-03 \pm 5.313E-04	1.406E-03 \pm 5.537E-04	1.413E-03 \pm 5.696E-04
View 11	1.602E-03 \pm 6.197E-04	1.625E-03 \pm 6.477E-04	1.651E-03 \pm 6.794E-04
View 12	1.644E-03 \pm 6.803E-04	1.673E-03 \pm 7.109E-04	1.706E-03 \pm 7.454E-04

Table B.1: Average and standard deviation of average residual (mm) for dataset 30 using LS, Huber and Bisquare estimators

Average Residual \pm Standard Deviation			
No. of View	LS	Huber	Bisquare
View 1	1.617E-03 \pm 6.935E-04	1.639E-03 \pm 7.204E-04	1.659E-03 \pm 7.453E-04
View 2	2.070E-03 \pm 1.380E-03	2.097E-03 \pm 1.404E-03	2.123E-03 \pm 1.421E-03
View 3	1.454E-03 \pm 5.599E-04	1.464E-03 \pm 5.817E-04	1.475E-03 \pm 6.053E-04
View 4	1.630E-03 \pm 6.401E-04	1.644E-03 \pm 6.621E-04	1.659E-03 \pm 6.859E-04
View 5	1.667E-03 \pm 6.037E-04	1.679E-03 \pm 6.180E-04	1.692E-03 \pm 6.339E-04
View 6	1.426E-03 \pm 4.861E-04	1.437E-03 \pm 5.126E-04	1.448E-03 \pm 5.389E-04
View 7	1.325E-03 \pm 2.355E-04	1.325E-03 \pm 2.359E-04	1.325E-03 \pm 2.366E-04
View 8	1.284E-03 \pm 2.538E-04	1.284E-03 \pm 2.540E-04	1.284E-03 \pm 2.545E-04
View 9	1.387E-03 \pm 4.991E-04	1.391E-03 \pm 5.101E-04	1.394E-03 \pm 5.187E-04
View 10	1.433E-03 \pm 6.002E-04	1.444E-03 \pm 6.249E-04	1.452E-03 \pm 6.439E-04
View 11	1.678E-03 \pm 6.260E-04	1.705E-03 \pm 6.561E-04	1.737E-03 \pm 6.907E-04
View 12	1.680E-03 \pm 7.364E-04	1.714E-03 \pm 7.736E-04	1.753E-03 \pm 8.174E-04

Table B.2: Average and standard deviation of average residual (mm) for dataset 31 using LS, Huber and Bisquare estimators

Average Residual \pm Standard Deviation			
No. of View	LS	Huber	Bisquare
View 1	1.630E-03 \pm 7.269E-04	1.652E-03 \pm 7.547E-04	1.673E-03 \pm 7.803E-04
View 2	2.122E-03 \pm 1.508E-03	2.146E-03 \pm 1.524E-03	2.171E-03 \pm 1.540E-03
View 3	1.486E-03 \pm 5.674E-04	1.497E-03 \pm 5.883E-04	1.508E-03 \pm 6.106E-04
View 4	1.673E-03 \pm 6.229E-04	1.688E-03 \pm 6.444E-04	1.704E-03 \pm 6.674E-04
View 5	1.724E-03 \pm 6.691E-04	1.735E-03 \pm 6.801E-04	1.748E-03 \pm 6.937E-04
View 6	1.415E-03 \pm 4.835E-04	1.426E-03 \pm 5.098E-04	1.437E-03 \pm 5.355E-04
View 7	1.309E-03 \pm 2.123E-04	1.309E-03 \pm 2.127E-04	1.310E-03 \pm 2.133E-04
View 8	1.298E-03 \pm 2.766E-04	1.298E-03 \pm 2.770E-04	1.298E-03 \pm 2.777E-04
View 9	1.408E-03 \pm 5.421E-04	1.413E-03 \pm 5.553E-04	1.417E-03 \pm 5.661E-04
View 10	1.451E-03 \pm 6.325E-04	1.463E-03 \pm 6.596E-04	1.473E-03 \pm 6.818E-04
View 11	1.677E-03 \pm 6.404E-04	1.705E-03 \pm 6.714E-04	1.739E-03 \pm 7.074E-04
View 12	1.722E-03 \pm 7.182E-04	1.759E-03 \pm 7.587E-04	1.806E-03 \pm 8.123E-04

Table B.3: Average and standard deviation of average residual (mm) for dataset 32 using LS, Huber and Bisquare estimators

Average Residual \pm Standard Deviation			
No. of View	LS	Huber	Bisquare
View 1	1.517E-03 \pm 6.269E-04	1.538E-03 \pm 6.555E-04	1.564E-03 \pm 6.885E-04
View 2	1.824E-03 \pm 8.587E-04	1.859E-03 \pm 9.032E-04	1.902E-03 \pm 9.609E-04
View 3	1.363E-03 \pm 5.771E-04	1.372E-03 \pm 5.988E-04	1.381E-03 \pm 6.222E-04
View 4	1.534E-03 \pm 6.666E-04	1.548E-03 \pm 6.902E-04	1.563E-03 \pm 7.157E-04
View 5	1.679E-03 \pm 6.058E-04	1.692E-03 \pm 6.211E-04	1.706E-03 \pm 6.368E-04
View 6	1.438E-03 \pm 4.698E-04	1.449E-03 \pm 4.956E-04	1.460E-03 \pm 5.218E-04
View 7	1.254E-03 \pm 1.235E-04	1.254E-03 \pm 1.243E-04	1.255E-03 \pm 1.250E-04
View 8	1.198E-03 \pm 9.974E-05	1.197E-03 \pm 9.968E-05	1.197E-03 \pm 9.968E-05
View 9	1.230E-03 \pm 1.261E-04	1.230E-03 \pm 1.266E-04	1.230E-03 \pm 1.271E-04
View 10	1.427E-03 \pm 5.346E-04	1.438E-03 \pm 5.601E-04	1.451E-03 \pm 5.895E-04
View 11	1.609E-03 \pm 6.162E-04	1.632E-03 \pm 6.439E-04	1.658E-03 \pm 6.757E-04
View 12	1.635E-03 \pm 6.871E-04	1.659E-03 \pm 7.139E-04	1.686E-03 \pm 7.431E-04

Table B.4: Average and standard deviation of average residual (mm) for dataset 33 using LS, Huber and Bisquare estimators

Average Residual \pm Standard Deviation			
No. of View	LS	Huber	Bisquare
View 1	1.555E-03 \pm 6.396E-04	1.579E-03 \pm 6.704E-04	1.607E-03 \pm 7.056E-04
View 2	1.827E-03 \pm 8.544E-04	1.865E-03 \pm 9.019E-04	1.909E-03 \pm 9.587E-04
View 3	1.367E-03 \pm 5.817E-04	1.376E-03 \pm 6.045E-04	1.387E-03 \pm 6.296E-04
View 4	1.574E-03 \pm 6.737E-04	1.590E-03 \pm 6.990E-04	1.607E-03 \pm 7.273E-04
View 5	1.515E-03 \pm 6.256E-04	1.529E-03 \pm 6.474E-04	1.543E-03 \pm 6.709E-04
View 6	1.410E-03 \pm 4.982E-04	1.422E-03 \pm 5.269E-04	1.434E-03 \pm 5.568E-04
View 7	1.289E-03 \pm 2.035E-04	1.290E-03 \pm 2.073E-04	1.292E-03 \pm 2.110E-04
View 8	1.199E-03 \pm 1.001E-04	1.198E-03 \pm 1.000E-04	1.198E-03 \pm 1.000E-04
View 9	1.249E-03 \pm 1.774E-04	1.249E-03 \pm 1.786E-04	1.250E-03 \pm 1.799E-04
View 10	1.375E-03 \pm 4.629E-04	1.384E-03 \pm 4.838E-04	1.393E-03 \pm 5.032E-04
View 11	1.530E-03 \pm 6.063E-04	1.550E-03 \pm 6.345E-04	1.572E-03 \pm 6.666E-04
View 12	1.491E-03 \pm 6.331E-04	1.509E-03 \pm 6.591E-04	1.528E-03 \pm 6.870E-04

Table B.5: Average and standard deviation of average residual (mm) for dataset 34 using LS, Huber and Bisquare estimators

Average Residual \pm Standard Deviation			
No. of View	LS	Huber	Bisquare
View 1	1.531E-03 \pm 6.312E-04	1.553E-03 \pm 6.592E-04	1.572E-03 \pm 6.868E-04
View 2	1.870E-03 \pm 9.458E-04	1.904E-03 \pm 9.871E-04	1.934E-03 \pm 1.017E-03
View 3	1.393E-03 \pm 5.724E-04	1.402E-03 \pm 5.955E-04	1.413E-03 \pm 6.207E-04
View 4	1.585E-03 \pm 6.747E-04	1.601E-03 \pm 7.007E-04	1.619E-03 \pm 7.302E-04
View 5	1.529E-03 \pm 6.188E-04	1.543E-03 \pm 6.411E-04	1.558E-03 \pm 6.654E-04
View 6	1.404E-03 \pm 4.991E-04	1.416E-03 \pm 5.272E-04	1.428E-03 \pm 5.560E-04
View 7	1.297E-03 \pm 2.201E-04	1.299E-03 \pm 2.247E-04	1.301E-03 \pm 2.293E-04
View 8	1.199E-03 \pm 1.025E-04	1.198E-03 \pm 1.024E-04	1.198E-03 \pm 1.024E-04
View 9	1.263E-03 \pm 1.582E-04	1.263E-03 \pm 1.594E-04	1.263E-03 \pm 1.603E-04
View 10	1.373E-03 \pm 4.502E-04	1.381E-03 \pm 4.682E-04	1.386E-03 \pm 4.801E-04
View 11	1.531E-03 \pm 5.980E-04	1.550E-03 \pm 6.267E-04	1.573E-03 \pm 6.596E-04
View 12	1.471E-03 \pm 6.519E-04	1.489E-03 \pm 6.793E-04	1.508E-03 \pm 7.089E-04

Table B.6: Average and standard deviation of average residual (mm) for dataset 35 using LS, Huber and Bisquare estimators

Average Residual \pm Standard Deviation			
No. of View	LS	Huber	Bisquare
View 1	1.461E-03 \pm 7.616E-04	1.481E-03 \pm 8.046E-04	1.514E-03 \pm 8.784E-04
View 2	1.493E-03 \pm 4.255E-04	1.504E-03 \pm 4.409E-04	1.511E-03 \pm 4.522E-04
View 3	1.408E-03 \pm 6.267E-04	1.416E-03 \pm 6.485E-04	1.425E-03 \pm 6.693E-04
View 4	1.594E-03 \pm 1.012E-03	1.614E-03 \pm 1.060E-03	1.642E-03 \pm 1.130E-03
View 5	1.846E-03 \pm 1.341E-03	1.915E-03 \pm 1.495E-03	2.026E-03 \pm 1.756E-03
View 6	1.488E-03 \pm 7.172E-04	1.506E-03 \pm 7.608E-04	1.524E-03 \pm 8.048E-04
View 7	1.451E-03 \pm 5.864E-04	1.466E-03 \pm 6.222E-04	1.481E-03 \pm 6.595E-04
View 8	1.281E-03 \pm 3.281E-04	1.281E-03 \pm 3.279E-04	1.281E-03 \pm 3.281E-04
View 9	2.062E-03 \pm 1.972E-03	2.094E-03 \pm 2.051E-03	2.129E-03 \pm 2.135E-03
View 10	2.269E-03 \pm 2.719E-03	2.407E-03 \pm 3.058E-03	2.737E-03 \pm 3.868E-03
View 11	2.146E-03 \pm 2.495E-03	2.231E-03 \pm 2.702E-03	3.139E-03 \pm 4.927E-03
View 12	1.700E-03 \pm 1.445E-03	1.776E-03 \pm 1.631E-03	2.202E-03 \pm 2.669E-03

Table B.7: Average and standard deviation of average residual (mm) for dataset 36 using LS, Huber and Bisquare estimators

Average Residual \pm Standard Deviation			
No. of View	LS	Huber	Bisquare
View 1	1.478E-03 \pm 7.801E-04	1.496E-03 \pm 8.175E-04	1.522E-03 \pm 8.736E-04
View 2	1.523E-03 \pm 4.533E-04	1.533E-03 \pm 4.679E-04	1.542E-03 \pm 4.797E-04
View 3	1.409E-03 \pm 6.835E-04	1.420E-03 \pm 7.096E-04	1.431E-03 \pm 7.366E-04
View 4	1.600E-03 \pm 1.041E-03	1.621E-03 \pm 1.091E-03	1.652E-03 \pm 1.166E-03
View 5	1.872E-03 \pm 1.401E-03	1.946E-03 \pm 1.569E-03	2.073E-03 \pm 1.867E-03
View 6	1.494E-03 \pm 7.406E-04	1.513E-03 \pm 7.866E-04	1.533E-03 \pm 8.355E-04
View 7	1.460E-03 \pm 6.263E-04	1.478E-03 \pm 6.699E-04	1.498E-03 \pm 7.180E-04
View 8	1.310E-03 \pm 3.948E-04	1.309E-03 \pm 3.947E-04	1.309E-03 \pm 3.950E-04
View 9	2.066E-03 \pm 2.033E-03	2.101E-03 \pm 2.119E-03	2.140E-03 \pm 2.214E-03
View 10	2.318E-03 \pm 2.854E-03	2.455E-03 \pm 3.190E-03	2.818E-03 \pm 4.080E-03
View 11	2.191E-03 \pm 2.492E-03	2.275E-03 \pm 2.697E-03	3.207E-03 \pm 4.978E-03
View 12	1.700E-03 \pm 1.448E-03	1.771E-03 \pm 1.621E-03	2.216E-03 \pm 2.707E-03

Table B.8: Average and standard deviation of average residual (mm) for dataset 37 using LS, Huber and Bisquare estimators

Average Residual \pm Standard Deviation			
No. of View	LS	Huber	Bisquare
View 1	1.480E-03 \pm 7.856E-04	1.497E-03 \pm 8.212E-04	1.520E-03 \pm 8.728E-04
View 2	1.555E-03 \pm 4.760E-04	1.565E-03 \pm 4.883E-04	1.573E-03 \pm 4.986E-04
View 3	1.406E-03 \pm 6.764E-04	1.417E-03 \pm 7.021E-04	1.427E-03 \pm 7.283E-04
View 4	1.603E-03 \pm 1.036E-03	1.623E-03 \pm 1.086E-03	1.654E-03 \pm 1.160E-03
View 5	1.863E-03 \pm 1.389E-03	1.938E-03 \pm 1.556E-03	2.062E-03 \pm 1.848E-03
View 6	1.489E-03 \pm 7.297E-04	1.507E-03 \pm 7.750E-04	1.527E-03 \pm 8.225E-04
View 7	1.449E-03 \pm 5.828E-04	1.464E-03 \pm 6.195E-04	1.481E-03 \pm 6.593E-04
View 8	1.308E-03 \pm 3.988E-04	1.307E-03 \pm 3.986E-04	1.308E-03 \pm 3.990E-04
View 9	2.025E-03 \pm 2.060E-03	2.060E-03 \pm 2.147E-03	2.100E-03 \pm 2.245E-03
View 10	2.330E-03 \pm 2.889E-03	2.466E-03 \pm 3.223E-03	2.832E-03 \pm 4.120E-03
View 11	2.159E-03 \pm 2.525E-03	2.242E-03 \pm 2.729E-03	3.178E-03 \pm 5.024E-03
View 12	1.701E-03 \pm 1.461E-03	1.776E-03 \pm 1.645E-03	2.206E-03 \pm 2.695E-03

Table B.9: Average and standard deviation of average residual (mm) for dataset 38 using LS, Huber and Bisquare estimators

Average Residual \pm Standard Deviation			
No. of View	LS	Huber	Bisquare
View 1	3.461E-03 \pm 5.596E-03	3.175E-03 \pm 4.893E-03	3.179E-03 \pm 4.901E-03
View 2	5.725E-03 \pm 1.044E-02	3.695E-03 \pm 5.446E-03	3.702E-03 \pm 5.444E-03
View 3	1.434E-03 \pm 6.490E-04	1.444E-03 \pm 6.731E-04	1.454E-03 \pm 6.970E-04
View 4	1.648E-03 \pm 9.951E-04	1.668E-03 \pm 1.044E-03	1.697E-03 \pm 1.114E-03
View 5	1.876E-03 \pm 1.378E-03	1.949E-03 \pm 1.542E-03	2.071E-03 \pm 1.828E-03
View 6	1.514E-03 \pm 7.447E-04	1.532E-03 \pm 7.908E-04	1.552E-03 \pm 8.389E-04
View 7	1.420E-03 \pm 6.321E-04	1.436E-03 \pm 6.737E-04	1.455E-03 \pm 7.185E-04
View 8	1.512E-03 \pm 8.982E-04	1.507E-03 \pm 8.867E-04	1.507E-03 \pm 8.870E-04
View 9	5.181E-03 \pm 9.609E-03	4.935E-03 \pm 9.003E-03	5.038E-03 \pm 9.255E-03
View 10	5.597E-03 \pm 1.076E-02	4.766E-03 \pm 8.717E-03	4.765E-03 \pm 8.714E-03
View 11	5.054E-03 \pm 9.636E-03	4.609E-03 \pm 8.548E-03	4.609E-03 \pm 8.546E-03
View 12	4.290E-03 \pm 7.784E-03	3.882E-03 \pm 6.788E-03	3.884E-03 \pm 6.792E-03

Table B.10: Average and standard deviation of average residual (mm) for dataset 39 using LS, Huber and Bisquare estimators

Average Residual \pm Standard Deviation			
No. of View	LS	Huber	Bisquare
View 1	3.204E-03 \pm 4.943E-03	3.027E-03 \pm 4.507E-03	3.044E-03 \pm 4.547E-03
View 2	4.083E-03 \pm 6.366E-03	3.388E-03 \pm 4.638E-03	3.397E-03 \pm 4.635E-03
View 3	1.421E-03 \pm 7.092E-04	1.432E-03 \pm 7.369E-04	1.444E-03 \pm 7.661E-04
View 4	1.631E-03 \pm 1.051E-03	1.652E-03 \pm 1.102E-03	1.683E-03 \pm 1.175E-03
View 5	1.913E-03 \pm 1.475E-03	1.995E-03 \pm 1.659E-03	2.149E-03 \pm 2.021E-03
View 6	1.530E-03 \pm 7.937E-04	1.550E-03 \pm 8.410E-04	1.569E-03 \pm 8.894E-04
View 7	1.450E-03 \pm 7.001E-04	1.472E-03 \pm 7.542E-04	1.497E-03 \pm 8.161E-04
View 8	1.362E-03 \pm 5.476E-04	1.360E-03 \pm 5.441E-04	1.360E-03 \pm 5.443E-04
View 9	2.475E-03 \pm 3.068E-03	2.552E-03 \pm 3.259E-03	2.641E-03 \pm 3.477E-03
View 10	2.709E-03 \pm 3.796E-03	2.851E-03 \pm 4.145E-03	3.559E-03 \pm 5.879E-03
View 11	2.244E-03 \pm 2.709E-03	2.321E-03 \pm 2.900E-03	3.426E-03 \pm 5.606E-03
View 12	1.762E-03 \pm 1.571E-03	1.835E-03 \pm 1.749E-03	2.366E-03 \pm 3.043E-03

Table B.11: Average and standard deviation of average residual (mm) for dataset 40 using LS, Huber and Bisquare estimators

Appendix C

Average and Standard Deviation of Average Radius (Datasets: 60-70)

Radius \pm Standard Deviation			
No. of View	LS	Huber	Bisquare
View 1	19.6253 \pm 0.1804	19.6388 \pm 0.1736	19.6373 \pm 0.1705
View 2	19.6862 \pm 0.1200	19.7016 \pm 0.1197	19.7009 \pm 0.1195
View 3	19.7485 \pm 0.1472	19.7610 \pm 0.1425	19.7597 \pm 0.1399
View 4	19.7396 \pm 0.1764	19.7513 \pm 0.1702	19.7500 \pm 0.1684
View 5	19.7391 \pm 0.1739	19.7518 \pm 0.1661	19.7509 \pm 0.1653
View 6	19.7391 \pm 0.1691	19.7572 \pm 0.1724	19.7570 \pm 0.1731
View 7	19.6700 \pm 0.2321	19.6877 \pm 0.2316	19.6866 \pm 0.2311
View 8	19.6089 \pm 0.1710	19.6286 \pm 0.1733	19.6284 \pm 0.1738
View 9	19.6043 \pm 0.1965	19.6231 \pm 0.1995	19.6230 \pm 0.2001
View 10	19.5370 \pm 0.1486	19.5545 \pm 0.1518	19.5544 \pm 0.1519
View 11	19.5681 \pm 0.1405	19.5866 \pm 0.1453	19.5865 \pm 0.1451
View 12	19.5600 \pm 0.1490	19.5751 \pm 0.1479	19.5748 \pm 0.1476

Table C.1: Average and standard deviation of average radius (mm) for dataset 60 obtained from LS, Huber and Bisquare estimators

Radius \pm Standard Deviation			
No. of View	LS	Huber	Bisquare
View 1	19.6310 \pm 0.1750	19.6385 \pm 0.1535	19.6376 \pm 0.1518
View 2	19.6949 \pm 0.1200	19.7118 \pm 0.1203	19.7117 \pm 0.1205
View 3	19.7593 \pm 0.1434	19.7725 \pm 0.1401	19.7711 \pm 0.1377
View 4	19.7538 \pm 0.1605	19.7647 \pm 0.1573	19.7631 \pm 0.1556
View 5	19.7853 \pm 0.1762	19.7933 \pm 0.1708	19.7903 \pm 0.1686
View 6	19.7560 \pm 0.1880	19.7718 \pm 0.1892	19.7707 \pm 0.1888
View 7	19.6760 \pm 0.2108	19.6909 \pm 0.2047	19.6885 \pm 0.2028
View 8	19.5993 \pm 0.1405	19.6183 \pm 0.1415	19.6184 \pm 0.1422
View 9	19.6245 \pm 0.2134	19.6397 \pm 0.2108	19.6401 \pm 0.2115
View 10	19.5943 \pm 0.2277	19.6123 \pm 0.2325	19.6122 \pm 0.2327
View 11	19.5959 \pm 0.1676	19.6142 \pm 0.1732	19.6141 \pm 0.1732
View 12	19.5571 \pm 0.1258	19.5749 \pm 0.1284	19.5749 \pm 0.1284

Table C.2: Average and standard deviation of average radius (mm) for dataset 61 obtained from LS, Huber and Bisquare estimators

Radius \pm Standard Deviation			
No. of View	LS	Huber	Bisquare
View 1	19.6282 \pm 0.1726	19.6425 \pm 0.1658	19.6409 \pm 0.1623
View 2	19.7142 \pm 0.1364	19.7306 \pm 0.1368	19.7298 \pm 0.1360
View 3	19.7392 \pm 0.1130	19.7542 \pm 0.1120	19.7542 \pm 0.1122
View 4	19.7566 \pm 0.1521	19.7692 \pm 0.1481	19.7672 \pm 0.1471
View 5	19.7914 \pm 0.1906	19.8008 \pm 0.1816	19.7969 \pm 0.1780
View 6	19.7508 \pm 0.1784	19.7699 \pm 0.1807	19.7693 \pm 0.1811
View 7	19.6616 \pm 0.1767	19.6755 \pm 0.1678	19.6733 \pm 0.1662
View 8	19.6057 \pm 0.1475	19.6237 \pm 0.1476	19.6236 \pm 0.1480
View 9	19.6369 \pm 0.2299	19.6547 \pm 0.2323	19.6548 \pm 0.2327
View 10	19.5687 \pm 0.1614	19.5867 \pm 0.1655	19.5867 \pm 0.1656
View 11	19.5774 \pm 0.1323	19.5956 \pm 0.1365	19.5956 \pm 0.1367
View 12	19.5547 \pm 0.1058	19.5721 \pm 0.1079	19.5719 \pm 0.1078

Table C.3: Average and standard deviation of average radius (mm) for dataset 62 obtained from LS, Huber and Bisquare estimators

Radius \pm Standard Deviation			
No. of View	LS	Huber	Bisquare
View 1	19.9443 \pm 0.4900	19.8449 \pm 0.3159	19.8032 \pm 0.2553
View 2	19.9000 \pm 0.3392	19.8101 \pm 0.1716	19.7593 \pm 0.1101
View 3	20.0585 \pm 0.4738	19.9486 \pm 0.3726	19.9099 \pm 0.3508
View 4	20.3947 \pm 0.6738	20.1986 \pm 0.5142	20.1106 \pm 0.4521
View 5	19.9265 \pm 0.4880	19.8316 \pm 0.2309	19.7418 \pm 0.1339
View 6	19.7380 \pm 0.2125	19.6791 \pm 0.1754	19.6522 \pm 0.1650
View 7	19.5947 \pm 0.1606	19.6123 \pm 0.1580	19.6104 \pm 0.1572
View 8	19.6515 \pm 0.3583	19.6197 \pm 0.2513	19.6040 \pm 0.2217
View 9	19.5346 \pm 0.1382	19.5505 \pm 0.1381	19.5486 \pm 0.1362
View 10	19.5295 \pm 0.1202	19.5473 \pm 0.1233	19.5465 \pm 0.1234
View 11	19.5979 \pm 0.1601	19.5790 \pm 0.1278	19.5676 \pm 0.1198
View 12	19.7811 \pm 0.6232	19.7163 \pm 0.4171	19.6712 \pm 0.3085

Table C.4: Average and standard deviation of average radius (mm) for dataset 63 obtained from LS, Huber and Bisquare estimators

Radius \pm Standard Deviation			
No. of View	LS	Huber	Bisquare
View 1	19.9452 \pm 0.6935	19.8799 \pm 0.5126	19.8196 \pm 0.3759
View 2	20.1762 \pm 0.7177	20.0524 \pm 0.6049	20.0128 \pm 0.5987
View 3	20.2724 \pm 0.6750	20.1100 \pm 0.6125	20.0382 \pm 0.6407
View 4	20.5501 \pm 0.8386	20.4164 \pm 0.8330	20.3384 \pm 0.8289
View 5	20.0239 \pm 0.7144	20.0141 \pm 0.6544	20.0105 \pm 0.6488
View 6	20.0151 \pm 0.4440	19.8185 \pm 0.2710	19.7226 \pm 0.2072
View 7	19.5774 \pm 0.1444	19.5870 \pm 0.1402	19.5831 \pm 0.1402
View 8	19.6529 \pm 0.3162	19.6210 \pm 0.2317	19.6027 \pm 0.2070
View 9	19.5863 \pm 0.2881	19.5530 \pm 0.1697	19.5310 \pm 0.1231
View 10	19.5024 \pm 0.1135	19.5209 \pm 0.1109	19.5206 \pm 0.1110
View 11	19.6820 \pm 0.2673	19.6248 \pm 0.1583	19.5908 \pm 0.1273
View 12	19.7786 \pm 0.5668	19.7240 \pm 0.3870	19.6806 \pm 0.2827

Table C.5: Average and standard deviation of average radius (mm) for dataset 64 obtained from LS, Huber and Bisquare estimators

Radius \pm Standard Deviation			
No. of View	LS	Huber	Bisquare
View 1	20.1266 \pm 0.7594	20.0128 \pm 0.6273	19.9641 \pm 0.5834
View 2	20.2724 \pm 0.8143	20.1695 \pm 0.7477	20.1301 \pm 0.7404
View 3	20.3091 \pm 0.7123	20.1530 \pm 0.6619	20.0753 \pm 0.6795
View 4	20.5591 \pm 0.8351	20.4316 \pm 0.8297	20.3549 \pm 0.8138
View 5	20.0495 \pm 0.6871	20.0109 \pm 0.6357	19.9932 \pm 0.6328
View 6	20.0608 \pm 0.5686	19.8590 \pm 0.3518	19.7119 \pm 0.2010
View 7	19.6046 \pm 0.2125	19.6050 \pm 0.1668	19.5966 \pm 0.1538
View 8	19.5905 \pm 0.2124	19.5946 \pm 0.1952	19.5902 \pm 0.1902
View 9	19.5868 \pm 0.2486	19.5720 \pm 0.1600	19.5519 \pm 0.1249
View 10	19.5374 \pm 0.1227	19.5527 \pm 0.1196	19.5514 \pm 0.1179
View 11	19.5745 \pm 0.1222	19.5741 \pm 0.1072	19.5661 \pm 0.1020
View 12	19.8043 \pm 0.6266	19.7448 \pm 0.4357	19.6954 \pm 0.3166

Table C.6: Average and standard deviation of average radius (mm) for dataset 65 obtained from LS, Huber and Bisquare estimators

Radius \pm Standard Deviation			
No. of View	LS	Huber	Bisquare
View 1	20.0187 \pm 0.5197	19.8716 \pm 0.3416	19.8107 \pm 0.2839
View 2	20.0167 \pm 0.4064	19.8560 \pm 0.2256	19.7804 \pm 0.1536
View 3	20.2216 \pm 0.4038	20.0062 \pm 0.3112	19.9172 \pm 0.3241
View 4	20.3851 \pm 0.6308	20.1670 \pm 0.4579	20.0346 \pm 0.3253
View 5	19.9993 \pm 0.5011	19.8590 \pm 0.2726	19.7444 \pm 0.1379
View 6	19.7336 \pm 0.1907	19.6745 \pm 0.1541	19.6464 \pm 0.1467
View 7	19.6117 \pm 0.2202	19.5994 \pm 0.1636	19.5878 \pm 0.1482
View 8	19.7195 \pm 0.3957	19.6704 \pm 0.3180	19.6422 \pm 0.2984
View 9	19.5137 \pm 0.1386	19.5328 \pm 0.1397	19.5324 \pm 0.1394
View 10	19.5025 \pm 0.1115	19.5224 \pm 0.1067	19.5209 \pm 0.1067
View 11	19.5965 \pm 0.1688	19.5785 \pm 0.1239	19.5665 \pm 0.1193
View 12	19.8013 \pm 0.4840	19.7554 \pm 0.3458	19.7299 \pm 0.2941

Table C.7: Average and standard deviation of average radius (mm) for dataset 66 obtained from LS, Huber and Bisquare estimators

Radius \pm Standard Deviation			
No. of View	LS	Huber	Bisquare
View 1	20.0094 \pm 0.5328	19.8535 \pm 0.3546	19.7872 \pm 0.2986
View 2	20.1513 \pm 0.5927	19.9576 \pm 0.3936	19.8516 \pm 0.3178
View 3	20.2605 \pm 0.4566	20.0342 \pm 0.3262	19.9283 \pm 0.3310
View 4	20.4951 \pm 0.7043	20.2763 \pm 0.5463	20.1570 \pm 0.4491
View 5	20.1170 \pm 0.5727	20.0093 \pm 0.4345	19.9712 \pm 0.4145
View 6	19.7534 \pm 0.2016	19.6776 \pm 0.1472	19.6446 \pm 0.1329
View 7	19.6260 \pm 0.2419	19.5999 \pm 0.1663	19.5827 \pm 0.1439
View 8	19.7257 \pm 0.4246	19.6776 \pm 0.3350	19.6495 \pm 0.3104
View 9	19.5269 \pm 0.1437	19.5392 \pm 0.1285	19.5368 \pm 0.1232
View 10	19.5010 \pm 0.1210	19.5166 \pm 0.1150	19.5150 \pm 0.1151
View 11	19.5368 \pm 0.1293	19.5545 \pm 0.1316	19.5535 \pm 0.1305
View 12	19.7550 \pm 0.4929	19.7119 \pm 0.3540	19.6879 \pm 0.3007

Table C.8: Average and standard deviation of average radius (mm) for dataset 67 obtained from LS, Huber and Bisquare estimators

Radius \pm Standard Deviation			
No. of View	LS	Huber	Bisquare
View 1	20.1036 \pm 0.6543	19.9387 \pm 0.4948	19.8586 \pm 0.4455
View 2	20.1093 \pm 0.6860	20.0151 \pm 0.5892	19.9793 \pm 0.5755
View 3	20.3475 \pm 0.6317	20.1525 \pm 0.5908	20.0469 \pm 0.6031
View 4	20.5609 \pm 0.7816	20.4502 \pm 0.7735	20.3689 \pm 0.7410
View 5	20.1721 \pm 0.6347	20.0634 \pm 0.5910	20.0053 \pm 0.5941
View 6	20.1107 \pm 0.6654	19.9965 \pm 0.6118	19.9506 \pm 0.6052
View 7	19.6092 \pm 0.2558	19.5958 \pm 0.1732	19.5748 \pm 0.1451
View 8	19.6886 \pm 0.3700	19.6415 \pm 0.2652	19.6131 \pm 0.2309
View 9	19.5263 \pm 0.1370	19.5479 \pm 0.1419	19.5468 \pm 0.1408
View 10	19.5232 \pm 0.1126	19.5436 \pm 0.1133	19.5430 \pm 0.1126
View 11	19.5589 \pm 0.1286	19.5765 \pm 0.1435	19.5643 \pm 0.1303
View 12	19.7894 \pm 0.5545	19.7437 \pm 0.4145	19.7122 \pm 0.3437

Table C.9: Average and standard deviation of average radius (mm) for dataset 68 obtained from LS, Huber and Bisquare estimators

Radius \pm Standard Deviation			
No. of View	LS	Huber	Bisquare
View 1	19.674 \pm 0.125	19.695 \pm 0.127	19.695 \pm 0.128
View 2	19.663 \pm 0.178	19.682 \pm 0.174	19.687 \pm 0.174
View 3	19.721 \pm 0.123	19.741 \pm 0.120	19.742 \pm 0.121
View 4	19.598 \pm 0.160	19.622 \pm 0.162	19.622 \pm 0.163
View 5	19.544 \pm 0.146	19.574 \pm 0.149	19.573 \pm 0.149
View 6	19.505 \pm 0.139	19.530 \pm 0.135	19.530 \pm 0.136
View 7	19.617 \pm 0.336	19.641 \pm 0.340	19.641 \pm 0.340
View 8	19.489 \pm 0.118	19.514 \pm 0.120	19.514 \pm 0.120
View 9	19.487 \pm 0.087	19.508 \pm 0.086	19.508 \pm 0.086
View 10	19.475 \pm 0.102	19.497 \pm 0.102	19.497 \pm 0.102
View 11	19.544 \pm 0.102	19.566 \pm 0.102	19.566 \pm 0.102
View 12	19.599 \pm 0.144	19.621 \pm 0.144	19.621 \pm 0.145

Table C.10: Average and standard deviation of average radius (mm) for dataset 69 obtained from LS, Huber and Bisquare estimators

Radius \pm Standard Deviation			
No. of View	LS	Huber	Bisquare
View 1	20.211 \pm 0.829	20.093 \pm 0.715	20.051 \pm 0.698
View 2	20.206 \pm 0.660	20.049 \pm 0.540	19.992 \pm 0.546
View 3	20.700 \pm 1.070	20.575 \pm 1.153	20.475 \pm 1.152
View 4	20.130 \pm 0.769	20.007 \pm 0.566	19.949 \pm 0.502
View 5	19.816 \pm 0.433	19.713 \pm 0.285	19.656 \pm 0.219
View 6	19.547 \pm 0.135	19.558 \pm 0.122	19.556 \pm 0.120
View 7	19.638 \pm 0.331	19.647 \pm 0.336	19.644 \pm 0.339
View 8	19.631 \pm 0.176	19.594 \pm 0.137	19.575 \pm 0.140
View 9	19.689 \pm 0.417	19.639 \pm 0.300	19.595 \pm 0.214
View 10	19.568 \pm 0.148	19.571 \pm 0.152	19.564 \pm 0.151
View 11	19.806 \pm 0.664	19.732 \pm 0.462	19.679 \pm 0.348
View 12	19.898 \pm 0.721	19.840 \pm 0.549	19.789 \pm 0.433

Table C.11: Average and standard deviation of average radius (mm) for dataset 70 obtained from LS, Huber and Bisquare estimators

Appendix D

Average and Standard Deviation of Average Average Residual (Datasets: 60-70)

Average Residual \pm Standard Deviation			
No. of View	LS	Huber	Bisquare
View 1	1.260E-03 \pm 1.348E-04	1.260E-03 \pm 1.348E-04	1.260E-03 \pm 1.349E-04
View 2	1.135E-03 \pm 7.820E-05	1.135E-03 \pm 7.819E-05	1.135E-03 \pm 7.821E-05
View 3	1.105E-03 \pm 1.439E-04	1.105E-03 \pm 1.439E-04	1.105E-03 \pm 1.439E-04
View 4	1.116E-03 \pm 1.670E-04	1.115E-03 \pm 1.670E-04	1.115E-03 \pm 1.670E-04
View 5	1.204E-03 \pm 7.265E-05	1.204E-03 \pm 7.265E-05	1.204E-03 \pm 7.267E-05
View 6	1.258E-03 \pm 1.135E-04	1.257E-03 \pm 1.134E-04	1.257E-03 \pm 1.134E-04
View 7	1.411E-03 \pm 3.909E-04	1.411E-03 \pm 3.907E-04	1.411E-03 \pm 3.907E-04
View 8	1.302E-03 \pm 2.159E-04	1.301E-03 \pm 2.157E-04	1.301E-03 \pm 2.157E-04
View 9	1.312E-03 \pm 1.896E-04	1.312E-03 \pm 1.893E-04	1.312E-03 \pm 1.893E-04
View 10	1.336E-03 \pm 2.976E-04	1.336E-03 \pm 2.973E-04	1.336E-03 \pm 2.973E-04
View 11	1.318E-03 \pm 2.718E-04	1.318E-03 \pm 2.713E-04	1.318E-03 \pm 2.713E-04
View 12	1.269E-03 \pm 1.274E-04	1.269E-03 \pm 1.273E-04	1.269E-03 \pm 1.273E-04

Table D.1: Average and standard deviation of average residual (mm) for dataset 60 using LS, Huber and Bisquare estimators

Average Residual \pm Standard Deviation			
No. of View	LS	Huber	Bisquare
View 1	1.302E-03 \pm 1.901E-04	1.302E-03 \pm 1.908E-04	1.302E-03 \pm 1.909E-04
View 2	1.126E-03 \pm 5.812E-05	1.125E-03 \pm 5.804E-05	1.125E-03 \pm 5.804E-05
View 3	1.096E-03 \pm 1.357E-04	1.096E-03 \pm 1.357E-04	1.096E-03 \pm 1.357E-04
View 4	1.116E-03 \pm 1.668E-04	1.115E-03 \pm 1.667E-04	1.116E-03 \pm 1.668E-04
View 5	1.265E-03 \pm 1.994E-04	1.265E-03 \pm 1.995E-04	1.265E-03 \pm 1.999E-04
View 6	1.285E-03 \pm 1.446E-04	1.284E-03 \pm 1.445E-04	1.284E-03 \pm 1.446E-04
View 7	1.425E-03 \pm 4.215E-04	1.424E-03 \pm 4.215E-04	1.424E-03 \pm 4.217E-04
View 8	1.333E-03 \pm 2.678E-04	1.332E-03 \pm 2.676E-04	1.332E-03 \pm 2.676E-04
View 9	1.346E-03 \pm 2.579E-04	1.345E-03 \pm 2.577E-04	1.345E-03 \pm 2.577E-04
View 10	1.321E-03 \pm 2.878E-04	1.321E-03 \pm 2.875E-04	1.321E-03 \pm 2.875E-04
View 11	1.290E-03 \pm 2.258E-04	1.290E-03 \pm 2.254E-04	1.290E-03 \pm 2.254E-04
View 12	1.261E-03 \pm 1.290E-04	1.261E-03 \pm 1.288E-04	1.261E-03 \pm 1.288E-04

Table D.2: Average and standard deviation of average residual (mm) for dataset 61 using LS, Huber and Bisquare estimators

Average Residual \pm Standard Deviation			
No. of View	LS	Huber	Bisquare
View 1	1.280E-03 \pm 1.791E-04	1.280E-03 \pm 1.790E-04	1.280E-03 \pm 1.790E-04
View 2	1.140E-03 \pm 9.894E-05	1.140E-03 \pm 9.888E-05	1.140E-03 \pm 9.890E-05
View 3	1.072E-03 \pm 1.212E-04	1.072E-03 \pm 1.212E-04	1.072E-03 \pm 1.212E-04
View 4	1.119E-03 \pm 1.686E-04	1.119E-03 \pm 1.686E-04	1.119E-03 \pm 1.686E-04
View 5	1.293E-03 \pm 2.868E-04	1.293E-03 \pm 2.869E-04	1.293E-03 \pm 2.876E-04
View 6	1.282E-03 \pm 1.459E-04	1.282E-03 \pm 1.458E-04	1.282E-03 \pm 1.458E-04
View 7	1.439E-03 \pm 4.561E-04	1.438E-03 \pm 4.563E-04	1.439E-03 \pm 4.565E-04
View 8	1.340E-03 \pm 2.574E-04	1.339E-03 \pm 2.571E-04	1.339E-03 \pm 2.571E-04
View 9	1.268E-03 \pm 1.268E-04	1.268E-03 \pm 1.267E-04	1.268E-03 \pm 1.267E-04
View 10	1.292E-03 \pm 2.166E-04	1.292E-03 \pm 2.163E-04	1.292E-03 \pm 2.163E-04
View 11	1.306E-03 \pm 2.266E-04	1.305E-03 \pm 2.262E-04	1.305E-03 \pm 2.262E-04
View 12	1.268E-03 \pm 1.476E-04	1.268E-03 \pm 1.474E-04	1.268E-03 \pm 1.474E-04

Table D.3: Average and standard deviation of average residual (mm) for dataset 62 using LS, Huber and Bisquare estimators

Average Residual \pm Standard Deviation			
No. of View	LS	Huber	Bisquare
View 1	1.674E-03 \pm 7.895E-04	1.701E-03 \pm 8.331E-04	1.728E-03 \pm 8.742E-04
View 2	1.478E-03 \pm 6.048E-04	1.499E-03 \pm 6.448E-04	1.531E-03 \pm 7.064E-04
View 3	1.708E-03 \pm 7.519E-04	1.728E-03 \pm 7.761E-04	1.743E-03 \pm 7.930E-04
View 4	2.431E-03 \pm 1.304E-03	2.491E-03 \pm 1.375E-03	2.555E-03 \pm 1.462E-03
View 5	1.698E-03 \pm 8.106E-04	1.735E-03 \pm 8.996E-04	1.816E-03 \pm 1.096E-03
View 6	1.850E-03 \pm 6.443E-04	1.858E-03 \pm 6.496E-04	1.865E-03 \pm 6.551E-04
View 7	1.487E-03 \pm 3.534E-04	1.486E-03 \pm 3.534E-04	1.487E-03 \pm 3.536E-04
View 8	1.532E-03 \pm 5.250E-04	1.543E-03 \pm 5.509E-04	1.553E-03 \pm 5.727E-04
View 9	1.571E-03 \pm 7.511E-04	1.571E-03 \pm 7.518E-04	1.572E-03 \pm 7.538E-04
View 10	1.395E-03 \pm 2.717E-04	1.394E-03 \pm 2.710E-04	1.394E-03 \pm 2.710E-04
View 11	1.579E-03 \pm 3.830E-04	1.583E-03 \pm 3.885E-04	1.586E-03 \pm 3.931E-04
View 12	1.826E-03 \pm 1.182E-03	1.850E-03 \pm 1.239E-03	1.881E-03 \pm 1.315E-03

Table D.4: Average and standard deviation of average residual (mm) for dataset 63 using LS, Huber and Bisquare estimators

Average Residual \pm Standard Deviation			
No. of View	LS	Huber	Bisquare
View 1	1.674E-03 \pm 1.098E-03	1.699E-03 \pm 1.159E-03	1.749E-03 \pm 1.279E-03
View 2	1.901E-03 \pm 1.072E-03	1.928E-03 \pm 1.101E-03	1.949E-03 \pm 1.113E-03
View 3	1.993E-03 \pm 9.723E-04	2.029E-03 \pm 1.002E-03	2.077E-03 \pm 1.043E-03
View 4	2.582E-03 \pm 1.387E-03	2.622E-03 \pm 1.418E-03	2.674E-03 \pm 1.466E-03
View 5	1.760E-03 \pm 8.837E-04	1.763E-03 \pm 8.927E-04	1.764E-03 \pm 8.944E-04
View 6	2.212E-03 \pm 9.649E-04	2.260E-03 \pm 1.011E-03	2.322E-03 \pm 1.075E-03
View 7	1.447E-03 \pm 3.575E-04	1.447E-03 \pm 3.582E-04	1.447E-03 \pm 3.590E-04
View 8	1.522E-03 \pm 4.597E-04	1.530E-03 \pm 4.781E-04	1.540E-03 \pm 4.988E-04
View 9	1.768E-03 \pm 8.625E-04	1.776E-03 \pm 8.699E-04	1.787E-03 \pm 8.804E-04
View 10	1.470E-03 \pm 5.132E-04	1.469E-03 \pm 5.125E-04	1.469E-03 \pm 5.125E-04
View 11	1.860E-03 \pm 6.092E-04	1.874E-03 \pm 6.241E-04	1.890E-03 \pm 6.427E-04
View 12	1.814E-03 \pm 1.212E-03	1.836E-03 \pm 1.266E-03	1.869E-03 \pm 1.343E-03

Table D.5: Average and standard deviation of average residual (mm) for dataset 64 using LS, Huber and Bisquare estimators

Average Residual \pm Standard Deviation			
No. of View	LS	Huber	Bisquare
View 1	1.983E-03 \pm 1.190E-03	2.013E-03 \pm 1.230E-03	2.040E-03 \pm 1.263E-03
View 2	2.179E-03 \pm 1.399E-03	2.206E-03 \pm 1.425E-03	2.232E-03 \pm 1.450E-03
View 3	2.077E-03 \pm 1.090E-03	2.114E-03 \pm 1.116E-03	2.165E-03 \pm 1.155E-03
View 4	2.616E-03 \pm 1.439E-03	2.655E-03 \pm 1.466E-03	2.702E-03 \pm 1.504E-03
View 5	2.014E-03 \pm 9.682E-04	2.021E-03 \pm 9.786E-04	2.027E-03 \pm 9.849E-04
View 6	2.303E-03 \pm 1.120E-03	2.361E-03 \pm 1.192E-03	2.489E-03 \pm 1.376E-03
View 7	1.543E-03 \pm 3.951E-04	1.544E-03 \pm 3.990E-04	1.547E-03 \pm 4.033E-04
View 8	1.380E-03 \pm 2.432E-04	1.380E-03 \pm 2.446E-04	1.381E-03 \pm 2.459E-04
View 9	1.989E-03 \pm 1.416E-03	1.995E-03 \pm 1.419E-03	2.005E-03 \pm 1.430E-03
View 10	1.462E-03 \pm 4.511E-04	1.461E-03 \pm 4.505E-04	1.461E-03 \pm 4.505E-04
View 11	1.636E-03 \pm 5.750E-04	1.638E-03 \pm 5.780E-04	1.640E-03 \pm 5.813E-04
View 12	1.852E-03 \pm 1.303E-03	1.877E-03 \pm 1.365E-03	1.916E-03 \pm 1.458E-03

Table D.6: Average and standard deviation of average residual (mm) for dataset 65 using LS, Huber and Bisquare estimators

Average Residual \pm Standard Deviation			
No. of View	LS	Huber	Bisquare
View 1	1.840E-03 \pm 8.448E-04	1.876E-03 \pm 8.875E-04	1.912E-03 \pm 9.293E-04
View 2	1.994E-03 \pm 1.240E-03	2.038E-03 \pm 1.292E-03	2.090E-03 \pm 1.356E-03
View 3	2.099E-03 \pm 6.147E-04	2.143E-03 \pm 6.525E-04	2.195E-03 \pm 7.014E-04
View 4	2.426E-03 \pm 1.341E-03	2.489E-03 \pm 1.405E-03	2.581E-03 \pm 1.520E-03
View 5	1.963E-03 \pm 7.963E-04	2.003E-03 \pm 8.550E-04	2.097E-03 \pm 1.014E-03
View 6	1.858E-03 \pm 6.274E-04	1.866E-03 \pm 6.335E-04	1.874E-03 \pm 6.400E-04
View 7	1.553E-03 \pm 4.595E-04	1.557E-03 \pm 4.682E-04	1.561E-03 \pm 4.769E-04
View 8	1.627E-03 \pm 5.659E-04	1.641E-03 \pm 5.989E-04	1.660E-03 \pm 6.400E-04
View 9	1.565E-03 \pm 6.455E-04	1.564E-03 \pm 6.446E-04	1.564E-03 \pm 6.446E-04
View 10	1.590E-03 \pm 7.759E-04	1.589E-03 \pm 7.743E-04	1.589E-03 \pm 7.745E-04
View 11	1.547E-03 \pm 4.825E-04	1.552E-03 \pm 4.954E-04	1.558E-03 \pm 5.068E-04
View 12	1.814E-03 \pm 1.004E-03	1.827E-03 \pm 1.036E-03	1.840E-03 \pm 1.065E-03

Table D.7: Average and standard deviation of average residual (mm) for dataset 66 using LS, Huber and Bisquare estimators

Average Residual \pm Standard Deviation			
No. of View	LS	Huber	Bisquare
View 1	1.837E-03 \pm 8.464E-04	1.875E-03 \pm 8.913E-04	1.914E-03 \pm 9.357E-04
View 2	2.127E-03 \pm 1.335E-03	2.184E-03 \pm 1.392E-03	2.265E-03 \pm 1.470E-03
View 3	2.144E-03 \pm 6.772E-04	2.196E-03 \pm 7.299E-04	2.269E-03 \pm 8.197E-04
View 4	2.508E-03 \pm 1.384E-03	2.571E-03 \pm 1.433E-03	2.648E-03 \pm 1.500E-03
View 5	2.098E-03 \pm 9.949E-04	2.124E-03 \pm 1.027E-03	2.141E-03 \pm 1.047E-03
View 6	1.854E-03 \pm 6.635E-04	1.864E-03 \pm 6.714E-04	1.874E-03 \pm 6.795E-04
View 7	1.653E-03 \pm 5.458E-04	1.659E-03 \pm 5.578E-04	1.666E-03 \pm 5.705E-04
View 8	1.593E-03 \pm 6.301E-04	1.609E-03 \pm 6.659E-04	1.629E-03 \pm 7.114E-04
View 9	1.647E-03 \pm 8.231E-04	1.647E-03 \pm 8.221E-04	1.647E-03 \pm 8.220E-04
View 10	1.580E-03 \pm 7.483E-04	1.579E-03 \pm 7.474E-04	1.580E-03 \pm 7.477E-04
View 11	1.402E-03 \pm 3.074E-04	1.401E-03 \pm 3.072E-04	1.401E-03 \pm 3.075E-04
View 12	1.880E-03 \pm 9.997E-04	1.893E-03 \pm 1.028E-03	1.905E-03 \pm 1.053E-03

Table D.8: Average and standard deviation of average residual (mm) for dataset 67 using LS, Huber and Bisquare estimators

Average Residual \pm Standard Deviation			
No. of View	LS	Huber	Bisquare
View 1	2.104E-03 \pm 1.187E-03	2.149E-03 \pm 1.237E-03	2.203E-03 \pm 1.294E-03
View 2	1.962E-03 \pm 1.111E-03	1.983E-03 \pm 1.133E-03	2.001E-03 \pm 1.146E-03
View 3	2.340E-03 \pm 9.528E-04	2.388E-03 \pm 9.826E-04	2.462E-03 \pm 1.043E-03
View 4	2.775E-03 \pm 1.605E-03	2.815E-03 \pm 1.631E-03	2.868E-03 \pm 1.671E-03
View 5	2.357E-03 \pm 1.228E-03	2.388E-03 \pm 1.254E-03	2.426E-03 \pm 1.285E-03
View 6	2.493E-03 \pm 1.417E-03	2.520E-03 \pm 1.442E-03	2.546E-03 \pm 1.463E-03
View 7	1.954E-03 \pm 1.079E-03	1.962E-03 \pm 1.088E-03	1.974E-03 \pm 1.102E-03
View 8	1.681E-03 \pm 6.843E-04	1.695E-03 \pm 7.134E-04	1.714E-03 \pm 7.509E-04
View 9	1.599E-03 \pm 7.703E-04	1.598E-03 \pm 7.687E-04	1.598E-03 \pm 7.690E-04
View 10	1.551E-03 \pm 6.899E-04	1.550E-03 \pm 6.885E-04	1.550E-03 \pm 6.885E-04
View 11	1.918E-03 \pm 1.250E-03	1.920E-03 \pm 1.250E-03	1.926E-03 \pm 1.261E-03
View 12	2.002E-03 \pm 1.344E-03	2.019E-03 \pm 1.383E-03	2.038E-03 \pm 1.426E-03

Table D.9: Average and standard deviation of average residual (mm) for dataset 68 using LS, Huber and Bisquare estimators

Average Residual \pm Standard Deviation			
No. of View	LS	Huber	Bisquare
View 1	5.275E-04 \pm 1.746E-04	5.272E-04 \pm 1.744E-04	5.272E-04 \pm 1.744E-04
View 2	4.916E-04 \pm 8.511E-05	4.914E-04 \pm 8.503E-05	4.914E-04 \pm 8.503E-05
View 3	4.768E-04 \pm 3.061E-05	4.766E-04 \pm 3.063E-05	4.766E-04 \pm 3.063E-05
View 4	5.200E-04 \pm 4.860E-05	5.197E-04 \pm 4.856E-05	5.197E-04 \pm 4.856E-05
View 5	6.162E-04 \pm 2.105E-04	6.158E-04 \pm 2.101E-04	6.158E-04 \pm 2.101E-04
View 6	5.801E-04 \pm 1.670E-04	5.798E-04 \pm 1.668E-04	5.798E-04 \pm 1.668E-04
View 7	5.411E-04 \pm 7.231E-05	5.408E-04 \pm 7.227E-05	5.408E-04 \pm 7.227E-05
View 8	6.667E-04 \pm 3.223E-04	6.663E-04 \pm 3.218E-04	6.663E-04 \pm 3.218E-04
View 9	6.354E-04 \pm 2.907E-04	6.351E-04 \pm 2.904E-04	6.351E-04 \pm 2.904E-04
View 10	5.266E-04 \pm 3.816E-05	5.264E-04 \pm 3.811E-05	5.264E-04 \pm 3.811E-05
View 11	6.230E-04 \pm 2.415E-04	6.227E-04 \pm 2.412E-04	6.227E-04 \pm 2.412E-04
View 12	5.078E-04 \pm 7.330E-05	5.076E-04 \pm 7.325E-05	5.076E-04 \pm 7.325E-05

Table D.10: Average and standard deviation of average residual (mm) for dataset 69 using LS, Huber and Bisquare estimators

Average Residual \pm Standard Deviation			
No. of View	LS	Huber	Bisquare
View 1	2.182E-03 \pm 1.359E-03	2.212E-03 \pm 1.392E-03	2.235E-03 \pm 1.413E-03
View 2	2.035E-03 \pm 9.407E-04	2.071E-03 \pm 9.773E-04	2.107E-03 \pm 1.006E-03
View 3	3.028E-03 \pm 1.789E-03	3.083E-03 \pm 1.827E-03	3.165E-03 \pm 1.898E-03
View 4	2.214E-03 \pm 1.343E-03	2.252E-03 \pm 1.405E-03	2.287E-03 \pm 1.468E-03
View 5	2.031E-03 \pm 1.060E-03	2.060E-03 \pm 1.115E-03	2.101E-03 \pm 1.195E-03
View 6	1.570E-03 \pm 4.695E-04	1.570E-03 \pm 4.700E-04	1.570E-03 \pm 4.702E-04
View 7	1.375E-03 \pm 2.342E-04	1.375E-03 \pm 2.342E-04	1.375E-03 \pm 2.343E-04
View 8	1.806E-03 \pm 7.051E-04	1.812E-03 \pm 7.073E-04	1.819E-03 \pm 7.109E-04
View 9	2.749E-03 \pm 3.376E-03	2.791E-03 \pm 3.477E-03	2.845E-03 \pm 3.608E-03
View 10	1.547E-03 \pm 3.792E-04	1.547E-03 \pm 3.801E-04	1.548E-03 \pm 3.814E-04
View 11	2.246E-03 \pm 1.453E-03	2.274E-03 \pm 1.516E-03	2.313E-03 \pm 1.604E-03
View 12	1.775E-03 \pm 1.159E-03	1.798E-03 \pm 1.216E-03	1.840E-03 \pm 1.315E-03

Table D.11: Average and standard deviation of average residual (mm) for dataset 70 using LS, Huber and Bisquare estimators

Appendix E

Whole Plants Surface Area Measurement From Yang and Our Experiment

Day	Time	No. of Dataset	Wild Type	PBI 121	10^4	3^1
Day 10	20:30	30	3342.62	3777.84	5059.15	3930.76
Day 10	02:00	31	3730.31	3874.14	3719.14	4363.21
Day 10	07:30	32	3822.18	4263.61	3927.54	4166.91
Day 11	20:30	33	4197.74	4180.32	4295.79	5000.05
Day 11	02:00	34	4102.25	4480.02	4376.26	5106.50
Day 11	07:30	35	4232.78	4924.62	4554.71	5214.75
Day 12	20:30	36	5032.27	5014.17	4843.95	6219.73
Day 12	02:00	37	4773.76	5650.46	5259.04	5701.83
Day 12	07:30	38	5186.52	5812.33	5445.97	6120.73
Day 13	20:30	39	5902.45	5915.17	5724.45	6745.73
Day 13	02:00	40	5861.97	6248.85	5951.78	6777.32

Table E.1: Canopy area measurement (mm^2) from Yang's experiment (Datasets 30-40)

Day	Time	No. of Dataset	Wild Type	PBI 121	10^4	3^1
Day 20	20:30	60	14172.20	16443.74	15858.38	15977.50
Day 20	02:00	61	14792.92	15852.55	16123.73	15394.64
Day 20	07:30	62	15014.97	16674.08	16615.42	17328.54
Day 21	20:30	63	16120.92	16794.41	16931.46	17652.27
Day 21	02:00	64	16019.35	16921.30	17557.30	17363.46
Day 21	07:30	65	15341.21	18471.51	17305.88	17959.18
Day 22	20:30	66	16320.89	18017.47	17347.15	18678.06
Day 22	02:00	67	16220.81	18553.07	17523.78	17509.06
Day 22	07:30	68	16750.02	18333.81	18383.57	19164.54
Day 23	20:30	69	17297.20	17589.05	17892.23	17892.23
Day 23	02:00	70	17196.29	18839.08	17930.98	19511.85

Table E.2: Canopy area measurement (mm^2) from Yang's experiment (Datasets 60-70)

Day	Time	No. of Datasets	Wild Type	pBI 121	10^4	3^1
Day 10	20:30	30	3496.31	3157.16	3762.83	3367.57
Day 10	02:00	31	3585.96	3502.92	3841.31	3540.40
Day 10	07:30	32	3537.87	3458.65	4011.28	3573.07
Day 11	20:30	33	3864.04	3893.66	4283.65	4109.90
Day 11	02:00	34	4316.47	4130.61	4761.47	4244.41
Day 11	07:30	35	4320.21	4180.14	5026.26	4122.45
Day 12	20:30	36	4633.31	4664.31	5038.71	4881.80
Day 12	02:00	37	4641.03	4690.95	5051.10	4893.05
Day 12	07:30	38	4817.77	4825.52	5099.75	4977.78
Day 13	02:00	40	5083.11	5229.51	5302.69	5366.00

Table E.3: Canopy area measurement (mm^2) from our experiment (Datasets 30-40)

Day	Time	No. of Datasets	Wild Type	pBI 121	10 ⁴	3 ¹
Day 20	20:30	60	13582.09	15297.73	13486.47	14382.57
Day 20	02:00	61	14101.53	14497.15	13276.03	14148.77
Day 20	07:30	62	12484.63	10572.50	9417.98	10566.93
Day 21	20:30	63	9463.17	12037.84	9499.38	10741.95
Day 21	02:00	64	13136.28	13268.39	12342.89	12920.67
Day 21	07:30	65	13177.36	13906.46	12803.19	12943.45
Day 22	20:30	66	13190.81	10584.92	11996.18	11191.61
Day 22	02:00	67	13643.68	13982.82	13003.61	14523.48
Day 22	07:30	68	11919.97	9602.43	8038.32	10960.86
Day 23	02:00	70	13533.68	13246.14	13255.76	13176.26

Table E.4: Canopy area measurement (mm²) from our experiment (Datasets 60-70)

Appendix F

3D Stem Volume Measurement From Yang Our Experiment

Day	Time	No. of Datasets	Wild Type	pBI 121	10^4	3^1
Day 20	20:30	60	447.99	592.30	588.72	785.41
Day 20	2:00	61	491.07	591.76	618.72	803.96
Day 20	7:30	62	541.22	648.72	636.17	862.45
Day 21	20:30	63	581.54	705.73	717.14	905.09
Day 21	2:00	64	631.58	772.62	769.13	958.34
Day 21	7:30	65	626.33	747.53	751.51	1053.76
Day 22	20:30	66	652.35	815.23	824.52	1082.48
Day 22	2:00	67	693.81	885.94	843.67	1111.48
Day 22	7:30	68	700.39	948.02	988.02	1238.09
Day 23	20:30	69	761.51	1052.42	1011.52	1390.39
Day 23	2:00	70	793.11	1139.29	1093.17	1285.12

Table F.1: 3D stem volume measurement (mm^3) from Yang's experiment (Datasets 60-70)

Day	Time	No. of Datasets	Wild Type	pBI 121	10^4	3^1
Day 20	20:30	60	35082.85	98915.89	50517.96	61119.68
Day 20	02:00	61	70072.73	101520.10	51103.44	61963.46
Day 20	07:30	62	71494.65	104441.50	57609.21	62437.06
Day 21	20:30	63	98722.67	106156.60	43577.41	81628.91
Day 21	02:00	64	77284.93	117533.50	84733.73	37875.49
Day 21	07:30	65	79526.28	123383.00	2082.85	90746.66
Day 22	20:30	66	86207.63	106383.70	35876.06	133797.00
Day 22	02:00	67	87164.23	107997.00	171849.80	138036.40
Day 22	07:30	68	87711.48	125942.80	99290.14	153445.50
Day 23	02:00	70	87093.84	151774.40	120619.40	98104.56

Table F.2: Canopy area measurement (mm^3) from our experiment (Datasets 60-70)

Appendix G

Macros used to Automate Various Geomagic's Tools

```
'*****  
'This macro saves a file in STL format  
  
' This macro is used to save the semi-spheres 3PI files in STL Format  
'*****  
  
' Specify the current directory (folder path)  
' This is needed as we want to perform a certain operation on every  
' files of this directory  
FolderPath = "C:\Save_as_STL\  
Set fso = CreateObject ("Scripting.FileSystemObject")  
Set folder = fso.GetFolder (FolderPath)  
  
' "files" contains every file of the above directory  
Set files = folder.Files  
  
for each file in files  
str = "3pi"  
a = Split (file, ".")  
  
If a(1) = str Then  
' Open each file in the current directory in Geomagic's  
' "Display Manager"  
geo.open 0, 1, CStr(file)  
newFile = a(0) & ".stl"  
' The first 2 arguments in important for geo.saveas  
' newFile = The name of the STL file  
' 3 indicates that the user wants to save the file in STL format
```

```

geo.saveas newFile, 3, 1, 0, 0, 0, 0, 0, 1, 0, 0, 0, -1, 0, 1, 0
End If
next

'*****
' This macro combines multiple Polygon objects.

' This macro is used to combine the full sphere files and the plant only
' files during the reconstruction of views phase.
'*****

' Specify the current directory (folder path)
' "Combined.txt" is a text file which contains the information of the
' total number of semi-spheres in each view. This information is needed
' during the reconstruction phase.
Set objFSO = CreateObject ("Scripting.FileSystemObject")
Set objFile = objFSO.OpenTextFile ("C:\Combined\Combined.txt",
ForReading)
Const ForReading = 1

Path = "C:\Combined\"

Dim Temp(6)
i = 0
Do Until objFile.AtEndOfStream
' The first line of "Combined.txt" contains the total number of files
' on which this operation needs to be performed
If i = 0 Then
Total_File = objFile.ReadLine

Else
File_Name = objFile.ReadLine
Total_Sphere = objFile.ReadLine

' Plant only file has the prefix "Delete-"
a = Split (File_Name, ".")
Delete_File_Name = Path & "Delete-" & a (0) & ".stl"

' Full sphere files have the prefix "Full-Ball-"
For j = 0 to (Total_Sphere-1)
Temp (j) = Path & "Full-Ball-" & (j+1) & "-" & a (0) & ".stl"
Next

If Total_Sphere = 6 Then

```

```

' Open each file in the current directory in Geomagic's
' "Display Manager"
' Second argument = Total number of files to be opened
geo.open 0, 7, CStr(Delete_File_Name), CStr(Temp (0)), CStr(Temp (1)),
CStr(Temp (2)), CStr(Temp (3)), CStr (Temp(4)), CStr(Temp (5))

ElseIf Total_Sphere = 5 Then
geo.open 0, 6, CStr(Delete_File_Name), CStr (Temp (0)), CStr (Temp (1)),
CStr (Temp (2)), CStr (Temp (3)), CStr (Temp (4))

ElseIf Total_Sphere = 4 Then
geo.open 0, 5, CStr(Delete_File_Name), CStr (Temp (0)), CStr (Temp (1)),
CStr (Temp (2)), CStr (Temp (3))

ElseIf Total_Sphere = 3 Then
geo.open 0, 4, CStr(Delete_File_Name), CStr (Temp (0)), CStr (Temp (1)),
CStr (Temp (2))
End If

' Combining the active files in the display manager
' Combined_File_Name is the object name not the file name
Combined_File_Name = "Combined-" & a (0)
geo.merge_polygon_objects Combined_File_Name, 0

' Saving as WRP file with the prefix "Combined-"
WRP_Name = Path & Combined_File_Name & ".wrp"
geo.saveas WRP_Name, 1000, 1, 0, 0, 1, 0, 0, 0, 0, 0, -1, 0, 1, 0
End If

i = i + 1
Loop

objTextFile.Close

'*****
'This macro converts a polygon object into point object
'Also re-samples the point object by a specified factor

' This macro is used before registration process as some of tools of
' Geomagic can not be recorded as macros in case of large dataset
'*****

' Specify the current directory (folder path)
' This is needed as we want to perform a certain operation on every

```



```

' files of this directory
FolderPath = "D:\Point_Sample\"
Set fso = CreateObject ("Scripting.FileSystemObject")
Set folder = fso.GetFolder (FolderPath)
Set files = folder.Files

for each file in files
str = "wrp"
a = Split (file, ".")

If a(1) = str Then
' Open each file in the current directory in Geomagic's
' "Display Manager"
geo.open 0, 1, cStr(file)
' Converts the current polygon object into a point object
geo.modify_current_points 0
' Re-samples the point object by a specified factor
' In our case, factor = 0.5 mm
geo.sample 0.0005, 0, false, 0

b = Split (a(0), "\")
a = Split (b(3), "-")
newFile = FolderPath & "Point" & "-" & a(1) & "-" & a(2) & "-" & a(3)
& ".wrp"
' Saving as WRP file with the prefix "Point-"
geo.saveas newFile, 1000, 1, 0, 0, 1, 0, 0, 0, 0, 0, 0, -1, 0, 1, 0
End If
next

objTextFile.Close

'*****
'This macro performs all the steps of the final registration

' This macro include "Target Registration", "Target Cleanup" and "Global
' Registration" phases
'*****

' Specify the current directory (folder path)
' "Registration.txt" is a text file which contains the information of the
' total number of files in the directory and total number of views in a
' single dataset. This information is needed
' during the registration phase.
Set objFSO = CreateObject ("Scripting.FileSystemObject")
Set objFile = objFSO.OpenTextFile ("C:\Registration\Registration.txt",

```

```

ForReading)
Const ForReading = 1

Path = "C:\Registration\"

Dim Temp(12)
i = 0
Do Until objFile.AtEndOfStream
If i = 0 Then
' The first line of "Registration.txt" contains the total number of
' files on which this operation needs to be performed
Total_File = objFile.ReadLine

Else
' The second line contains basic file name and the third line contains
' the total number of views in a dataset
File_Name = objFile.ReadLine
Total_Scene = objFile.ReadLine

a = Split (File_Name, ".")
objTextFile.Write (a(0)) & vbCrLf
b = Split (a(0), "-")

' Target detected files have the prefix "Target-Detected-"
For j = 0 to (Total_Scene-1)
Temp (j) = Path & "Target-Detected-" & b(0) & "-" & b(1) & "-" & "00"
& j & ".wrp"
Next

' objectName is the object name not the file name
' finalName is the WRP file name
objectName = "Registered-" & b(0) & "-" & b(1)
finalName = Path & "Registered-" & b(0) & "-" & b(1) & ".wrp"

' Open each file in the current directory in Geomagic's
' "Display Manager"
' Second argument = Total number of files to be opened
geo.open 0, 12, CStr(Temp (0)), CStr(Temp (1)), CStr(Temp (2)),
CStr(Temp (3)), CStr (Temp(4)), CStr(Temp (5)), CStr(Temp (6)),
CStr(Temp (7)), CStr(Temp (8)), CStr(Temp (9)), CStr (Temp(10)),
CStr(Temp (11))

' These are the tools used for registration purpose
' "Target Registration", "Target Cleanup", "Global Registration",
' and "Merge"

```

```
geo.target_registration 0, 0, 0.1, 1, 0, 0, 0
geo.global_registration 0, 100, 2000, false, 20, false, true, false
geo.merge_polygon_objects objectName, 0

' Saving as WRP file with the prefix "Combined-"
geo.saveas finalName, 1000, 1, 0, 0, 1, 0, 0, 0, 0, 0, 0, -1, 0, 1, 0
End If

i = i + 1
Loop

objTextFile.Close
```

Bibliography

- [1] M. D. Fox and L. G. Puffer. Analysis of Transient Plant Movements by Holographic Interferometry. *Nature*, 261:488–490, June 1976.
- [2] M. D. Fox and L.G. Puffer. Holographic Interferometric Measurement of Motions in Mature Plants. *Plant Physiology*, 60:30–33, 1977.
- [3] A. Lang. Xylem, Phloem and Transpiration Flows in Developing Apple Fruits. *Journal of Experimental Botany*, 41(227):645–651, 1990.
- [4] S. V. Pasumarty, P. E. H. Minchin, D. W. Fountain, and R. G. Thomas. Influence of Shade on the Growth and Sink Activity of Young Flower Heads and Peduncles of White Clover (*Trifolium Repens* L.). *Journal of Experimental Botany*, 42(239):705–710, 1991.
- [5] J. L. Barron and A. Liptay. Optic Flow to Measure Minute Increments in Plant Growth. *BioImaging*, 2(1):57–61, 1994.
- [6] J. L. Barron, A. Aboelela, and A. Liptay. Using Optical Flow in Near-infrared Imagery to Measure Plant Growth. *Intl. Journal of Robotics and Automation (IJRA'05)*, ACTA Press, 20(1), 2005.
- [7] A. Liptay, J. L. Barron, T. Jewett, and I. Wesenbeeck. Oscillations in Corn Seedling Growth as Measured by Optical Flow. *Journal of American Society for Horticultural Science*, 120(3):379–385, 1995.
- [8] J. L. Barron and A. Liptay. Measuring 3d Plant Growth using Optical Flow. *BioImaging*, 5, 1997.
- [9] J. L. Barron, A. Liptay, and H. Spies. Optical Flow and Range Flow for Plant Growth and Leaf Motion. *Image and Vision Computing*, pages 68–77, 2000.
- [10] H. Spies, B. Jähne, and J. L. Barron. Regularised Range Flow. In *European Conference on Computer Vision (ECCV2'00)*, LCNS 1843/44, volume 2, pages 785–799. Springer, 2000.

- [11] H. Spies, B. Jähne, and J. L. Barron. Range Flow Estimation. *Computer Vision Image Understanding (CVIU'02)*, 85(3):209–231, 2002.
- [12] H. Spies, H. Haußecker, B. Jähne, and J. L. Barron. Differential Range Flow Estimation. In *21st Symposium Fur Mustererkennung (DAGM'99)*, pages 309–316, Bonn, Germany, 1999. Springer.
- [13] H. Spies, B. Jähne, and J. L. Barron. Dense Range Flow from Depth and Intensity Data. In *Intl. Conference on Pattern Recognition (ICPR'00)*, pages 131–134, 2000.
- [14] H. Spies, B. Jähne, and J. L. Barron. Surface Expansion from Range Data Sequences. In *23rd Symposium Fur Mustererkennung (DAGM'01), LNCS 2191*, pages 163–169, Munich, Germany, 2001. Springer.
- [15] C. Zhao. 3d Plant Growth Measurement using the Shapegrabber Laser Scanner. Master's thesis, Department of Computer Science, University of Western Ontario, Middlesex College, London, ON, Canada N6A 5B7, 2009.
- [16] P. Yang. Quantitative 3D Plant Growth of Arabidopsis Thaliana using 3D Range Images. Master's thesis, Department of Computer Science, University of Western Ontario, Middlesex College, London, ON, Canada N6A 5B7, 2010.
- [17] Z. Zhang. Parameter Estimation Techniques: A Tutorial with Application to Conic Fitting. *Image and Vision Computing*, 15:59–76, 1997.
- [18] S. J. Ahn, W. Rauh, and H. J. Warnecke. Least-Squares Orthogonal Distances Fitting of Circle, Sphere, Ellipse, Hyperbola, and Parabola. *Pattern Recognition*, 34(12):2283–2303, December 2001.
- [19] C. Witzgall, G. S. Cheok, and A. J. Kearsley. Recovering Circles and Spheres from Point Data. In F. B. Alt, M. C. Fu, and B. L. Golden, editors, *Perspectives in Operations Research*, volume 36 of *Operations Research/ Computer Science Interfaces Series*, pages 393–413. Springer US, 2006.
- [20] C. Witzgall, G. S. Cheok, and A. J. Kearsley. Recovering Spheres from 3D Point Data. In *35th IEEE Applied Imagery and Pattern Recognition Workshop, AIPR'06*, page 8, October 2006.
- [21] A.W. Fitzgibbon, M. Pilu, and R.B. Fischer. Direct Least Squares Fitting of Ellipses, January 1996.
- [22] A.W. Fitzgibbon, M. Pilu, and R.B. Fischer. Direct Least Squares Fitting of Ellipses. In *Proc. of the 13th Intl. Conf. on Pattern Recognition*, pages 253–257, September 1996.

- [23] R. Halir and J. Flusser. Numerically Stable Direct Least Squares Fitting of Ellipses. In *The 6th Intl. Conf. in Central Europe on Computer Graphics and Visualization*, pages 125–132, 1998.
- [24] W. Gander, G. H. Golub, and R. Strebler. Least Squares Fitting of Circles and Ellipses, 1994.
- [25] M. Burr, A. Cheng, R. Coleman, and D. L. Souvaine. Transformations and Algorithms for Least Sum of Squares Hypersphere Fitting. In *16th Canadian Conference on Computational Geometry, CCCG'04*, pages 104–107, 2004.
- [26] G. Lukacs, R. Martin, and D. Marshall. Faithful Least-Squares Fitting of Spheres, Cylinders, Cones and Tori for Reliable Segmentation. In *In Proc. 5th European Conference, Computer Vision, ECCV'98*, pages 671–686, 1998.
- [27] J. Fox. Robust regression, 2002. <http://cran.r-project.org/doc/contrib/Fox-Companion/appendix-robust-regression.pdf>, [Last Accessed: 05.07.20011].
- [28] J. Fox and S. Weisberg. Robust Regression in R, December 2010.
- [29] S. Zhou, Y. Guan, X. Zhan, and T. Lu. Sphere Target Fitting of Point Cloud Data Based on M-Estimation. In *In Proc. of the 6th International Conference on Fuzzy Systems and Knowledge Discovery, FSKD'09*, pages 296–299, Washington, DC, USA, 2009. IEEE Computer Society.
- [30] P. Huber. Robust Estimation of Location Parameter, 1964.
- [31] H. Youcai. Data Snooping and Error-resistance Estimation, 1990.
- [32] D.A. Belsley, E. Kuh, and R.E. Welsch. Regression Diagnostics, 1980.
- [33] Z. Jiang and W. Staude. An interferometric method for plant growth measurements. *Journal of Experimental Botany*, 40(219):1169 – 1173, 1989.
- [34] A. A. Dyrseth. Measurement of plant movement in young and mature plants using electronic speckle pattern interferometry. *Applied Optics*, 35(19):3695 – 3701, 1996.
- [35] H. Kadono, N. Shimizu, and S. Toyooka. Statistical interferometry and application to monitoring of biological activity of plant. In *Proceedings of SPIE Digital Library*, volume 6341, September 2006.
- [36] H. Lüthen, M. Bigdon, and M. Böttger. Reexamination of the acid growth theory of auxin action. *Plant Physiology*, 93(3):931 – 939, July 1990.
- [37] A. Liptay, J. L. Barron, T. Jewett, and I. van Wesenbeeck. Oscillations in corn seedling growth as measured by optical flow. *Journal of American Society for Horticultural Science*, 120(3):379 – 385, 1995.

- [38] A. Aboeela, A. Liptay, and J. L. Barron. Using optical flow in near-infrared imagery to measure plant growth. *Intl. Journal of Robotics and Automation*, 20(1):43 – 49, 2004.
- [39] H. Spies, H. Haußecker, B. Jähne, and J. L. Barron. Differential range flow estimation. In *21.Symposium fur Mustererkennung (DAGM1999)*, pages 309 – 316, Bonn, Germany, 1999. Springer.
- [40] H. Spies, B. Jähne, and J. L. Barron. Regularised range flow. In *European Conference on Computer Vision (ECCV2000), LNCS 1843/44*, volume 2, pages 785 – 799. Springer, 2000.
- [41] H. Spies, B. Jähne, and J. L. Barron. Dense range flow from depth and intensity data. In *Int. Conference on Pattern Recognition (ICPR2000)*, pages 131 – 134, 2000.
- [42] H. Spies, B. Jähne, and J. L. Barron. Surface expansion from range data sequences. In *23rd Symposium fur Mustererkennung (DAGM2001), LNCS 2191*, pages 163 – 169, Munich, Germany, 2001. Springer.
- [43] H. Spies, B. Jähne, and J. L. Barron. Range flow estimation. *Computer Vision Image Understanding (CVIU2002)*, 85(3):209 – 231, 2002.
- [44] N. Ortiz-Uribe, R. R. Cloutier, E. D. Leonardos, M. J. Iqbal, W. Liu, J. Sutton, A. DesLauriers, J. Brockerville, I. Christie, and B. Grodzinski. Non-invasive monitoring of plant growth using 3d metrology and gas exchange. In *OCE Discovery 2006 Conference*, Toronto Conference Centre, Toronto, ON, Canada, February 2006.
- [45] H. H. Bartelink. Allometric Relationships for Biomass and Leaf Area of Beech (*Fagus sylvatica* l.). *Ann. For. Sci.*, 54:39–50, 1997.
- [46] K. E. Keightleya and G. W. Bawden. 3D Volumetric Modeling of Grapevine Biomass using Tripod LiDAR. *Computers and Electronics in Agriculture*, 74:305–312, September 2010.
- [47] D. Seidel, F. Beyer, D. Hertel, S. Fleck, and C. Leuschner. 3D-laser Scanning: A Non-destructive Method for Studying Above-ground Biomass and Growth of Juvenile Trees. *Agricultural and Forest Meteorology*, 151:1305–1311, June 2011.
- [48] F. Hosoi and K. Omasa. Factors contributing to Accuracy in the Estimation of the Woody Canopy Leaf Area Density Profile using 3D Portable LiDAR Imaging. *Journal of Experimental Botany*, 58:3463–3473, 2007.

- [49] P. J. Watt, D. N. M. Donoghue, and R. W. Dunford. Forest Parameter Extraction using Terrestrial Laser Scanning. In *In Proc. of the ScandLaser Scientific Workshop on Airborne Laser Scanning of Forests*, pages 237–244, September 2003.
- [50] K. S. Lim and P. M. Treitz. Estimation of Above Ground Forest Biomass from Airborne Discrete Return Laser Scanner Data using Canopy-based Quantile Estimators. *Scandinavian Journal of Forest Research*, 19:558–570, 2004.
- [51] Ken Garrard. MATLAB Central (Thread Subject: Best Fit Sphere). http://www.mathworks.ch/matlabcentral/newsreader/view_thread/157211; [Last Accessed: 04/ 01/ 2012].
- [52] Bill McDonald. MATLAB Central: File Exchange: surf2stl. <http://www.mathworks.com/matlabcentral/fileexchange/4512>; [Last Accessed: 13/ 03/ 2012].
- [53] S. Colin. *On vertex-vertex meshes and their use in Geometric and biological modeling*. PhD thesis, Dept. of Computer Science, University of Calgary, 2006.
- [54] P. Shirley, M. Ashikhmin, M. Gleicher, S. R. Marschner, E. Reinhard, K. Sung, W. B. Thompson, and P. Willemsen. *Fundamentals of computer graphics*. A K Peters, Ltd., Natick, MA, U.S.A., 2nd edition, 2005.
- [55] Graphpad Software Inc. <http://www.graphpad.com/welcome.htm>.

Vita

NAME

Akter, Quazi Mah-Zereen

BIRTH PLACE

Dhaka, Bangladesh

YEAR CAME TO CANADA

2010

RESEARCH INTEREST

Digital image processing, computer vision, computer graphics, 3D imaging reverse engineering.

EDUCATION

Master of Science, Computer Science anticipated, April 2012
University of Western Ontario September 2010 to present
London, ON, Canada
Supervisor: Dr. John L. Barron

Bachelor of Science, Computer Science & Engineering received, 2008
University of Dhaka July 2003 to April 2008

WORK EXPERIENCE

Research Assistant September 2010 - April 2012

Department of Computer Science
University of Western Ontario
London, ON, Canada

Teaching Assistant September 2010 - December 2011

Department of Computer Science
University of Western Ontario
London, ON, Canada

Lecturer February 2010 - August 2010

Northern University Bangladesh
Khulna, Bangladesh

Lecturer September 2008 - September 2009

State University of Bangladesh
Dhaka, Bangladesh